

A Development Framework for High Fidelity Non-hydrostatic Simulations of Cross Mountain
Flow

By

Jorge E. Guerra
DISSERTATION

Submitted in partial satisfaction of the requirements
for the degree of
DOCTOR OF PHILOSOPHY

in

Atmospheric Science

in the

OFFICE OF GRADUATE STUDIES

of the

UNIVERSITY OF CALIFORNIA

DAVIS

Approved:

Dr. Paul A. Ullrich (Chair)

Dr. Joseph Biello

Dr. Terry Nathan

Committee in Charge
2018

“One learns that the world, though made, is yet being made; that this is still the morning of creation; that mountains long conceived are now being born, channels traced for coming rivers, basins hollowed for lakes...”

John Muir

Abstract

Jorge E. Guerra

*A Development Framework for High Fidelity Non-hydrostatic
Simulations of Cross Mountain Flow*

The development of weather and climate prediction models is steadily progressing toward a unified state where multi-scale processes will be fully resolved on dense uniform, variable, or adaptive meshes. However, we are currently in a transition period where advances in computation, numerical methods, and scientific understanding of detailed atmospheric dynamics are converging and much work remains in all these areas to establish a new generation of operational weather and climate forecasting. This thesis aims to put forth a process for advancing numerical modeling of the atmosphere from formulation to implementation, design of numerical tests, and validation by exploring the detailed dynamics of orographically forced gravity wave breaking. We present a novel, efficient, and high-performance dynamical core, Tempest, and use it to create high resolution non-hydrostatic simulations of wave breaking with the purpose of investigating and informing on the behavior of a gravity wave drag parameterization currently in operational use. We demonstrate the superior properties of the numerical scheme using a variety of tests spanning a wide range of length scales. We further present an extension of the classical linear theory of mountain waves and use this solution in the design of fully nonlinear wave breaking simulations leading to a detailed characterization of gravity wave drag as it is implemented in general circulation models.

Acknowledgements

I would first like to thank Dr. Paul Ullrich for all of his work and effort in guiding this work. You have been a kind, persistent, patient, and sensitive force behind every step up the ladder of understanding. I also thank my colleagues; they are all inspiring thoughtful researchers and I look forward to sharing our discoveries in the future. I would like to mention Dr. Joseph Biello who came into my research work precisely at a time when I needed a “shot in the arm.” His enthusiasm for the challenging problems in geophysical fluid dynamics leaves a lasting impression on me. I thank Dr. Graham Fogg and Dr. Carole Hom for all of their support through the Climate Change, Water and Society traineeship program. They endeavor to teach young scientists the value of collaboration and have given me the tools to be courageous about engaging diverse research. I especially thank Dr. Franci Giraldo of the Naval Postgraduate School for his participation in my Qualifying Examination; it was an honor for him to serve and a real challenge to confront such an expert in the development of numerical models.

I lack the words to express the tremendous importance that my wife Kathleen has for me. This work (and any subsequent work I might accomplish) simply isn't possible without her support and love. She brought light and love to my life and set my mind free with confidence to pursue this degree. I thank my daughter Maren because she has taught me the meaning of purpose and perseverance. Lastly, I thank my parents and sisters for the love, sacrifice, and faith they placed upon me throughout my life. There is nothing more important than the support of family for people to grow emotionally and intellectually strong.

Contents

Abstract	ii
Acknowledgements	iii
List of Figures	viii
List of Tables	xvi
1 Introduction and Background	1
1.1 Non-hydrostatic vertical motion in numerical weather and climate prediction	2
1.2 Spatial discretizations for non-hydrostatic models	3
1.3 Theoretical and computational study of mountain wave breaking	7
1.4 Outline of the thesis	11
2 A High-Order Staggered Finite-Element Vertical Discretization for Non-Hydrostatic Atmospheric Models	12
2.1 Introduction	13
2.2 The non-hydrostatic equations of fluid motion	16
2.3 Discretization	19
2.3.1 Horizontal Discretization	19
2.3.2 Vertical Discretization	20
Interpolation Operators	21
Differentiation Operators	22

Second Derivative Operators in the Vertical	25
Flow-dependent vertical hyperviscosity	27
The Staggered Nodal Finite Element Method (SNFEM)	28
2.3.3 Temporal Discretization	30
2.4 Validation	33
2.4.1 Steady-state geostrophically balanced flow in a channel	34
2.4.2 Schär mountain	39
2.4.3 Straka density current	46
2.4.4 Rising thermal bubble	53
2.4.5 Numerical Characteristics of the Method	59
2.5 Conclusions	63
3 An Orographically Forced Shear Flow Linear Model for Numerical Test Design and Val-	
idation	67
3.1 Introduction	68
3.2 The 2-D linearized equations in terrain-following Cartesian coordinates	70
3.2.1 A new vertical coordinate transformation with uniform smooth decay	74
3.3 Semi-analytic reference solution of the perturbation equations	76
3.3.1 Boundary conditions and terrain forcing	78
3.4 The sheared jet Schär Mountain test	80
3.4.1 Background jet	81
3.4.2 Thermodynamic and kinematic background initial state	83
3.4.3 Comparison to the classical theory	84
3.5 Numerical tests and results	86
3.5.1 Diagnostic instability parameters	91
3.6 Nonlinear wave breaking simulations	93
3.7 Conclusions	94

4	An Assessment of the Lindzen/McFarlane Orographic Gravity Wave Drag Parameterization at Non-hydrostatic Scale	97
4.1	Introduction	98
4.2	Lindzen/McFarlane wave drag parameterization	100
4.2.1	Formulation	100
4.2.2	Implementation	103
4.3	Methodology	104
4.3.1	Elevation of the Tropical Andes	105
4.3.2	Terrain filtering and analysis	106
4.4	Numerical test design - 2D Wave breaking	110
4.4.1	Background atmospheric conditions	111
4.4.2	Discrete setup and initialization	112
4.4.3	Stratified turbulence metrics	114
4.4.4	Transient drag force comparison metrics	115
4.4.5	Test configurations	116
4.5	Results	117
4.5.1	Linear steady-state predictions	117
4.5.2	High-resolution reference	122
4.5.3	Transient drag forces - Test configurations	130
4.5.4	Parameterization input fields	132
4.5.5	Parameterized drag	135
4.6	Conclusions	137
5	Summary, Conclusions, and Future Directions	139
A		141
A.1	Metric terms based on new terrain decay function	142
A.2	Linearization of the Inviscid Equations - Conservation Form	143

B	146
B.1 Linear Steady State Model Solution	147
B.2 Terrain Input Processing	150
Bibliography	151

List of Figures

1.1	Spectral element and staggered vertical column element discretization. u, ρ, θ are horizontal velocity, density, and potential temperature at a model level, and w is the vertical velocity at a model interface including top and bottom boundaries. \mathcal{D} operators represent local derivatives projected from levels to interfaces \mathcal{D}_n^i and interfaces to levels \mathcal{D}_i^n	5
1.2	Schematic of the McFarlane (1987) parameterization scheme also showing turbulent stress at the base of a computational column. The equation shows the relationship between zonal mean horizontal wind \bar{u} and vertical gradient of zonal mean momentum flux covariance $u'w'$ subject to the Boussinesq approximation where only the background variation in density ρ_0 is considered.	9
1.3	Schematic of dynamical processes expected as a current of air encounters mountainous terrain.	10
2.1	(a) Vertical placement of (left) Gauss-Lobatto nodes and (right) Gauss nodes within a vertical element with $n_{vp} = 3$. (b) Basis functions $\tilde{\phi}_{a,k}$ for Gauss-Lobatto nodes within element a . (c) Basis functions $\phi_{a,k}$ for Gauss nodes within element a	21
2.2	A depiction of the derivative operators \mathcal{D}_n^i and \mathcal{D}_i^n , which remap from interfaces to levels and levels to interfaces, respectively. The gray line depicts a typical field variable within element a that emerges from the expansion (left) (2.24) or (center) (2.23).	23

2.3	Baroclinic wave in a 3D Cartesian channel at the reference resolution $\Delta x = 100$ km, $\Delta y = 100$ km, $\Delta z = 1$ km at vertical 4th order accuracy (VO4). From top to bottom, temperature, vorticity, vertical velocity, and divergence are shown at day 10 (left) and 15 (right) and at an elevation of 500 m. Contour intervals: Temperature 2K, Vorticity $1.0 \times 10^{-5} \text{s}^{-1}$, Divergence $5.0 \times 10^{-6} \text{s}^{-1}$, and vertical velocity $2.0 \times 10^{-3} \text{m s}^{-1}$.	37
2.4	Baroclinic wave in a Cartesian channel at vertical orders 2, 4 and 10. Vorticity at 500 meters on days 10 and 15 at the resolution $\Delta x = 200$ km, $\Delta y = 200$ km, $\Delta z = 1.5$ km. Contour interval: $1.0 \times 10^{-5} \text{s}^{-1}$	38
2.5	Baroclinic wave in a Cartesian channel at vertical orders 2, 4 and 10. Vertical Velocity at 500m on days 10 and 15 at the resolution $\Delta x = 200$ km, $\Delta y = 200$ km, $\Delta z = 1.5$ km. Contour interval: $2.0 \times 10^{-3} \text{m s}^{-1}$	38
2.6	Schär flow at steady state (10 hours) vertical velocity in (m/s) at VO4. Reference resolution shown compared to the analytical solution (dotted contours) from linear mountain wave theory. $\Delta x = 100$ m and $\Delta z = 100$ m. Contour interval: 0.1m s^{-1}	40
2.7	Schär flow at steady state (10 hours). Collocated method (all variables on column levels) result compared to staggered (Lorenz) solution at the same spatial order and resolution. $\Delta x = 200$ m and $\Delta z = 200$ m. Contour intervals: vertical velocity 0.1m s^{-1} and vertical velocity difference versus reference 0.0125m s^{-1}	41
2.8	Still atmosphere experiment over Schär mountain profile at vertical orders 2, 4, and 10 showing errors in vertical velocity. $\Delta x = 500$ m and $\Delta z = 500$ m. Contour interval: $2.0 \times 10^{-5} \text{m s}^{-1}$.	42
2.9	Schär flow at steady state (10 hours) vertical velocity in (m/s) at various vertical orders of accuracy (2, 4, 10, and ST) where "ST" stands for single column element spectral transform ($n_{ve} = 1$) with Lorenz (LOR) vertical staggering. Colored contours from Tempest compared to dotted contours for the analytical solution. $\Delta x = 500$ m and $\Delta z = 500$ m. Contour interval: 0.1m s^{-1}	43

2.10	Schär flow steady state (10 hours). Vertical velocity difference with respect to the reference solution (fig. 2.6, left). Results are interpolated to a regular z coordinate with $\Delta z = 500$ m in experiments and reference solution for differencing. Computations performed at $\Delta x = 500$ m and $\Delta z = 500$ m. Contour interval: 0.0125m s^{-1} . . .	44
2.11	Schär mountain vertical profile of momentum flux for all experiments. The flux profiles are computed by $\int_{-X}^X \{[\bar{\rho} + \rho'] [\bar{u} + u'] w'\} dx$ at $t = 10\text{hours}$ where overbars indicate initial condition values and primes are departures thereof. Results are interpolated to a regular z coordinate with $\Delta z = 500$ m in experiments and reference solution to compute the integral flux. Results are normalized to the value at the surface in the reference solution.	45
2.12	Straka Density Current test reference solutions at vertical order 4 in two staggering configurations LOR and CPH. Converged resolution of $\Delta x = 25$ m and $\Delta z = 25$ m shown. Vertical flow dependent diffusion in of order 2 and 4 (rows 2 and 3) is compared with the reference solution where an explicit 2^{nd} order diffusion with $\nu_0 = 75\text{ m}^2\text{s}^{-1}$ is used (top row). Contour interval: 1.0K	48
2.13	Straka Density Current test at vertical order 2, 4 and 10. Coarse, evaluation resolution of $\Delta x = 190$ m and $\Delta z = 160$ m shown. Vertical flow dependent diffusion of order 2 and 4 (rows 2 and 3) is compared with the reference solution where an explicit 2^{nd} order diffusion with $\nu_0 = 75\text{ m}^2\text{s}^{-1}$ is used (top row). Results for Lorenz (LOR) staggering shown. Contour interval: 1.0K	50
2.14	Straka Density Current test at vertical order 2, 4 and 10. Coarse, evaluation resolution of $\Delta x = 190$ m and $\Delta z = 160$ m with explicit 2^{nd} order diffusion with $\nu_0 = 75\text{ m}^2\text{s}^{-1}$ compared at 1200 m with the reference solution ($\Delta x = 25$ m and $\Delta z = 25$ m). Results for Lorenz (LOR) staggering shown.	51

2.15	Straka Density Current test at vertical order 2, 4 and 10. Coarse, evaluation resolution of $\Delta x = 190$ m and $\Delta z = 160$ m shown. Vertical flow dependent diffusion of derivative order 2 and 4 compared at 1200 m with the reference solution ($\Delta x = 25$ m and $\Delta z = 25$ m). Results for Lorenz (LOR) staggering shown.	51
2.16	Rising thermal bubble potential temperature reference solution at vertical order 4. Reference resolution $\Delta x = 5$ m and $\Delta z = 5$ m. Flow at 700 and 1200 seconds. Contour interval: 0.05K	55
2.17	Rising Robert bubble potential temperature reference solution at vertical order 4. Reference resolution $\Delta x = 5$ m and $\Delta z = 5$ m. Flow at 800 and 1200 seconds. Contour interval: 0.05K	56
2.18	Rising thermal bubble potential temperature at vertical orders 2, 4 and 10. Convection bubbles at 700 and 1200 seconds. Coarse, resolution $\Delta x = 10$ m and $\Delta z = 10$ m. Extrema in θ shown. Contour interval: 0.05K	57
2.19	Rising Robert bubble potential temperature at vertical orders 2, 4 and 10. Convection bubbles at 800 at 1200 seconds. Coarse, evaluation resolution $\Delta x = 10$ m and $\Delta z = 10$ m. Extrema in θ shown. Contour interval: 0.05K	58
2.20	Spatial (left) and temporal (right) self convergence at various vertical orders of accuracy. Thermal bubble test at 200 s. Spatial resolution for temporal convergence is 10 m with reference $\Delta t = 0.001$ s. Reference spatial resolution is $\Delta x = 2$ m.	61
2.21	Observed normalized change in mass and energy (top row), along with zonal and vertical momentum (bottom row) using the Robert Bubble experiment in section 2.4.4. The reference solution corresponds to fig. 2.17 with 5 m resolution. Evaluation experiments use variable vertical order (VO) SNFEM at 10 m resolution corresponding to fig. 2.19. Total normalized mass and energy change are computed as $(Q_t - Q_{initial}) / Q_{initial}$	62

3.1	Comparison of terrain decay functions. The coordinate of Gal-Chen and Somerville (1975) left and (3.16) right showing decay of terrain features near boundary terrain.	76
3.2	Background wind and thermodynamic profiles. Dry atmosphere with a prescribed sensible temperature distribution (top right).	82
3.3	The original Schär mountain test case computed by our reference solution as compared to the classical theory Fourier solution.	85
3.4	Overlay of numerical results and linear reference solution. Dashed contours represent the reference solution and filled contours correspond to numerical results at various resolutions. Vertical Velocity (m s^{-1}).	88
3.5	L_2 error convergence of numerical integration with respect to the semi-analytical reference solution. 10 m terrain height. Density (kg m^{-3}).	89
3.6	L_2 error convergence of numerical integration with respect to the semi-analytical reference solution. 10 m terrain height. Vertical Momentum ($\text{kg m}^{-2} \text{s}^{-1}$).	90
3.7	Difference in density for 3LAYER configuration with respect to simulation. Scaling set to show structure in the error fields. Density (kg m^{-3}).	90
3.8	Numerical to reference solution difference. Scaling set to show structure in the error fields. Vertical Velocity difference (m s^{-1}).	91
3.9	Local Richardson number and convective stability parameter for 3LAYER configuration. Reference solution with 10, 100 and 1000 m mountains from top to bottom. Fields plotted in the vertical axis only to show vertical structure. Dashed line indicates $Ri = 0.25$	92
3.10	Convective stability parameter for 3LAYER configuration. Reference solution with 10, 100 and 1000 m mountains from top to bottom. Fields plotted in the vertical axis only to show vertical structure.	92
3.11	Wave breaking in the 3LAYER configuration. Potential temperature deviation (K) field shown.	95

4.1	Digital elevation map of the equatorial Andes. Height in km. Domain distances are specified relative to the South West corner of the data map at 82° West and 6° South.	105
4.2	The normalized amplitude spectra for all horizontal cross sections as a function of wavelength (in m). The dark black line denotes the average spectrum for longitudinal cross sections. Dotted black line corresponds to the k^{-2} decay law.	107
4.3	Input terrain profile processing. Black curve denotes the circularly shifted data, red curve is the 4 th order Gaussian windowing function, and in blue is the resulting input profile. Height is normalized to unity.	107
4.4	The input terrain normalized amplitude spectra. Filter widths are 0.1 km (blue), 0.2 km (orange), 1.0 km (yellow), 5.0 km (purple), 25.0 km (green).	109
4.5	The input terrain normalized amplitude spectra. Filter widths are 0.1 km (blue), 0.2 km (orange), 1.0 km (yellow), 5.0 km (purple), 25.0 km (green).	109
4.6	The background wind and thermodynamic profiles as a function of geometric height. Vertical profile and gradient details and parameters specified in Chapter 2.	111
4.7	Schematic diagram of initial horizontal flow field and orographic forcing for numerical tests. Dashed black lines indicate the position of the sponge layers. The solid black rectangle shows a control volume boundary to evaluate net drag as given by (4.13). Terrain profile has been magnified for visualization in this figure.	113
4.8	Vertical scatter plots of Richardson number (4.14) and convective stability (4.15) criteria computed from the linear solution with 1000 m peak terrain height. Dashed black lines indicate the stability thresholds. Markers corresponds to each grid value plotted by amplitude-Z. Red curves denote Ri and S_p evaluated with initial conditions.	119
4.9	Vertical scatter plot of local Froude number from (4.16) computed from the linear solution with 100 m peak terrain height. The red curve indicates profile based on initial conditions. Markers corresponds to each grid value plotted by amplitude-Z.	120

4.10	Linear solution frequency response map. Horizontal (top log axis) and vertical velocity (bottom linear axis) response as a function of horizontal spatial frequency k . Response amplitude is normalized to unity.	122
4.11	Potential temperature departure (K) from initial state before (2.5 hours top plot) and after (14 hours middle plot) wave breaking in the reference simulation. Bottom plot shows response at 28 hours.	124
4.12	Horizontal velocity departure (ms^{-1}) from initial state before (2.5 hours top plot) and after (14 hours middle plot) wave breaking in the reference simulation. Bottom plot shows response at 28 hours.	125
4.13	Horizontal component of kinetic energy power spectra as a function of elevation over wavelengths 200 to $1.0\text{E}5$ m. Values of \mathcal{N} correspond to the initial background conditions at the specified elevation.	126
4.14	Vertical component of kinetic energy power spectra as a function of elevation over wavelengths 200 to $1.0\text{E}5$ m. Values of \mathcal{N} correspond to the initial background conditions at the specified elevation.	127
4.15	The net drag force with the bottom surface of the control volume changed from $Z_1 = 5$ to 15 km elevation. The control volume region is given by [-100 250] km by [Z_1 25] km in the vertical, with $Z_1 = 5\text{km}$ (blue), $Z_1 = 10\text{km}$ (red), and $Z_1 = 15\text{km}$ (black). Results from the reference resolution simulation at 100 m horizontal and vertical resolution.	129
4.16	The net drag force comparison for wave breaking region (blue) and jet core region (red). The control volume regions are given by [-100 250] km by [15 25] km (wave breaking) and [05 15] km (jet core) in the vertical. Results from the reference resolution simulation at 100 m horizontal and vertical resolution.	129

4.17	The net drag force comparison for wave breaking region directly above terrain (blue), in the turbulent wake (red) and the combined region (black) over the same depth. The control volume regions are given by [-100 100] km by [15 25] km (blue) and [100 250] km by [15 25] (red). Results from the reference resolution simulation at 100 m horizontal and vertical resolution.	130
4.18	The net drag force comparison for wave breaking region in FINE configuration tests. The control volume region is given by [-100 250] km by [15 25] km. FINE test resolution 200 m with input filter widths of 1.0, 5.0, and 25.0 km.	131
4.19	The net drag force comparison for wave breaking region in COARSE configuration tests. Control volume region: [-100 250] km by [15 25] km. COARSE test resolutions matching filter widths 1.0, 5.0, and 25.0 km.	131
4.20	The ensemble (time) averaged total horizontal velocity with (left) FINE resolution and (right) COARSE resolution simulations with 25 km terrain filtering.	134
4.21	The ensemble (time) averaged total $\ln \theta$ with (left) FINE resolution and (right) COARSE simulations with 25 km terrain filtering.	134
4.23	The parameterized stress and deceleration drag for the FINE configuration. Total drag estimate in [-100 250] km by [15 25] km region: 80.6 kNm^{-1}	136
4.22	The spatial distribution of standard deviation for each filtering level. Filter widths are 0.1 km (blue), 0.2 km (orange), 1.0 km (yellow), 5.0 km (purple), 25.0 km (green).	137
4.24	The parameterized stress and deceleration drag for the COARSE configuration. Total drag estimate in [-100 250] km by [15 25] km region: 46.9 kNm^{-1}	137

List of Tables

2.1	Composition of interpolation \mathcal{I} and differentiation \mathcal{D} operators for several choices of staggering, including co-located spectral elements (SE), SNFEM with Lorenz staggering (SNFEM-LOR) and SNFEM with Charney-Phillips staggering (SNFEM-ChP). Script i denotes variables defined on interfaces (Gauss-Lobatto nodes) and n represents variables defined on model levels (Gauss nodes). For operator \mathcal{I} and \mathcal{D} , the subscript denotes the target (i or n) and the superscript denotes the origin.	30
2.2	Cold wave front position ($\theta' = -1.0$ K) for all orders of accuracy and diffusion methods. Reference damping is uniform 2^{nd} order diffusion on all prognostic variables such that $\nu = 75 \text{ m}^2\text{s}^{-1}$ combined with horizontal hyperdiffusion on scalars and vertical 4^{th} order up-wind diffusion. The reference solution wave front position (finite difference method at 25 meter resolution) by Straka et al. (1993) is shown in bold (REFC) compared to the equivalent result from Tempest.	49
2.3	Numerically computed estimates of the Courant-Friedrichs-Lewy condition (maximum Courant number) using Thermal Bubble tests over a wide range of horizontal : vertical aspect ratios. The maximum wave speed corresponds to the speed of sound given by $c = \sqrt{\gamma R_d T}$ where $\gamma = 1.4$, $R_d = 286.07$, and $T = 300.5\text{K}$	60

2.4	Thermal bubble test ($\Delta x = 20$ m) average processor time taken per time step in seconds. Intel Core i7 4000 series under Linux with 4 computational cores on die (no interconnect hardware present). Results show relative scalability for Tempest using MPI architecture and IMEX partitioning with variable vertical order of accuracy. The implicit equations are solved using the GMRES with no preconditioner.	60
3.1	Background jet parameters.	82
3.2	Background thermodynamic parameters.	84
3.3	Nonlinear residuals in density ρ (kg m^{-3}) and vertical momentum ρw ($\text{kg m}^{-2} \text{s}^{-1}$) in the 3LAYER configuration.	89

Dedicado a mi esposa Kathleen, a mi
hija Maren, y a mis padres. Y también
a tí; esa parte de mi que nunca supo
darse por vencido...

Chapter 1

Introduction and Background

1.1 Non-hydrostatic vertical motion in numerical weather and climate prediction

Numerical modeling of the atmosphere begins with a detailed examination of the governing equations of fluid motion in a stratified environment. Scaling arguments based on physical reasoning or observation have led to remarkable progress (Holton and Hakim, 2012) and the various mathematical formulations have been made rigorous using variational techniques (Tort and Dubos, 2014). Ultimately, our goal is to find numerical solutions that preserve (as many or all) symmetries and invariant properties of the continuous equations in an accurate and efficient manner.

The hydrostatic approximation is one of the most important and ubiquitous simplifications made due, primarily, to the observation that vertical to horizontal aspect ratio of the synoptic atmosphere is very small. We consider the 2D vertical momentum equation in conserved Eulerian form expressed in Cartesian xz local coordinates,

$$\frac{\partial(\rho w)}{\partial t} + \frac{\partial(\rho u w)}{\partial x} + \frac{\partial(\rho w^2)}{\partial z} + \frac{1}{\rho} \frac{\partial p}{\partial z} + \rho g = 0. \quad (1.1)$$

where ρ is density, u is horizontal velocity, w is vertical velocity, p is absolute pressure, and g is the body acceleration due to gravity. If we assume that the vertical column is static and divergence of vertical momentum flux vanishes then only the following force balance remains in (1.1),

$$\frac{\partial p}{\partial z} = -\rho g. \quad (1.2)$$

This is the textbook statement of hydrostatic balance. There are several important consequences of enforcing this constraint:

1. All vertical motion depends on convergence/divergence of mass in and out of columns.
2. Vertical motion is diagnosed reducing the computational complexity of the system tremendously.

3. Vertical mixing is no longer possible and other nonlinear processes are neglected as well.

It cannot be understated how beneficial the hydrostatic approximation has been in both theoretical work over a wide range of phenomena spanning mid-latitude waves and instability through quasi-geostrophy (Holton and Hakim, 2012) and large scale tropical dynamics (Majda and Biello, 2004). However, computing hardware/software advances have partly motivated steady increases in model resolution. Coupled with a pressing need to resolve weather phenomena at local scale, most, if not all, dynamical core development worldwide is embracing the full non-hydrostatic equations as de-facto for atmospheric modeling going forward. Ullrich (2012) provides a detailed history of atmospheric model development including recent advances and trends for non-hydrostatic model development.

1.2 Spatial discretizations for non-hydrostatic models

The spatial discretization of the governing equations (Euler, Navier-Stokes, etc.) applied to geophysical flow may be separated into horizontal (on surfaces parallel to Earth's surface) and vertical (aligned with gravity) directions. Therefore, numerical methods can be considered first with respect to horizontal derivatives and typically developed for so-called Shallow Water and/or hydrostatic models. Prominent examples applied to non-hydrostatic models include the spectral element method of Patera (1984) used by Guerra and Ullrich (2016) and Giraldo, Kelly, and Constantinescu (2013a), finite volume discretizations by Ullrich and Jablonowski (2012), and the MPAS model in finite differences by Skamarock et al. (2012).

For a given flow field, if horizontal resolution approaches the vertical scale height of the virtual atmosphere, (typically 10 km or the depth of the troposphere) then non-hydrostatic effects are expected to become significant and a question emerges: what is the most efficient AND accurate discrete representation of vertical motion when combined with a given horizontal scheme?

Chapter 1. Introduction and Background

Again, for a given horizontal 2D scheme on some grid cell element (regular or deformed quadrilateral, hexagon, icosahedron, etc.), a vertical discretization is essentially a 1D model communicating quantities through each level surface and supporting transport across columns i.e. divergence. Here, a regular terrain surface following mesh of quadrilaterals connected by gravity aligned column grids is considered. Two dimensional spectral elements are used in the horizontal and a class of staggered elements (Guerra and Ullrich, 2016) deployed in the vertical column. This construction, as shown in fig. 1.1, is among the simplest encountered, is easier to implement in software, and enjoys a relatively longer history of verification and validation studies (Giraldo and Restelli, 2008). Furthermore, finite element methods are well suited to parallelization and deployment on distributed computers as calculations can be mostly contained within elements or small groups of elements.

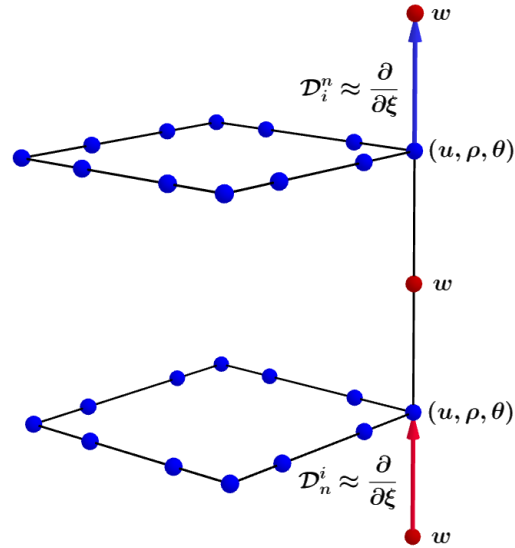


FIGURE 1.1: Spectral element and staggered vertical column element discretization. u, ρ, θ are horizontal velocity, density, and potential temperature at a model level, and w is the vertical velocity at a model interface including top and bottom boundaries. \mathcal{D} operators represent local derivatives projected from levels to interfaces \mathcal{D}_n^i and interfaces to levels \mathcal{D}_i^n .

The following set of criteria defining desirable properties of the combined spatial/temporal numerical scheme are used as guidance in this work:

1. The discretization must be numerically stable, mathematically consistent with the continuous equations, and be reliably accurate.
2. The resulting model must be fast. And execution performance must not compromise stability, consistency, or accuracy.
3. The model must be implemented in a rigorous, neatly organized, and logical fashion. It must facilitate the search for and resolution of problems as well as enable improvements readily.

Chapter 1. Introduction and Background

Chief among these concerns for atmospheric studies is that of mathematical consistency with respect to mass and/or energy conservation in a virtual atmosphere. While, almost all discretizations in use for research or in operational settings lead to mass conservation, much work is being currently done in search of discretizations that also conserve energy perfectly. Examples include the work of Dubos and Tort (2014), Thuburn, Cotter, and Dubos (2014) and Eldred and Randall (2017) where discretization is applied directly to the invariant functionals describing total energy. While there is still some debate as to the importance of energy conservation from a practical sense, this author believes such research to be significantly valuable in providing a definitive accounting of implicit and explicit energy losses i.e. that which results from the overall combined model implementation and that which is strictly a consequence of discretization error and/or dissipation terms added onto the equations. In fact, a perfectly energy conserving scheme would allow the model user to fully control any dissipation through parameterizations typically in the form of diffusion or hyper-diffusion terms.

A second, but equally important concern in atmospheric simulations is the treatment of waves. It is widely known that Earth's atmosphere supports a variety of waves at every scale from planetary and synoptic (Rossby and Kelvin waves) to meso and human scale (Bouyancy and sound waves). In fact, waves constitute one of the primary mechanisms for energy, momentum, and constituent transport in the atmosphere (Holton and Hakim, 2012). Therefore, a numerical model must have the ability to reproduce such wave action accurately over a spectrum of wavelengths as close to the grid scale length as possible. In this regard, a proposed model discretization is initially analyzed and tested in the context of linearized equation sets (Ullrich, 2014b). It has been shown, that prognostic variables cannot all be collocated on computational grid if wave dispersion is to be computed correctly. This gave rise to staggered discretizations of various forms along with discrete dispersion analyses indicating optimal configurations (Thuburn and Woollings, 2005), (Thuburn, 2006), and previously (Arakawa and Moorthi, 1988).

This work is concerned with the simulation of orographically forced gravity wave breaking

and thus utilizes a modeling system that produces internal gravity waves and follows their breakdown with high fidelity. Therefore, the numerical model used in these studies provides both accurate wave dispersion properties, and is nearly completely energy conservative allowing for a faithful representation of processes leading to unstable wave breakdown and the generation of forced stratified turbulence over mountains.

1.3 Theoretical and computational study of mountain wave breaking

Theoretical considerations of the zonally averaged general circulation using the quasi-geostrophic framework, most notably by Eliassen and Palm (1960) and also by Bretherton (1969b); Bretherton (1969a), along with numerical simulations such as those by Holton and Wehrbein (1980); Holton (1983); Zhu and Holton (1987) indicate that divergence in wave/fluctuation mean momentum flux is responsible for broad scale drag forcing on the circulation. The mechanism for such transports of momentum is the dissipation of wave energy through turbulent breakdown. The linear steady state theory of mountain waves by (Smith, 1979; Smith, 1980), and more recently reviewed by Teixeira (2014) is sufficient to establish dispersive properties of mountain waves and give estimates for amplitude growth. Furthermore, convective instability conditions that determine the onset of overturning can be derived from the linearized equations allowing a detailed understanding of the wave breaking process up to the moment instability takes place. More recent numerical studies by (Chen, Durran, and Hakim, 2005; Chen, Durran, and Hakim, 2006) have explored the transient and non-linear evolution of momentum flux profiles and their effects on synoptic scale cross flows.

While significant progress continues in understanding the dynamics of gravity wave breaking under idealized conditions over various terrain forms, a significant gap remains when these processes are incorporated into general purpose meso-scale and general circulation models. The primary reason is a lack of grid resolution over steep terrain necessary to resolve turbulent transport of breaking waves leading to drag forcing on the general circulation. Thus, this process is

Chapter 1. Introduction and Background

parameterized mechanistically based on a solution of the 2D compressible Euler equations, cast into a single variable form known as the Taylor-Goldstein equation, linearized about a mean background flow and static stratification (Nappo, 2012).

As of this writing, the Community Atmosphere Model (Neale et al., 2010) employs an Orographic Gravity Wave Drag (OGWD) parameterization based on the work of Lindzen (1981) followed by McFarlane (1987) and Palmer, J., and R. (1986). This model, as seen in fig. 1.2, enjoys several decades of testing and validation and benefits from a simple and accurate construction. However, as with any parameter scheme, there are pivotal assumptions made in the formulation: 1) the hydrostatic approximation is made in the perturbation equations, 2) input terrain is sinusoidal, and 3) incompressibility allows for velocity fields to be derived from a displacement stream function giving a precise prediction of propagation/nonpropagation regimes based on background wind and buoyancy frequency. A central question for this work is what happens to the parameterization as mean model resolution decreases from hydrostatic to nonhydrostatic scale (less than 10 km)?

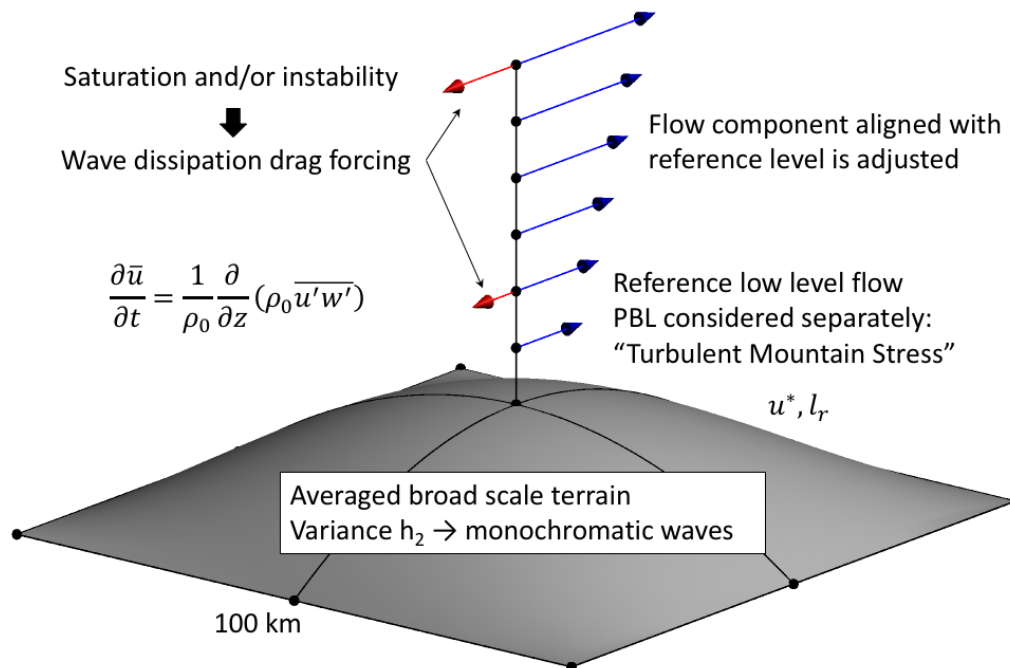


FIGURE 1.2: Schematic of the McFarlane (1987) parameterization scheme also showing turbulent stress at the base of a computational column. The equation shows the relationship between zonal mean horizontal wind \bar{u} and vertical gradient of zonal mean momentum flux covariance $u'w'$ subject to the Boussinesq approximation where only the background variation in density ρ_0 is considered.

One consequence of increased model resolution is the emergence (in terms of importance) of related but different forms of drag occurring at low level near the terrain boundary as depicted in fig. 1.3. At larger scales these processes manifest as evanescent modes that do not propagate but rapidly decay with height, however at much higher resolution, these modes become richer and produce local turbulent form drag in an increasingly well resolved boundary layer. The OGWD scheme has been augmented to incorporate some of these lower level processes by way of defining an enhanced roughness length akin to what is done in aerospace flow dynamics (Lott and Miller, 1997; Beljaars, Brown, and Wood, 2004). A detailed accounting of all the processes that

Chapter 1. Introduction and Background

determine the distribution of drag throughout the atmosphere is still not present in current operational global modeling and significant time remains before resolution increases by the order of magnitude needed to explicitly include terrain drag in a general manner.

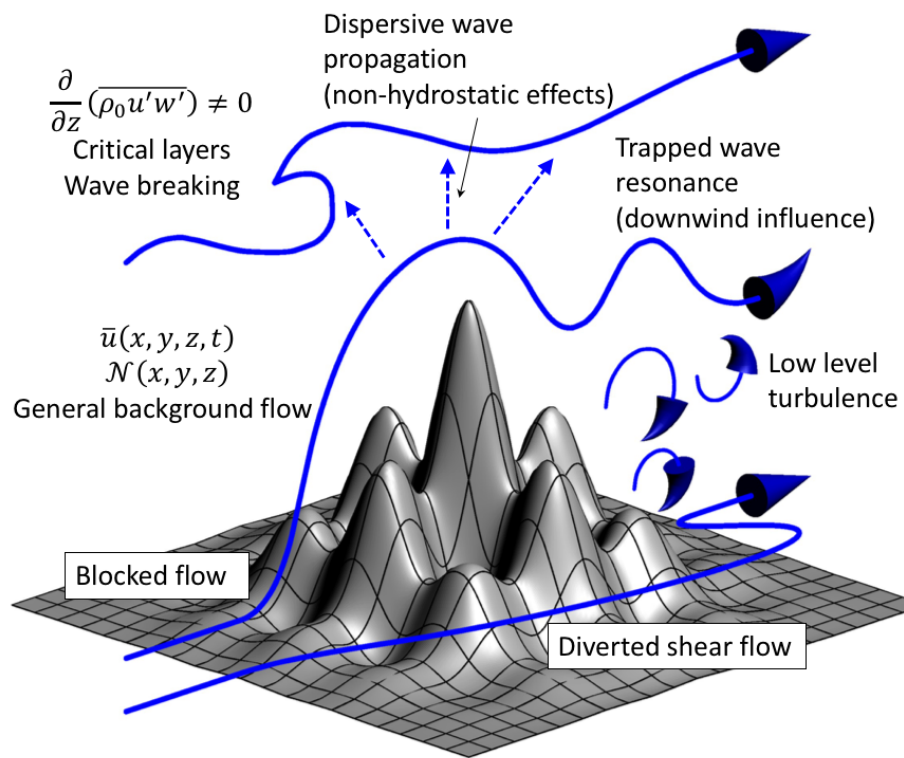


FIGURE 1.3: Schematic of dynamical processes expected as a current of air encounters mountainous terrain.

1.4 Outline of the thesis

The primary objective of this thesis is to introduce a novel numerical method for non-hydrostatic models and design test experiments to investigate the simulated behavior of breaking mountain waves at high resolution. Using detailed high-fidelity simulations of orographic waves, we then make an evaluation of an operational gravity wave drag parameterization scheme in the context of increasing model resolution. We seek to advance the detailed understanding of gravity wave breaking and inform the modeling community on appropriate development of more complete parameterization schemes that will be needed for some time to come.

The remainder of this thesis is organized as follows. In Chapter 1 we describe a novel discretization for vertical non-hydrostatic motion as part of the Tempest research dynamical core. This model combines the spectral element method on regular quadrilaterals over terrain following surfaces with a generalized arbitrary-order staggered finite element method that works with mixed polynomial spaces to achieve vertical staggering. With the numerical model implemented and tested, we proceed in Chapter 2 to design numerical experiments in the context of breaking mountain waves under general atmospheric conditions. The objective is to produce simulations that capture flow features in detail for both waves and, crucially, the transition from waves to stratified turbulence.

In Chapter 3 we present a high-fidelity simulation study of cross mountain flow using real terrain data from the Equatorial Andes. We show direct measurements of drag forcing and test the OGWD parameterization scheme at high resolution. Finally, we present conclusions from this work and future directions for this research including extending such studies to 3D with moisture and suggest other small scale phenomena related to terrain interactions that may be explored in a similar framework.

Chapter 2

A High-Order Staggered Finite-Element Vertical Discretization for Non-Hydrostatic Atmospheric Models

2.1 Introduction

The accurate representation of vertical wave motion is essential for models of the atmosphere. The vertical coordinate for the non-hydrostatic fluid equations has traditionally been discretized in the Eulerian frame via a second-order Charney-Phillips (Charney and Phillips, 1953) or Lorenz grid (Arakawa and Moorthi, 1988), or via Lagrangian layers, such as in Lin (2004). However, little work has been undertaken to develop high-order vertical discretizations due to a number of outstanding issues. First, higher-order generalizations must somehow incorporate the no-flux boundary conditions at the model bottom and top without loss of accuracy, especially near the surface where accurate treatment of dynamics is paramount. Second, as observed by Thuburn and Woollings (2005), Thuburn (2006) and Toy and Randall (2007) the choice of vertical coordinate (whether height-based, mass-based or entropy-based) implies an optimal vertical staggering of prognostic variables for maintaining correct behavior for wave motions relevant to the atmosphere. Third, unstaggered discretizations (that is, discretizations where all prognostic variables are stored on model levels) possess stationary computational modes which represent gross errors in the dispersion properties of the solution (Melvin, Staniforth, and Thuburn, 2012; Ullrich, 2014c). As in the horizontal, unstaggered FEM leads to waves with zero phase speed in the limit as the wavelength tends to $2\Delta x$, where Δx is the average grid spacing between degrees of freedom. However, unlike the horizontal, these wave modes can be dramatically enhanced by an implicit treatment of the vertical at high Courant number.

This paper describes a new discretization for the vertical that combines the accuracy of finite element methods with the desirable wave propagation properties of staggered methods. This method of vertical discretization was originally described in Ullrich and Guerra (2015), but tested using a modified set of equations and validated with a single test case. Here we extend this approach, referred to as the Staggered Nodal Finite Element Method (SNFEM), in a similar framework. Notably, this formulation is sufficiently general to be compatible with essentially any form of the fluid equations. The SNFEM discretization can be easily composed in differential

Chapter 2. The Staggered Nodal Finite-Element Method

form using interpolation and differentiation operators built in accordance with the discontinuous Galerkin and spectral element discretizations that arise from the flux reconstruction method of Huynh (2007) (see Table 2.1).

Our staggered method is similar to the mixed finite element formulations of Cotter and J. (2012) and Cotter and J. (2014) where different functional spaces are used on the prognostic fields in order to achieve desirable wave propagation and conservation properties. The SNFEM utilizes different polynomial spaces based on continuous and discontinuous grids to achieve staggered configurations. The use of SNFEM is natural for vertical discretizations, as no-flux conditions are easily imposed on top and bottom boundaries in the general finite element framework (Zienkiewicz, Taylor, and Zhu, 2005) without loss of accuracy. Further, SNFEM inherits the mimetic properties of the spectral element method so the vertical operator will automatically conserve both mass and discrete linear energy. The objectives of this paper are as follows:

1. To introduce our approach for the construction of a generalized, staggered, variable order-of-accuracy, finite element vertical discretization. We emphasize discretization of the non-conservative differential form of the Navier-Stokes equations (in vector invariant or so-called Clark form), which is independent of coordinate system.
2. To validate the implementation of this discretization within the Tempest framework using a selection of test cases in Cartesian geometry through a range of horizontal scales from 1 to 1000 km.
3. To determine the qualitative and quantitative effect of vertical order of accuracy on solutions by conducting validation experiments at coarse resolutions relative to finer reference solutions. We consider the effects of Lorenz (LOR) and Charney-Phillips (CPH) staggering both in the interior flow and at the lower boundary.
4. To determine whether a high-order vertical discretization greatly improves the simulation quality, and consequently to recommend whether there is an optimal order-of-accuracy that

Chapter 2. The Staggered Nodal Finite-Element Method

provides the best tradeoff between accuracy and computational cost.

To assess the performance of SNFEM, this discretization has been implemented in the spectral element Tempest model (Ullrich, 2014a) and run through a suite of mesoscale test cases. The test cases are as follows: Baroclinic instability in a 3D Cartesian channel of Ullrich, Reed, and Jablonowski (2015), uniform flow over the mountain of Schär et al. (2002), the density current of Straka et al. (1993), and rising thermal convective bubble tests as given in (Giraldo and Restelli, 2008). While not exhaustive, this validation suite is intended to show the treatment of waves, non-linear vertical transport, and near boundary dynamics corresponding to a high-order vertical coordinate with and without the influence of topography. Therefore, the objectives of this paper are as follows:

We will show that a high-order vertical discretization at coarse resolution more accurately approximates the reference solution relative to the low vertical order alternative when total count of degrees of freedom is kept constant. Since the interpolation and derivative operators in the finite element approach are easily expressed as linear matrix operators, there is minimal cost in adjusting the order-of-accuracy. We will present control experiments 2.4 where only the resolution and vertical order-of-accuracy vary. We leave the rigorous analysis of staggered wave modes and discrete energy conservation using the interpolation/differentiation operators for a subsequent work.

The remainder of this manuscript is as follows: Section 2.2 describes the non-hydrostatic equations of fluid motion on an arbitrary coordinate frame. Section 2.3 describes the discrete form of these equations, including the spectral element horizontal discretization, the operators used by the SNFEM vertical discretization and the time-stepping scheme employed. In section 2.4, we describe the test case suite and discuss the corresponding model results. The summary and conclusions follow in section 2.5.

2.2 The non-hydrostatic equations of fluid motion

In an arbitrary coordinate frame (α, β, ζ) , the vector velocity can be written as

$$\mathbf{u} = u^\alpha \mathbf{g}_\alpha + u^\beta \mathbf{g}_\beta + u^\zeta \mathbf{g}_\zeta, \quad (2.1)$$

where \mathbf{g}_i ($i \in \{\alpha, \beta, \zeta\}$) are the local coordinate basis vectors and u^i are the contravariant velocity components. The associated covariant components are

$$u_\alpha = \mathbf{u} \cdot \mathbf{g}_\alpha, \quad u_\beta = \mathbf{u} \cdot \mathbf{g}_\beta, \quad u_\zeta = \mathbf{u} \cdot \mathbf{g}_\zeta. \quad (2.2)$$

Covariant components can be obtained in terms of contravariant components via contraction with the covariant metric $g_{ij} = \mathbf{g}_i \cdot \mathbf{g}_j$,

$$u_i = g_{i\alpha} u^\alpha + g_{i\beta} u^\beta + g_{i\zeta} u^\zeta. \quad (2.3)$$

The reverse operation uses the contravariant metric g^{ij} , defined as the matrix inverse of the covariant metric. Contraction of the covariant components with the contravariant metric returns the contravariant vector components,

$$u^i = g^{i\alpha} u_\alpha + g^{i\beta} u_\beta + g^{i\zeta} u_\zeta. \quad (2.4)$$

The volume element J is computed in terms of the covariant metric as

$$J = \sqrt{\det g_{ij}}. \quad (2.5)$$

Using covariant horizontal velocity components, vertical velocity, potential temperature θ and

Chapter 2. The Staggered Nodal Finite-Element Method

dry air density ρ as prognostic variables, the Euler equations with shallow-atmosphere approximation can be written in an arbitrary coordinate frame as

$$\frac{\partial u_\alpha}{\partial t} = -\frac{\partial}{\partial \alpha}(K + \Phi) - \theta \frac{\partial \Pi}{\partial \alpha} + (\boldsymbol{\eta} \times \mathbf{u})_\alpha, \quad (2.6)$$

$$\frac{\partial u_\beta}{\partial t} = -\frac{\partial}{\partial \beta}(K + \Phi) - \theta \frac{\partial \Pi}{\partial \beta} + (\boldsymbol{\eta} \times \mathbf{u})_\beta, \quad (2.7)$$

$$\left(\frac{\partial r}{\partial \xi}\right) \frac{\partial w}{\partial t} = -\frac{\partial}{\partial \xi}(K + \Phi) - \theta \frac{\partial \Pi}{\partial \xi} + (\boldsymbol{\eta} \times \mathbf{u})_\xi \quad (2.8)$$

$$\frac{\partial \theta}{\partial t} = -u^\alpha \frac{\partial \theta}{\partial \alpha} - u^\beta \frac{\partial \theta}{\partial \beta} - u^\xi \frac{\partial \theta}{\partial \xi}, \quad (2.9)$$

$$\frac{\partial \rho}{\partial t} = -\frac{1}{J} \frac{\partial}{\partial \alpha}(J\rho u^\alpha) - \frac{1}{J} \frac{\partial}{\partial \beta}(J\rho u^\beta) - \frac{1}{J} \frac{\partial}{\partial \xi}(J\rho u^\xi). \quad (2.10)$$

The vertical velocity w is closely related to u_ξ via

$$w = |\mathbf{g}_\xi|^{-1} u_\xi, \quad (2.11)$$

The specific Kinetic energy is

$$K = \frac{1}{2} (u_\alpha u^\alpha + u_\beta u^\beta + u_\xi u^\xi), \quad (2.12)$$

while the geopotential function Φ is given by the product of gravitational acceleration (constant) with the elevation coordinate $r(\xi)$.

$$\Pi = c_p \left(\frac{p_0}{p}\right)^{R_d/c_p} = c_p \left(\frac{R_d \rho \theta}{p_0}\right)^{R_d/c_p}. \quad (2.13)$$

Here p_0 denotes the constant reference pressure, R_d is the ideal gas constant and c_v and c_p refer to the specific heat capacity at constant volume and pressure, respectively. The absolute vorticity vector is given by

$$\boldsymbol{\eta} = \boldsymbol{\zeta} + \boldsymbol{\omega}, \quad (2.14)$$

where the relative vorticity vector is

$$\boldsymbol{\zeta} = \frac{1}{J} \left[\left(\frac{\partial u_{\zeta}}{\partial \beta} - \frac{\partial u_{\beta}}{\partial \zeta} \right) \mathbf{g}_{\alpha} + \left(\frac{\partial u_{\alpha}}{\partial \zeta} - \frac{\partial u_{\zeta}}{\partial \alpha} \right) \mathbf{g}_{\beta} + \left(\frac{\partial u_{\beta}}{\partial \alpha} - \frac{\partial u_{\alpha}}{\partial \beta} \right) \mathbf{g}_{\zeta} \right], \quad (2.15)$$

and, under the shallow-atmosphere approximation, the planetary vorticity vector is

$$\boldsymbol{\omega} = f(\partial r / \partial \zeta)^{-1} \mathbf{g}_{\zeta}. \quad (2.16)$$

Consequently, the rotational terms in the equation of motion take the form

$$(\boldsymbol{\eta} \times \mathbf{u})_{\alpha} = J \left[u^{\beta} (\omega^{\zeta} + \zeta^{\zeta}) - u^{\zeta} \zeta^{\beta} \right], \quad (2.17)$$

$$(\boldsymbol{\eta} \times \mathbf{u})_{\beta} = J \left[u^{\zeta} \zeta^{\alpha} - u^{\alpha} (\omega^{\zeta} + \zeta^{\zeta}) \right], \quad (2.18)$$

$$(\boldsymbol{\eta} \times \mathbf{u})_{\zeta} = J \left[u^{\alpha} \zeta^{\beta} - u^{\beta} \zeta^{\alpha} \right]. \quad (2.19)$$

Note that this formulation does not specify a coordinate system. Consequently, these equations can be used for either Cartesian or spherical geometry. To account for topography, terrain-following σ -coordinates are imposed by defining the radius $r = r(\alpha, \beta, \zeta)$ so that $r(\alpha, \beta, 0)$ is coincident with the surface. For example, Gal-Chen and Somerville (1975) coordinates arise from the choice

$$r(\alpha, \beta, \zeta) = \zeta [r_{top} - r_s(\alpha, \beta)] + r_e + r_s(\alpha, \beta), \quad (2.20)$$

where r_{top} denotes the model height and $r_s(\alpha, \beta)$ denotes the surface elevation from the mean Earth radius r_e . In Cartesian coordinates r simply maps to the elevation z while neglecting the mean radius r_e in (2.20). The symmetric covariant and contravariant metric tensors in the (α, β, r)

Cartesian system are written as

$$g^{ij} = \begin{pmatrix} 1 & 0 & -\left(\frac{\partial r}{\partial \zeta}\right)^{-1} \left(\frac{\partial r}{\partial \alpha}\right) \\ & 1 & -\left(\frac{\partial r}{\partial \zeta}\right)^{-1} \left(\frac{\partial r}{\partial \beta}\right) \\ & & \left(\frac{\partial r}{\partial \zeta}\right)^{-2} \left[1 + \left(\frac{\partial r}{\partial \alpha}\right)^2 + \left(\frac{\partial r}{\partial \beta}\right)^2\right] \end{pmatrix} : i, j = (\alpha, \beta, \zeta) \quad (2.21)$$

and

$$g_{ij} = \begin{pmatrix} \left[1 + \left(\frac{\partial r}{\partial \alpha}\right)^2\right] & \frac{\partial r}{\partial \alpha} \frac{\partial r}{\partial \beta} & \frac{\partial r}{\partial \alpha} \frac{\partial r}{\partial \zeta} \\ & \left[1 + \left(\frac{\partial r}{\partial \beta}\right)^2\right] & \frac{\partial r}{\partial \beta} \frac{\partial r}{\partial \zeta} \\ & & \left(\frac{\partial r}{\partial \zeta}\right)^2 \end{pmatrix} : i, j = (\alpha, \beta, \zeta) \quad (2.22)$$

We note that in this framework, the discretization is decoupled from the grid definition. As such, Tempest is designed to target flows on the sphere and in Cartesian domains simultaneously with or without terrain. This is convenient in the analysis, implementation, and validation of the numerical techniques that follow. We focus our validation on Cartesian cases and will address test cases on the sphere in a subsequent publication based on the same discretization framework. Lastly, derivatives of the vertical coordinate in α and β are evaluated using the discrete derivative operators developed in the next section while the vertical gradient of coordinate surfaces can easily be obtained analytically from (2.20).

2.3 Discretization

2.3.1 Horizontal Discretization

The horizontal discretization of (2.6)-(2.10) follows the continuous element formulation of Ullrich (2014a), which is analogous to earlier efforts with spectral elements (Giraldo and Rosmond, 2004;

Taylor and Fournier, 2010; Dennis et al., 2011; Giraldo, Kelly, and Constantinescu, 2013b) with coordinate information completely contained in the definition of the metric tensors (2.21) and (2.22).

2.3.2 Vertical Discretization

Each vertical column consists of n_{ve} nodal finite elements, indexed $a \in \{0, \dots, n_{ve} - 1\}$. Throughout this manuscript, all vertical indices are assumed to increase with altitude. Within each element, levels are placed at the n_{vp} Gaussian quadrature nodes and interfaces at $n_{vp} + 1$ Gauss-Lobatto quadrature nodes, leading to a staggering of levels and interfaces. With vertical coordinate ξ , the location of model levels denoted $\xi_{a,k}$ with $k \in \{0, \dots, n_{vp} - 1\}$ and model interfaces denoted $\tilde{\xi}_{a,k}$ with $k \in \{0, \dots, n_{vp}\}$. Each finite element is then bounded within the interval $[\tilde{\xi}_{a,0}, \tilde{\xi}_{a,n_{vp}}]$ with two associated sets of basis functions – one over model levels, denoted by the set $\phi_a = \{\phi_{a,j} | j = 0, \dots, n_{vp} - 1\}$ that includes characteristic polynomials of degree $n_{vp} - 1$, and one over model interfaces, denoted by the set $\tilde{\phi}_a = \{\tilde{\phi}_{a,j} | j = 0, \dots, n_{vp} - 1\}$ that includes characteristic polynomials of degree n_{vp} . A depiction of the vertical staggering associated with levels and interfaces is given in fig. 2.1, along with basis functions in each case. A scalar field $q(\xi, t)$ can then be written approximately, either as a linear combination of basis functions on levels,

$$q(\xi, t) \approx \sum_{a=0}^{n_{ve}-1} \sum_{j=0}^{n_{vp}-1} q_{a,j}(t) \phi_{a,j}(\xi), \quad (2.23)$$

or on interfaces,

$$q(\xi, t) \approx \sum_{a=0}^{n_{ve}-1} \sum_{j=0}^{n_{vp}} \tilde{q}_{a,j}(t) \tilde{\phi}_{a,j}(\xi). \quad (2.24)$$

For the remainder of this manuscript we will use script n to denote variables stored on model levels and script i to denote variables stored on interfaces.

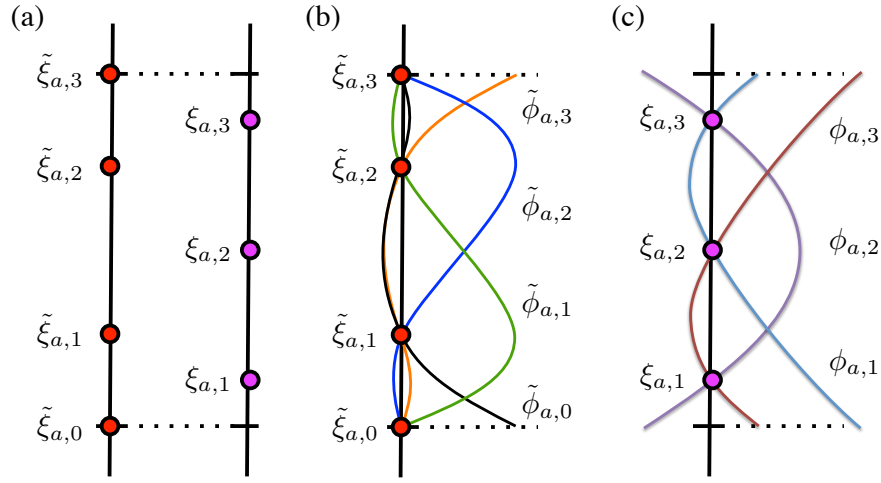


FIGURE 2.1: (a) Vertical placement of (left) Gauss-Lobatto nodes and (right) Gauss nodes within a vertical element with $n_{vp} = 3$. (b) Basis functions $\tilde{\phi}_{a,k}$ for Gauss-Lobatto nodes within element a . (c) Basis functions $\phi_{a,k}$ for Gauss nodes within element a .

Interpolation Operators

Note that (2.23) and (2.24) are not equivalent discretizations since (2.23) cannot represent polynomials of degree n_{vp} and (2.24) cannot represent fields that are discontinuous at element interfaces. Nonetheless, we can define interpolation operators between these fields via \mathcal{I}_i^n , representing interpolation from levels to interfaces, and \mathcal{I}_n^i , representing interpolation from interfaces to nodes. First, interpolation from interfaces to levels is defined as

$$(\mathcal{I}_n^i \tilde{\mathbf{q}})_{a,k} = \sum_{j=0}^{n_{vp}} \tilde{q}_{a,j}(t) \tilde{\phi}_{a,j}(\xi_{a,k}). \quad (2.25)$$

To define the interpolant from levels to interfaces, a two-step procedure is employed. Since basis functions on levels are discontinuous, we define the left and right interpolants at element

boundaries as

$$(\mathcal{I}_L^n \mathbf{q})_{a,0} = \sum_{j=0}^{n_{vp}-1} q_{a,j} \phi_{a,j}(\tilde{\xi}_{a,0}), \quad (\mathcal{I}_R^n \mathbf{q})_{a,n_{vp}-1} = \sum_{j=0}^{n_{vp}-1} q_{a,j} \phi_{a,j}(\tilde{\xi}_{a,n_{vp}-1}) \quad (2.26)$$

and then define the total interpolant as

$$(\mathcal{I}_i^n \mathbf{q})_{a,k} = \begin{cases} \sum_{j=0}^{n_{vp}-1} q_{a,j} \phi_{a,j}(\tilde{\xi}_{a,k}) & \text{if } 0 < k < n_{vp}, \\ \frac{1}{2}(\mathcal{I}_R^n \mathbf{q})_{a-1,n_{vp}-1} + \frac{1}{2}(\mathcal{I}_L^n \mathbf{q})_{a,0} & \text{if } k = 0, \\ \frac{1}{2}(\mathcal{I}_R^n \mathbf{q})_{a,n_{vp}-1} + \frac{1}{2}(\mathcal{I}_L^n \mathbf{q})_{a+1,0} & \text{if } k = n_{vp}. \end{cases} \quad (2.27)$$

These interpolation operators can also be obtained from equivalence via the variational (weak) form. At model interfaces, the accuracy of (2.27) degrades for unequally spaced finite elements. For the case of stacked finite elements with unequal thickness $\Delta\tilde{\xi}_a = \tilde{\xi}_{a,n_{vp}} - \tilde{\xi}_{a,0}$, a more accurate formula can be obtained from

$$(\mathcal{I}_i^n \mathbf{q})_{a,0} = \frac{\Delta\tilde{\xi}_a^{n_{vp}} (\mathcal{I}_R^n \mathbf{q})_{a-1,n_{vp}-1} + \Delta\tilde{\xi}_{a-1}^{n_{vp}} (\mathcal{I}_L^n \mathbf{q})_{a,0}}{\Delta\tilde{\xi}_a^{n_{vp}} + \Delta\tilde{\xi}_{a-1}^{n_{vp}}}, \quad (2.28)$$

which arises on noting that the one-sided interpolant has error $O(\Delta\tilde{\xi}_a^{n_{vp}})$.

Differentiation Operators

Differentiation is required for all combinations of model levels and interfaces: \mathcal{D}_i^i represents differentiation from interfaces to interfaces, \mathcal{D}_n^i represents differentiation from interfaces to levels, \mathcal{D}_n^n denotes differentiation from levels to levels and \mathcal{D}_i^n denotes differentiation from levels to interfaces. A depiction of the behavior of these derivative operators is shown in fig. 2.2.

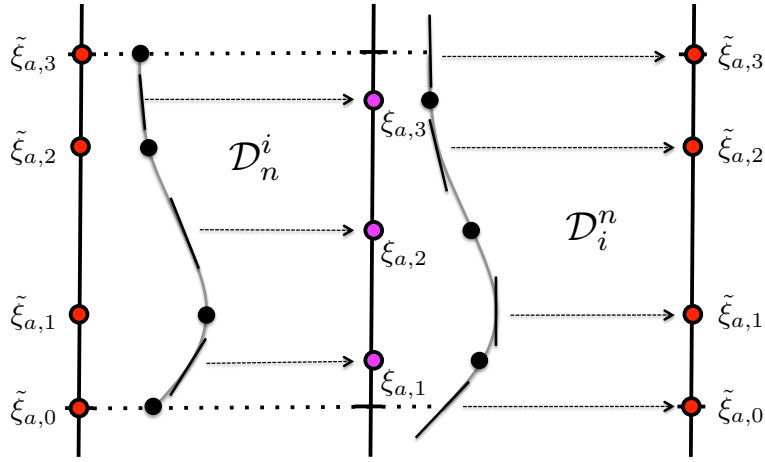


FIGURE 2.2: A depiction of the derivative operators \mathcal{D}_n^i and \mathcal{D}_i^n , which remap from interfaces to levels and levels to interfaces, respectively. The gray line depicts a typical field variable within element a that emerges from the expansion (left) (2.24) or (center) (2.23).

Differentiation from interfaces to levels is obtained by simply differentiating (2.25),

$$(\mathcal{D}_n^i \mathbf{q})_{a,k} = \sum_{j=0}^{n_{vp}} \tilde{q}_j \frac{\partial \tilde{\phi}_j}{\partial \tilde{\xi}}(\tilde{\xi}_{a,k}). \quad (2.29)$$

This works in practice as there is an exact mapping from derivatives of the continuous polynomial space (over interfaces) to the discontinuous polynomial space (over levels).

Differentiation from levels to levels is computed via the composed operator

$$\mathcal{D}_n^n \mathbf{q} = \mathcal{D}_n^i \mathcal{I}_i^n \mathbf{q}, \quad (2.30)$$

where boundary conditions, such as the no flux condition ($u^\xi = 0$) at the top and bottom, are enforced after application of the interpolation operator.

Differentiation from interfaces to interfaces requires averaging the one-sided derivatives at element interfaces, but is otherwise simply the derivative of (2.25) on the element interior,

$$(\mathcal{D}_i^i \mathbf{q})_{a,k} = \begin{cases} \frac{1}{2} \left(\sum_{j=0}^{n_{vp}} \tilde{q}_{a,j} \frac{\partial \tilde{\phi}_{a,j}}{\partial \tilde{\xi}}(\tilde{\xi}_{a,k}) + \sum_{j=0}^{n_{vp}} \tilde{q}_{a-1,j} \frac{\partial \tilde{\phi}_{a-1,j}}{\partial \tilde{\xi}}(\tilde{\xi}_{a,k}) \right) & \text{if } k = 0, \\ \sum_{j=0}^{n_{vp}} \tilde{q}_{a,j} \frac{\partial \tilde{\phi}_{a,j}}{\partial \tilde{\xi}}(\tilde{\xi}_{a,k}) & \text{if } 0 < k < n_{vp}, \\ \frac{1}{2} \left(\sum_{j=0}^{n_{vp}} \tilde{q}_{a,j} \frac{\partial \tilde{\phi}_{a,j}}{\partial \tilde{\xi}}(\tilde{\xi}_{a,k}) + \sum_{j=0}^{n_{vp}} \tilde{q}_{a+1,j} \frac{\partial \tilde{\phi}_{a+1,j}}{\partial \tilde{\xi}}(\tilde{\xi}_{a,k}) \right) & \text{if } k = n_{vp}. \end{cases} \quad (2.31)$$

Differentiation from levels to interfaces (\mathcal{D}_i^n) should not be defined via the composition $\mathcal{D}_i^i \mathcal{I}_i^n$ since this procedure would introduce a non-zero null space that can trigger an unphysical computational mode in the discrete equations. Instead we define \mathcal{D}_i^n using the robust differentiation technique discussed in Ullrich (2014a), based on the flux reconstruction methods of Huynh (2007). This strategy leads to the discrete operator

$$\begin{aligned} (\mathcal{D}_i^n \mathbf{q})_{a,k} &= (\hat{\mathcal{D}}_i^n \mathbf{q})_{a,k} + \frac{1}{2} \frac{dG_R}{d\tilde{\xi}}(\tilde{\xi}_{a,k}) [(\mathcal{I}_L^n \mathbf{q})_{a+1,k} - (\mathcal{I}_R^n \mathbf{q})_{a,k}] \\ &\quad + \frac{1}{2} \frac{dG_L}{d\tilde{\xi}}(\tilde{\xi}_{a,k}) [(\mathcal{I}_R^n \mathbf{q})_{a-1,k} - (\mathcal{I}_L^n \mathbf{q})_{a,k}], \end{aligned} \quad (2.32)$$

where

$$(\hat{\mathcal{D}}_i^n \mathbf{q})_{a,k} = \begin{cases} \frac{1}{2} \left(\sum_{j=0}^{n_{vp}-1} q_{a,j} \frac{\partial \phi_{a,j}}{\partial \tilde{\xi}}(\tilde{\xi}_{a,k}) + \sum_{j=0}^{n_{vp}-1} q_{a-1,j} \frac{\partial \phi_{a-1,j}}{\partial \tilde{\xi}}(\tilde{\xi}_{a,k}) \right) & \text{if } k = 0, \\ \sum_{j=0}^{n_{vp}-1} q_{a,j} \frac{\partial \phi_{a,j}}{\partial \tilde{\xi}}(\tilde{\xi}_{a,k}) & \text{if } 0 < k < n_{vp}, \\ \frac{1}{2} \left(\sum_{j=0}^{n_{vp}-1} q_{a,j} \frac{\partial \phi_{a,j}}{\partial \tilde{\xi}}(\tilde{\xi}_{a,k}) + \sum_{j=0}^{n_{vp}-1} q_{a+1,j} \frac{\partial \phi_{a+1,j}}{\partial \tilde{\xi}}(\tilde{\xi}_{a,k}) \right) & \text{if } k = n_{vp}, \end{cases} \quad (2.33)$$

and G_L and G_R are the local flux correction functions, which are chosen to satisfy

$$G_L(\xi_{a,0}) = 1, \quad G_L(\xi_{a,n_{vp}-1}) = 0, \quad G_R(\xi_{a,0}) = 0, \quad G_R(\xi_{a,n_{vp}-1}) = 1, \quad (2.34)$$

Chapter 2. The Staggered Nodal Finite-Element Method

and otherwise approximate zero throughout $[\xi_{a,0}, \xi_{a,n_{vp}-1}]$.

There is some flexibility in the discretization that depends on the specific choice of flux correction functions. Huynh (2007) gives a family of flux correction functions on the interval $[-1, 1]$ denoted by G_k for $k = 1, 2, \dots$. In particular, we are interested in G_1 (the Radau polynomials) and G_2 , which have the special property that $dG_2/dx = 0$ at all Gauss-Lobatto points. Although either choice of flux correction function leads to a valid discretization for $n_{vp} > 1$, when $n_{vp} = 1$ a consistent differential operator is recovered only with G_2 . Hence, for the remainder of this text we will adopt the flux correction function G_2 . For this choice, the flux correction function satisfies

$$\frac{\partial G_2}{\partial x} = \frac{(n_{vp} + 1) [P_{n_{vp}+1}(x) - xP_{n_{vp}}(x)]}{2(x-1)}, \quad (2.35)$$

where $P_N(x)$ is the Legendre polynomial of order N . In the limit as x approaches the boundaries of the reference element, a simplified expression emerges:

$$\lim_{x \rightarrow +1} \frac{\partial G_2}{\partial x} = n_{vp}(n_{vp} + 1). \quad (2.36)$$

On the interval $[\tilde{\xi}_{j,0}, \tilde{\xi}_{j,n_{vp}-1}]$ we have

$$\frac{\partial G_R}{\partial \tilde{\xi}}(\tilde{\xi}) = \frac{1}{\Delta \tilde{\xi}_a} \frac{\partial G_2}{\partial x} \left[\frac{2(\tilde{\xi} - \tilde{\xi}_{j,0})}{\Delta \tilde{\xi}_a} - 1 \right], \quad \frac{\partial G_L}{\partial \tilde{\xi}}(\tilde{\xi}) = -\frac{1}{\Delta \tilde{\xi}_a} \frac{\partial G_2}{\partial x} \left[\frac{2(\tilde{\xi}_{j,n_{vp}-1} - \tilde{\xi})}{\Delta \tilde{\xi}_a} - 1 \right]. \quad (2.37)$$

Second Derivative Operators in the Vertical

The second derivative operators are used in viscosity and hyperviscosity calculations. They are obtained as approximations to the equation

$$\mathcal{L}(\nu) \mathbf{q} \approx \nu \frac{\partial^2 q}{\partial \tilde{\xi}^2}, \quad (2.38)$$

subject to Neumann (no-flux) boundary condition

$$\frac{\partial q}{\partial \zeta} = 0 \quad \text{at } \zeta = 0 \text{ and } \zeta = 1. \quad (2.39)$$

For the viscous operator from interfaces to interfaces, the discretization is obtained from the variational (weak) formulation. Specifically, from (2.38) and integration by parts,

$$\int_0^1 (\mathcal{L}_i^i \mathbf{q})_{b,n} \tilde{\phi}_{a,k} d\zeta = \left. \frac{\partial q}{\partial \zeta} \tilde{\phi}_{a,k} \right|_0^1 - \int_0^1 \frac{\partial q}{\partial \zeta} \frac{\partial \tilde{\phi}_{a,k}}{\partial \zeta} d\zeta. \quad (2.40)$$

Then using (2.24), (2.39) and the assumption of orthogonality of basis functions $\tilde{\phi}$ under quadrature,

$$(\mathcal{L}_i^i \mathbf{q})_{a,k} = -\frac{1}{\int_0^1 \tilde{\phi}_{a,k}^2 d\zeta} \sum_{b=0}^{n_{ve}-1} \sum_{n=0}^{n_{vp}} \tilde{q}_{b,n} \int_0^1 \frac{\partial \tilde{\phi}_{a,k}}{\partial \zeta} \frac{\partial \tilde{\phi}_{b,n}}{\partial \zeta} d\zeta. \quad (2.41)$$

For model interfaces on Gauss-Lobatto nodes, the integral is discretized via Gauss-Lobatto quadrature.

The viscous operator from levels to levels is derived in a similar manner, although the non-differentiability of q at interfaces in the discontinuous basis means that we must rely on differentiation via (2.32). Consequently, the weak form

$$\int_{\tilde{\zeta}_{a,0}}^{\tilde{\zeta}_{a,vnp}} (\mathcal{L}_i^i \mathbf{q})_{b,n} \phi_{a,k} d\zeta = \left. \frac{\partial q}{\partial \zeta} \phi_{a,k} \right|_{\tilde{\zeta}_{a,0}}^{\tilde{\zeta}_{a,vnp}} - \int_{\tilde{\zeta}_{a,0}}^{\tilde{\zeta}_{a,vnp}} \frac{\partial q}{\partial \zeta} \frac{\partial \phi_{a,k}}{\partial \zeta} d\zeta. \quad (2.42)$$

then leads to discrete operator

$$(\mathcal{L}_n^n \mathbf{q})_{a,k} = \frac{1}{\int_{\tilde{\zeta}_{a,0}}^{\tilde{\zeta}_{a,vnp}} \phi_{a,k}^2 d\zeta} [(\hat{\mathcal{L}}_n^n \mathbf{q})_{a,k} + (\mathcal{D}_i^n \mathbf{q})_{a,vnp} \phi(\tilde{\zeta}_{a,vnp}) - (\mathcal{D}_i^n \mathbf{q})_{a,0} \phi(\tilde{\zeta}_{a,0})], \quad (2.43)$$

where

$$(\hat{\mathcal{L}}_n^n \mathbf{q})_{a,k} = - \sum_{b=0}^{n_{ve}-1} \sum_{n=0}^{n_{vp}-1} q_{b,n} \int_{\tilde{\xi}_{a,0}}^{\tilde{\xi}_{a,n_{vp}}} \frac{\partial \phi_{a,k}}{\partial \tilde{\xi}} \frac{\partial \phi_{b,n}}{\partial \tilde{\xi}} d\tilde{\xi}. \quad (2.44)$$

For model levels on Gauss nodes, the integral is discretized directly via Gaussian quadrature. Note that the boundary condition implies that we must impose

$$(\mathcal{D}_i^n \mathbf{q})_{0,0} = 0 \quad \text{and} \quad (\mathcal{D}_i^n \mathbf{q})_{v_{ne}-1, v_{np}} = 0. \quad (2.45)$$

Flow-dependent vertical hyperviscosity

The basic spectral element method is an energy conservative scheme (Taylor and Fournier, 2010) that allows for the accumulation of energy at the shortest wavelengths. Following Ullrich (2014a) and Dennis et al. (2011), we impose explicit dissipation in the horizontal using a constant coefficient hyperviscosity. In the vertical, a constant coefficient hyperviscosity would have a rapid and adverse affect on hydrostatic balance in the absence of a hydrostatic reference state (Giraldo and Restelli, 2008). Consequently, in this paper we apply a localized hyperviscosity in the vertical column that is weighted by the contravariant vertical flow velocity $u^{\tilde{\xi}}$,

$$\frac{\partial q}{\partial t} = \dots + v_z |u^{\tilde{\xi}}| \frac{\partial^{2k} q}{\partial \tilde{\xi}^{2k}}, \quad (2.46)$$

where $q \in \{u_\alpha, u_\beta, w, \theta, \rho\}$ and k is a positive integer. The motivation for using $u^{\tilde{\xi}}$ stems from the observation that advective transport in the vertical occurs with speed $u^{\tilde{\xi}}$, and so this would be the corresponding wave speed that would enter into, for example, the Rusanov Riemann solver in the context of discontinuous Galerkin or finite volume methods. In this sense, the flow-dependent hyperviscosity is a generalization of advective up-winding if applied simultaneously with the vertical advective operator. The Riemann solver interpretation also yields an appropriate estimate

for the value of v_z ,

$$\begin{aligned}
 k = 2 : \quad v_z &= (1/2)(\overline{\Delta\xi})^{-1}, \\
 k = 4 : \quad v_z &= -(1/12)(\overline{\Delta\xi})^{-3}, \\
 k = 6 : \quad v_z &= (1/60)(\overline{\Delta\xi})^{-5},
 \end{aligned}
 \tag{2.47}$$

where $\overline{\Delta\xi} = 1/(an_{vp})$ is the average spacing between nodes in the vertical direction.

The Staggered Nodal Finite Element Method (SNFEM)

The interpolation and differentiation operators given in the previous sections provide a framework for constructing staggered vertical grids in the context of the nonlinear system (2.6)-(2.10). Furthermore, the SNFEM allows for discretizations of arbitrary order-of-accuracy via adjustments in n_{vp} . For the present work, we investigate unstaggered (on interfaces), Lorenz (LOR) (u, v, ρ, θ on levels, w on interfaces), and Charney-Phillips (CPH) (u, v, ρ on levels, w, θ on interfaces) configurations. The two key diagnosed variables, Π and u^ξ are co-located with ρ and w respectively. Table 2.1 provides a reference nomenclature for the various discrete derivative operators that arise in the SNFEM corresponding to the terms treated implicitly. In general, we will use subscripts and superscripts i and n denote quantities computed on “interfaces” or “levels” respectively. When needed, the contravariant α and ξ velocity are computed via

$$(u^j) = g^{j\alpha}(u_\alpha) + g^{j\beta}(u_\beta) + g^{j\xi}|\mathbf{g}_\xi|w,
 \tag{2.48}$$

where $j \in \{\alpha, \xi\}$ and all covariant velocities are first interpolated to levels or interfaces (wherever u^j is needed) prior to evaluation.

For example, applying the discrete derivative operators with Lorenz staggering to (2.6)-(2.10) and neglecting flow in the β direction gives:

$$\frac{\partial(u_\alpha)_n}{\partial t} = -\mathcal{D}_\alpha(K_n + \Phi_n) - \theta_n \mathcal{D}_\alpha(\Pi_n) - (u^\xi)_n \left[\mathcal{D}_n^n u_\alpha - \mathcal{D}_\alpha \mathcal{I}_n^i(u_\xi)_i \right], \quad (2.49)$$

$$\left(\frac{\partial r}{\partial \xi} \right)_i \frac{\partial w_i}{\partial t} = -\mathcal{D}_i^n (K_n + \Phi_n) - \mathcal{I}_i^n \theta_n (\mathcal{D}_i^n \Pi_n) + (u^\alpha)_i \mathcal{D}_n^i u_\alpha - \mathcal{I}_i^n \left[(u^\alpha)_n \mathcal{D}_\alpha \mathcal{I}_n^i(u_\xi)_i \right] \quad (2.50)$$

$$\frac{\partial \theta_n}{\partial t} = -(u^\alpha)_n (\mathcal{D}_\alpha \theta_n) - \left[\mathcal{I}_n^i(u^\xi)_i \right] (\mathcal{D}_n^n \theta_n), \quad (2.51)$$

$$\frac{\partial \rho_n}{\partial t} = -\frac{1}{J_n} \mathcal{D}_\alpha [J_n \rho_n (u^\alpha)_n] - \frac{1}{J_n} \mathcal{D}_n^i [J_i (\mathcal{I}_i^n \rho_n) (u^\xi)_i]. \quad (2.52)$$

Here the vertical interpolation operators are defined in section 2.3.2, the derivative operators are defined in section 2.3.2, and the horizontal derivative operator \mathcal{D}_α represents the standard co-located spectral element derivative operator.

It is important to note the great deal of flexibility available in the computation of spatial terms in eqs. (2.49) - (2.52). In particular, covariant/contravariant velocity components (needed in the advection of θ) and the specific kinetic energy K may be composed with different interpolation sequences and preliminary experiments have suggested that stability of the method may depend on such variations, particularly in the presence of steep topography.

Variable	Term	Choice of Staggering		
		SE (ρ_i, θ_i, w_i)	SNFEM-LOR (ρ_n, θ_n, w_i)	SNFEM-ChP (ρ_n, θ_i, w_i)
u, v	Π	$\Pi_i(\rho_i, \theta_i)$	$\Pi_n(\rho_n, \theta_n)$	$\Pi_n(\rho_n, \mathcal{I}_n^i \theta_i)$
θ	$u^\xi \frac{\partial \theta}{\partial \xi}$	$(u_i^\xi) \mathcal{D}_i^i \theta_i$	$(\mathcal{I}_n^i u_i^\xi) (\mathcal{D}_n^n \theta)$	$(u_i^\xi) (\mathcal{D}_i^i \theta_i)$
w	$\theta \frac{\partial \Pi}{\partial \xi}$	$\theta_i \mathcal{D}_i^i \Pi_i$	$(\mathcal{I}_n^i \theta_n) (\mathcal{D}_i^n \Pi_n)$	$\theta_i (\mathcal{D}_i^n \Pi_n)$
ρ	$\frac{1}{J} \frac{\partial}{\partial \xi} (J \rho u^\xi)$	$\frac{1}{J_i} \mathcal{D}_i^i (J_i \rho_i u_i^\xi)$	$\frac{1}{J_n} \mathcal{D}_n^i [J_i (\mathcal{I}_n^i \rho_n) u_i^\xi]$	$\frac{1}{J_n} \mathcal{D}_n^i [J_i (\mathcal{I}_n^i \rho_n) u_i^\xi]$

TABLE 2.1: Composition of interpolation \mathcal{I} and differentiation \mathcal{D} operators for several choices of staggering, including co-located spectral elements (SE), SNFEM with Lorenz staggering (SNFEM-LOR) and SNFEM with Charney-Phillips staggering (SNFEM-ChP). Script i denotes variables defined on interfaces (Gauss-Lobatto nodes) and n represents variables defined on model levels (Gauss nodes). For operator \mathcal{I} and \mathcal{D} , the subscript denotes the target (i or n) and the superscript denotes the origin.

2.3.3 Temporal Discretization

Many options are available for the temporal discretization of the semi-discrete equations, including several fully explicit and implicit-explicit schemes (Ascher, Ruuth, and Spiteri, 1997). One simple temporal discretization is investigated here, which utilizes Strang splitting for the dynamics and operator splitting for the hyperviscosity. The equations (2.6)-(2.10) are written in the form

$$\frac{\partial \psi}{\partial t} - f(\mathbf{x}, \psi) = g(\mathbf{x}, \psi), \quad (2.53)$$

where $f(\mathbf{x}, \psi)$ denotes terms associated with non-stiff modes, *i.e.* horizontally-propagating modes and vertical advection of horizontal velocity. The function $g(\mathbf{x}, \psi)$ denotes geometrically stiff terms associated with all vertical derivatives except for vertical advection of horizontal velocity. The model follows the approach of Ullrich and Jablonowski (2012) by treating non-stiff terms using an explicit temporal operator and stiff terms using an implicit operator. For the current study,

Chapter 2. The Staggered Nodal Finite-Element Method

the terms highlighted in red in eqs. (2.49) - (2.52) are treated implicitly in order to avoid timestep limitations due to vertically propagating sound waves.

For the first time step, an implicit update is applied,

$$\psi^{(0)} = \psi^n + \frac{\Delta t}{2} (\mathcal{I} - \frac{\Delta t}{2} \mathcal{D}\mathcal{G}(\psi^n))^{-1} \mathcal{G}(\psi^n), \quad (2.54)$$

where $\mathcal{G}(\psi^n)$ represents the discretization described in section 2.3.2 and $\mathcal{D}\mathcal{G}(\psi^n) = \partial\mathcal{G}/\partial\psi^n$. For later time steps, the implicit update is instead obtained from a stored tendency,

$$\psi^{(0)} = \psi^n + \frac{\Delta t}{2} \bar{\psi}. \quad (2.55)$$

Explicit terms are evolved using a Runge-Kutta method which supports a large stability bound for spatial discretizations with purely imaginary eigenvalues. This particular scheme is based on Kinnmark and Gray (1984b); Kinnmark and Gray (1984a) and takes the form

$$\begin{aligned} \psi^{(1)} &= \psi^{(0)} + \frac{\Delta t}{5} f(\psi^{(0)}), \\ \psi^{(2)} &= \psi^{(0)} + \frac{\Delta t}{5} f(\psi^{(1)}), \\ \psi^{(3)} &= \psi^{(0)} + \frac{\Delta t}{3} f(\psi^{(2)}), \\ \psi^{(4)} &= \psi^{(0)} + \frac{2\Delta t}{3} f(\psi^{(3)}), \\ \psi^{(5)} &= -\frac{1}{4}\psi^{(0)} + \frac{5}{4}\psi^{(1)} + \frac{3\Delta t}{4} f(\psi^{(4)}). \end{aligned} \quad (2.56)$$

Hyperviscosity is then applied in accordance with Ullrich (2014a), with scalar hyperviscosity used for all scalar quantities and vector hyperviscosity used for the horizontal velocity field. Mathematically, the update takes the form,

$$\psi_s^{(6)} = \psi_s^{(5)} + \Delta t \mathcal{H}(v) \mathcal{H}(1) \psi_s^{(5)}, \quad (2.57)$$

$$\mathbf{u}^{(6)} = \mathbf{u}^{(5)} + \Delta t \mathcal{H}(v_d, v_v) \mathcal{H}(1, 1) \mathbf{u}^{(5)}, \quad (2.58)$$

Chapter 2. The Staggered Nodal Finite-Element Method

where $\psi_s \in \{\theta, w, \rho\}$.

When active, Rayleigh friction is applied via backward Euler to relax all prognostic variables to a specified reference state,

$$\psi^{(7)} = \gamma\psi^{(6)} + (1 - \gamma)\psi^{\text{ref}}, \quad (2.59)$$

where $\gamma = [1 + \nu_r(\mathbf{x})\Delta t]^{-1}$ is in terms of the Rayleigh friction strength $\nu_r(\mathbf{x})$.

In accordance with Strang splitting, a final implicit update is applied,

$$\bar{\psi} = (\mathcal{I} - \frac{\Delta t}{2}\mathcal{D}\mathcal{G}(\psi^{(7)}))^{-1}\mathcal{G}(\psi^{(7)}), \quad (2.60)$$

$$\psi^{n+1} = \psi^{(7)} + \frac{\Delta t}{2}\bar{\psi}. \quad (2.61)$$

2.4 Validation

In this section we present a set of test cases with the purpose of investigating the performance of the SNFEM for mesoscale atmospheric modeling. Our emphasis is on a wide range of resolutions from the global scale (200 km) to the large eddy scale (5 m). These scales transition from hydrostatic to scales where all non-linear terms in the equations (2.6) - (2.10) become significant. For our experiments we will hold the following components of the computations constant:

- (1) The horizontal discretization is kept as a standard 4th order spectral element formulation for all simulations, as outlined in section 2.3.1.
- (2) The time integration scheme is based on Strang-split IMplicit EXplicit (IMEX) outlined in section 2.3.3.
- (3) Vertical terms $\frac{\partial}{\partial z}$ are integrated implicitly using the generalized minimal residual method (GMRES) with no preconditioner. Efforts are underway to determine the most efficient preconditioner for this system. We have also implemented an analytical Jacobian for the vertical solve, which appears to be the most computationally efficient option.
- (4) Reference solutions employ consistent 4th order vertical and horizontal discretizations at a resolution at least twice as fine as experiments
- (5) The total number of vertical levels in each test is kept constant. Only the vertical order of accuracy is changed and consequently the distribution of grid spacing according to the locations of element nodes.

For these tests, we investigate the effect of a relatively high-order $n_{vp} = 10$ vertical coordinate on flow results at resolutions coarser than the reference solutions. Our hypothesis is that flow structures and measures of interest will be better approximated using the high-order discretization. We consider the properties of our arbitrary order methods in the context of meshes with

mixed grid resolutions such as static and adaptive variable resolution experiments. A primary benefit of using the higher order SNFEM is improved accuracy even with a coarser vertical grid.

Reference results are computed with a consistent spatial (horizontal and vertical) discretization or order “O4”. Experiments done at coarser resolutions with varying vertical order of accuracy are titled “VO#”.

2.4.1 Steady-state geostrophically balanced flow in a channel

The first test represents steady-state geostrophically balanced flow in a channel and is based on a new test case defined by Ullrich, Reed, and Jablonowski (2015). The domain is a channel of dimensions $L_x \times L_y \times L_z$ with periodic boundaries in the x direction and no-flux conditions at all other interfaces. In this case we choose $L_x = 30000$ km, $L_y = 6000$ km and $L_z = 30$ km. The shorter zonal width compared with that of Ullrich, Reed, and Jablonowski (2015) was chosen for reasons of computational efficiency and did not affect the final solution. The initial flow is comprised of a zonally-symmetric mid-latitude jet, defined so that the wind is zero at the surface and along the y -boundary. Hyperviscosity is applied in the horizontal and vertical at 4th order as well as a Rayleigh layer at the top and longitudinal boundaries. The Rayleigh layers are used to prevent the accumulation of standing wave reflections in the flow. This formulation can either be on an f -plane or β -plane, which have Coriolis parameters

$$f = f_0, \quad \text{and} \quad \beta = f_0 + \beta_0(y - y_0), \quad (2.62)$$

respectively, where $f_0 = 2\Omega \sin \varphi_0$ and $\beta_0 = 2a^{-1}\Omega \cos \varphi_0$ at latitude $\varphi_0 = 45^\circ\text{N}$. Here, the radius of the Earth is $a = 6371.229 \times 10^3$ m, its angular velocity is $\Omega = 7.292 \times 10^{-5} \text{ s}^{-1}$ and $y_0 = L_y/2$ is the center point of the domain in the y -direction.

The simulation is performed for the original β -plane configuration outlined in Ullrich, Reed, and Jablonowski (2015) where the jet is perturbed directly by a “bump” in the zonal wind that is

Chapter 2. The Staggered Nodal Finite-Element Method

vertically uniform where $u_p = 1.0 \text{ m s}^{-1}$ centered at $x_c = 2000 \text{ km}$ and $y_c = 2500 \text{ km}$.

$$u'(x, y) = u_p \exp \left[- \left(\frac{(x - x_c)^2 + (y - y_c)^2}{L_p^2} \right) \right] \quad (2.63)$$

The grid spacing for the reference solution is $\Delta x = 50 \text{ km}$, $\Delta y = 50 \text{ km}$, $\Delta z = 0.75 \text{ km}$ and $\Delta t = 30 \text{ s}$. Experiments are conducted at vertical order 2, 4 and 10 at a resolution of $\Delta x = 200 \text{ km}$, $\Delta y = 200 \text{ km}$, $\Delta z = 1.5 \text{ km}$ and $\Delta t = 240 \text{ s}$. The 4th order scalar and vector (vorticity and divergence separately) diffusion coefficients are given by

$$\nu_{\text{scalar}} = 1.0 \times 10^{14} \left(\frac{\Delta x}{L_{\text{ref}}} \right)^{3.2} \text{ m}^4 \text{ s}^{-1}, \quad (2.64)$$

$$\nu_{\text{vorticity}} = 1.0 \times 10^{14} \left(\frac{\Delta x}{L_{\text{ref}}} \right)^{3.2} \text{ m}^4 \text{ s}^{-1}, \quad (2.65)$$

$$\nu_{\text{divergence}} = 1.0 \times 10^{14} \left(\frac{\Delta x}{L_{\text{ref}}} \right)^{3.2} \text{ m}^4 \text{ s}^{-1}. \quad (2.66)$$

where Δx is the element length in the x direction and $L_{\text{ref}} = 11.0 \times 10^5 \text{ m}$ is the reference length used for this test case. For this test, vertical flow-dependent viscosity is disabled since it did not have a clear impact on the solution.

The baroclinic instability is a primary mechanism for the development of mid-latitude storm systems and so it is important that an atmospheric modeling platform reproduce these phenomena accurately. We present a reference solution of the baroclinic wave shown in fig. 2.3 that is approaching the transition into the non-hydrostatic regime. We are interested in estimates of vertical motion where the reference solution shows maxima on the order of 2 cm s^{-1} . Regions of strong vertical motion correspond to strong horizontal gradients in the vorticity and temperature fields and we expect that non-hydrostatic effects will be locally significant.

The reference solution for temperature and vorticity at 500m elevation shown here can be compared at day 10 with the original results from Ullrich, Reed, and Jablonowski (2015) produced with MCore Ullrich and Jablonowski (2012) to verify that Tempest is computing a consistent solution.

Chapter 2. The Staggered Nodal Finite-Element Method

In particular we expect that vertical motion will be under-predicted in coarser models at a given order of accuracy.

The vorticity field at coarse resolution (fig. 2.4) is largely unaffected by changes in vertical order. However, the vertical velocity (fig. 2.5), and by association the horizontal divergence (not shown), shows a substantial increase in magnitude as order increases. This increase aligns the vertical velocity more closely with the reference solution magnitude (greater than 1 cm s^{-1}) using the 10th order vertical coordinate as shown in fig. 2.5. We conclude that although the higher order vertical coordinate does not substantially impact the horizontal character of the solution, it does better capture the magnitude of vertical velocity, particularly in frontal regions. We note that the coarse resolution chosen here is nearly double that of current operational climate modeling systems and well within the hydrostatic regime.

Chapter 2. The Staggered Nodal Finite-Element Method

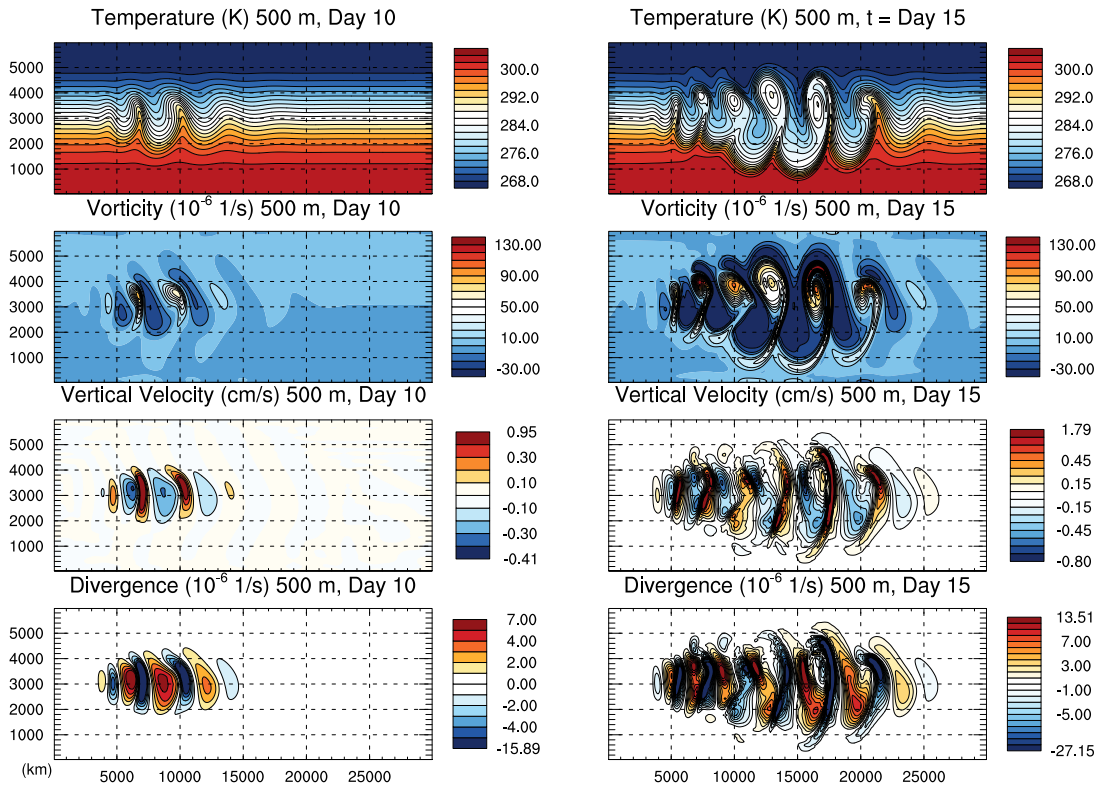


FIGURE 2.3: Baroclinic wave in a 3D Cartesian channel at the reference resolution $\Delta x = 100$ km, $\Delta y = 100$ km, $\Delta z = 1$ km at vertical 4th order accuracy (VO4). From top to bottom, temperature, vorticity, vertical velocity, and divergence are shown at day 10 (left) and 15 (right) and at an elevation of 500 m. Contour intervals: Temperature 2K, Vorticity $1.0 \times 10^{-5} \text{s}^{-1}$, Divergence $5.0 \times 10^{-6} \text{s}^{-1}$, and vertical velocity $2.0 \times 10^{-3} \text{m s}^{-1}$.

Chapter 2. The Staggered Nodal Finite-Element Method

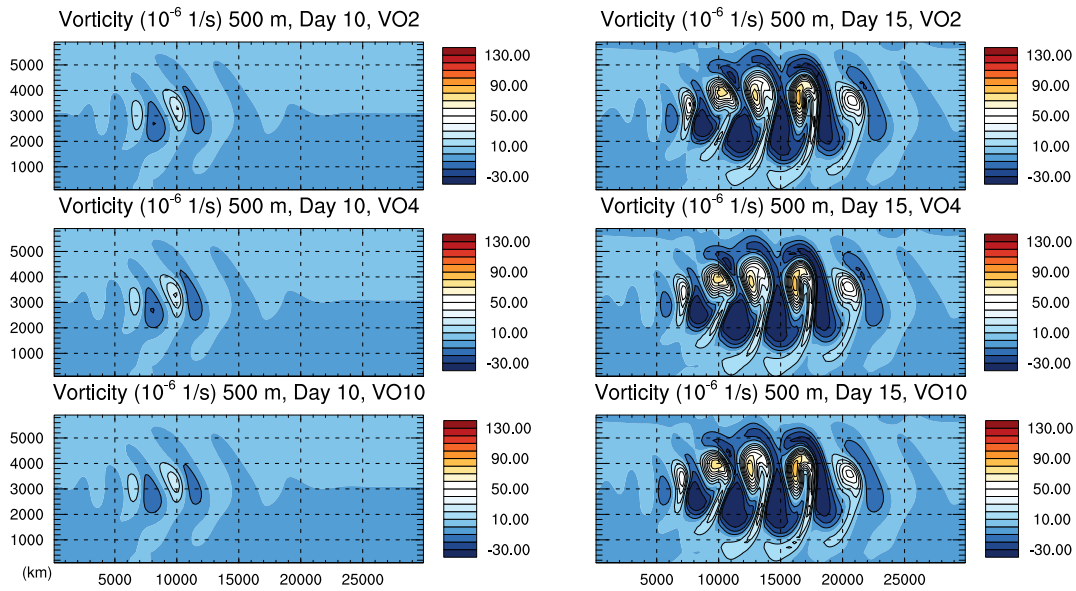


FIGURE 2.4: Baroclinic wave in a Cartesian channel at vertical orders 2, 4 and 10. Vorticity at 500 meters on days 10 and 15 at the resolution $\Delta x = 200$ km, $\Delta y = 200$ km, $\Delta z = 1.5$ km. Contour interval: $1.0 \times 10^{-5} \text{s}^{-1}$

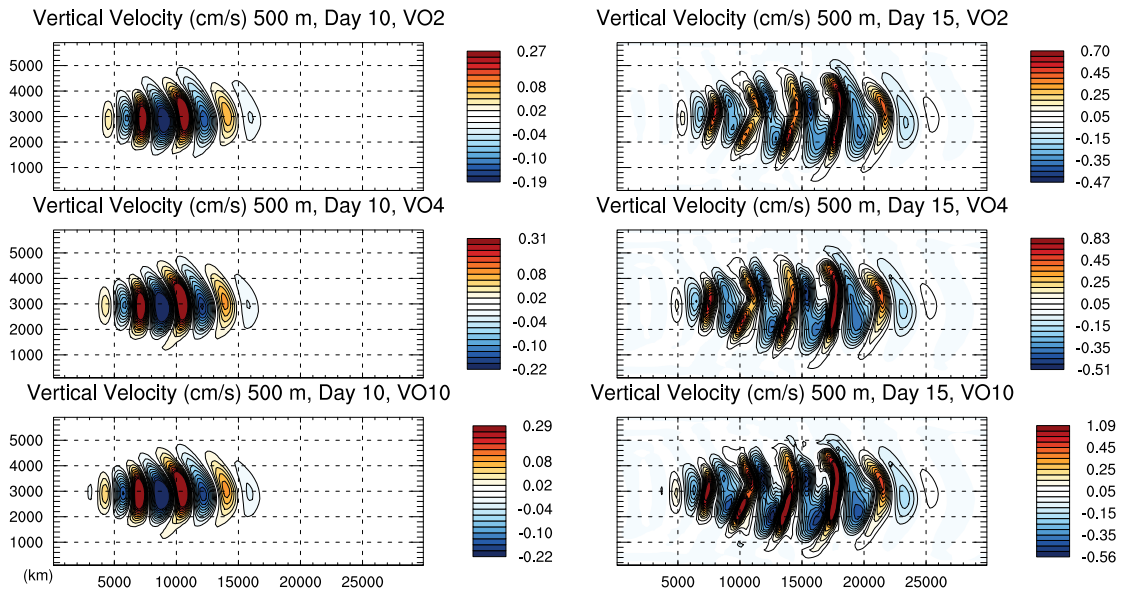


FIGURE 2.5: Baroclinic wave in a Cartesian channel at vertical orders 2, 4 and 10. Vertical Velocity at 500m on days 10 and 15 at the resolution $\Delta x = 200$ km, $\Delta y = 200$ km, $\Delta z = 1.5$ km. Contour interval: $2.0 \times 10^{-3} \text{m s}^{-1}$

2.4.2 Schär mountain

Atmospheric flows are strongly influenced by the lower boundary, where topographically-induced waves transport momentum and energy vertically. Schär et al. (2002) describes a uniform zonal flow field over orography that leads to the generation of a stationary mountain response, consisting of a linear combination of hydrostatic and non-hydrostatic waves. The atmosphere is initially under uniform stratification with constant Brunt-Väisälä frequency $\mathcal{N} = 0.01 \text{ s}^{-1}$. The temperature and pressure are $p_0 = 1000 \text{ hPa}$ and $T_0 = 280 \text{ K}$ at $z = 0 \text{ m}$. To trigger the standing waves, an initial uniform mean flow of $\bar{u} = 10 \text{ m s}^{-1}$ is prescribed over the topographic profile given by

$$h_T(x) = h_c \exp \left[- \left(\frac{x}{a_c} \right)^2 \right] \cos^2 \left(\frac{\pi x}{\lambda} \right), \quad (2.67)$$

with parameters $h_c = 250 \text{ m}$, $\lambda = 4000 \text{ m}$ and $a_c = 5000 \text{ m}$. The simulation domain is $(x, z) \in [-30, 30] \times [0, 25] \text{ km}$ with a no-flux boundary specified along the bottom surface. Free-flow boundary conditions are prescribed at the top and lateral boundaries with a Rayleigh layer 10 km wide along the lateral boundaries and 10 km deep at the model top. Note that the domain bounds differ from Schär et al. (2002) to minimize the effect of the Rayleigh layers on the flow interior. Also, the Rayleigh layer is applied to progressively and smoothly increase in strength up to the boundaries. The simulation is run to $t = 10 \text{ h}$, when the solution has reached a quasi-steady state. For these simulations, no explicit dissipation is applied in either the horizontal or vertical and Coriolis forcing is set to zero throughout.

To validate that Tempest produces the correct mountain wave response, the Schär mountain test was performed until $t = 10 \text{ h}$ with a relatively fine resolution of $\Delta x = 100 \text{ m}$, $\Delta z = 100 \text{ m}$ and $\Delta t = 0.2 \text{ s}$. As shown in fig. 2.6 (left) Tempest accurately reproduces the vertical velocity field at the reference resolution (for comparison with another numerically derived solution, see Giraldo and Restelli (2008)). We also show the analytical solution based on linear mountain theory following Klemp, Skamarock, and Fuhrer (2003); Smith (1979) overlaid in dotted contours. As pointed out by Klemp, Skamarock, and Fuhrer (2003), an inconsistent treatment of the topographic metric

terms in this formulation can lead to the generation of spurious waves which is not observed in this case.

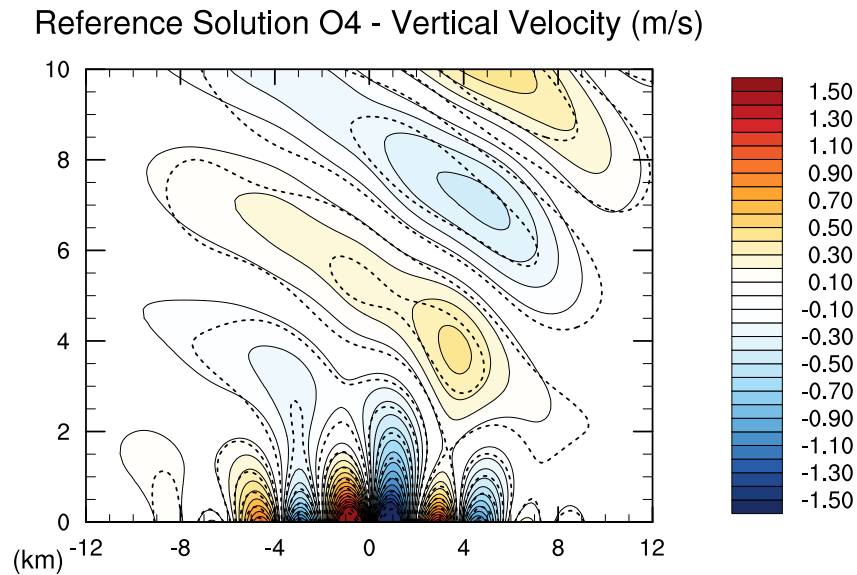


FIGURE 2.6: Schär flow at steady state (10 hours) vertical velocity in (m/s) at VO4. Reference resolution shown compared to the analytical solution (dotted contours) from linear mountain wave theory. $\Delta x = 100$ m and $\Delta z = 100$ m. Contour interval: 0.1 m s^{-1}

As discussed in Thuburn and Woollings (2005) and Thuburn (2006), staggering is necessary to eliminate stationary computational modes that arise in collocated discretizations. To better understand the impact of staggering, fig. 2.7 demonstrates the use of the collocated or unstaggered configuration which shows a highly-oscillatory stationary mode that pollutes the solution relative to the Lorenz configuration at the same resolution. The plots show errors in the vertical velocity near the bottom boundary condition and errors throughout the flow field due to the vertical mode. This artifact is conspicuously absent from both LOR and CPH runs.

Chapter 2. The Staggered Nodal Finite-Element Method

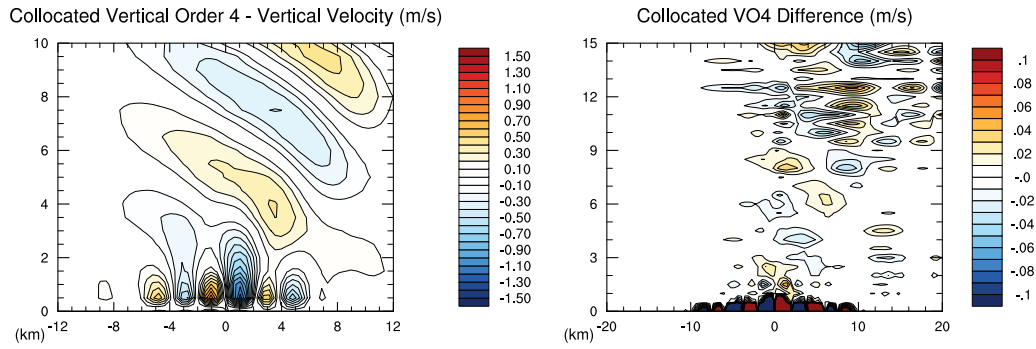


FIGURE 2.7: Schär flow at steady state (10 hours). Collocated method (all variables on column levels) result compared to staggered (Lorenz) solution at the same spatial order and resolution. $\Delta x = 200$ m and $\Delta z = 200$ m. Contour intervals: vertical velocity 0.1 m s^{-1} and vertical velocity difference versus reference 0.0125 m s^{-1}

Chapter 2. The Staggered Nodal Finite-Element Method

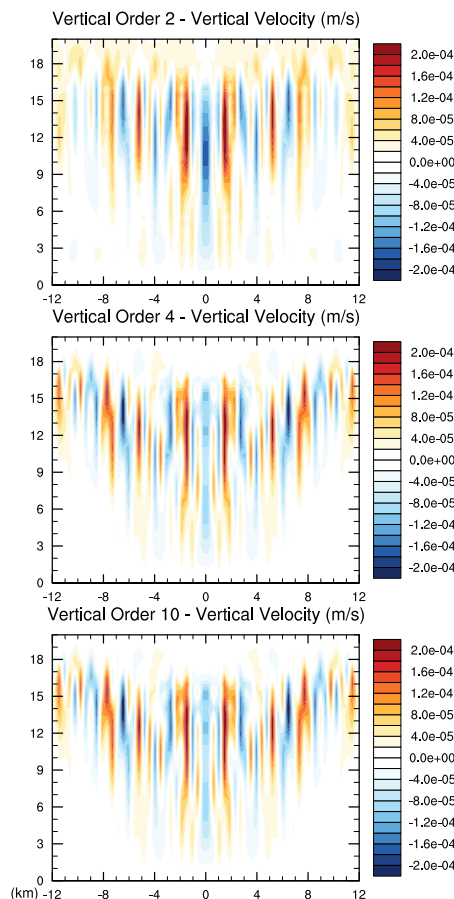


FIGURE 2.8: Still atmosphere experiment over Schär mountain profile at vertical orders 2, 4, and 10 showing errors in vertical velocity. $\Delta x = 500$ m and $\Delta z = 500$ m. Contour interval: $2.0 \times 10^{-5} \text{ m s}^{-1}$.

As discussed in Thuburn and Woollings (2005) and Thuburn (2006), staggering is necessary to eliminate stationary computational modes that arise in collocated discretizations. To better understand the impact of staggering, fig. 2.7 demonstrates the use of the collocated or unstaggered configuration which shows a highly-oscillatory stationary mode that pollutes the solution relative to the Lorenz configuration at the same resolution. The plots show errors in the vertical velocity near the bottom boundary condition and errors throughout the flow field due to the vertical mode. This artifact is conspicuously absent from both LOR and CPH runs.

Because our model makes use of a terrain-following coordinate, it is expected that a hydrostatically balanced rest state is not exactly preserved over topography. Imbalance will arise as a consequence of inexact cancellation of the terrain-following and vertical pressure gradient terms in the discrete equations. Experiments carried out with zero background flow in the presence of topographic features shown in fig. 2.8 indicate that errors in vertical velocity are dominated by the horizontal discretization. We note that improvements with vertical order of accuracy are apparent when going from 2nd order to 4th order, but differences are small at higher orders of accuracy. These errors can be removed completely with a vertical reference state (Giraldo and Restelli, 2008), but such a state is difficult to utilize for global simulations and so may not be desirable in practice.

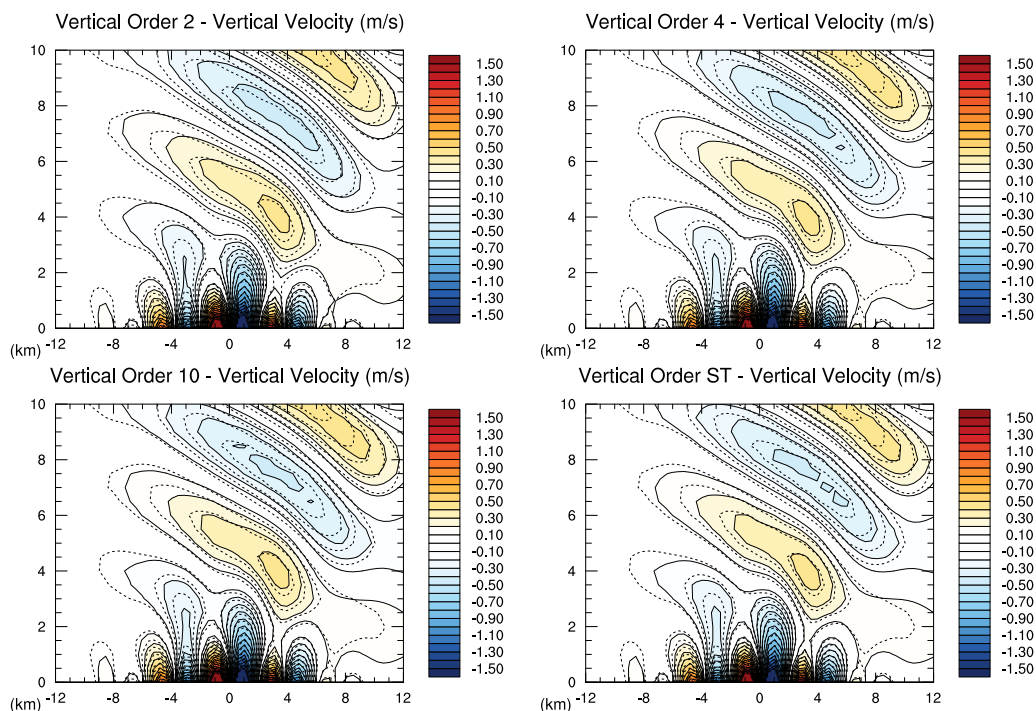


FIGURE 2.9: Schär flow at steady state (10 hours) vertical velocity in (m/s) at various vertical orders of accuracy (2, 4, 10, and ST) where “ST” stands for single column element spectral transform ($n_{ve} = 1$) with Lorenz (LOR) vertical staggering. Colored contours from Tempest compared to dotted contours for the analytical solution. $\Delta x = 500$ m and $\Delta z = 500$ m. Contour interval: 0.1 m s^{-1}

Chapter 2. The Staggered Nodal Finite-Element Method

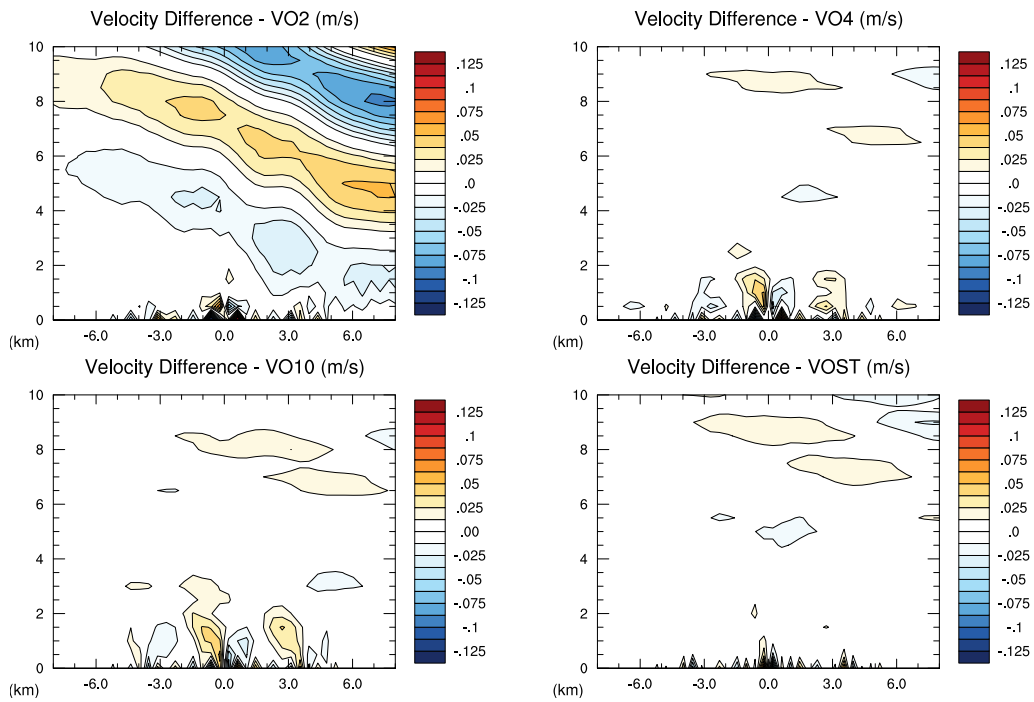


FIGURE 2.10: Schär flow steady state (10 hours). Vertical velocity difference with respect to the reference solution (fig. 2.6, left). Results are interpolated to a regular z coordinate with $\Delta z = 500$ m in experiments and reference solution for differencing. Computations performed at $\Delta x = 500$ m and $\Delta z = 500$ m. Contour interval: 0.0125 m s^{-1}

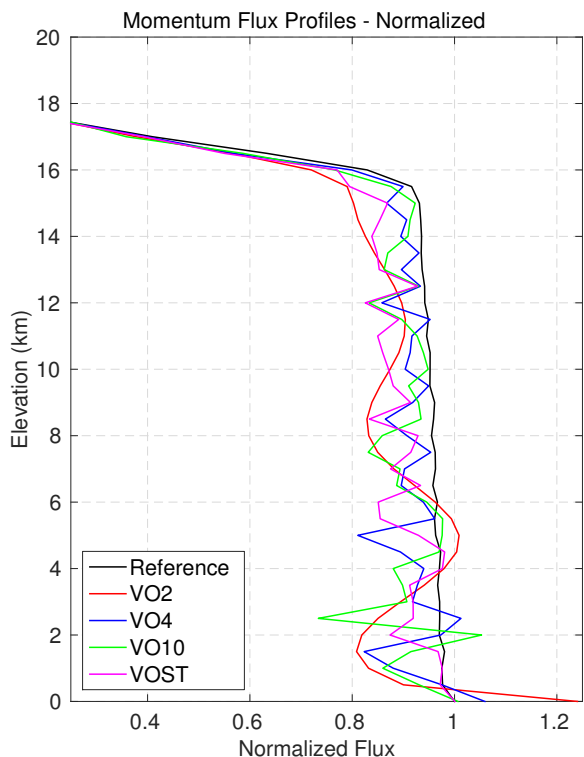


FIGURE 2.11: Schär mountain vertical profile of momentum flux for all experiments. The flux profiles are computed by $\int_{-X}^X \{[\bar{\rho} + \rho'] [\bar{u} + u'] w'\} dx$ at $t = 10$ hours where overbars indicate initial condition values and primes are departures thereof. Results are interpolated to a regular z coordinate with $\Delta z = 500$ m in experiments and reference solution to compute the integral flux. Results are normalized to the value at the surface in the reference solution.

Experiments are conducted at vertical order 2, 4, 10, and 40 (in the limit where the polynomial order is equal to the total number of levels, denoted ST) at a relatively coarse resolution of $\Delta x = 500$ m, $\Delta z = 500$ m and $\Delta t = 0.4$ s. Results are depicted in fig. 2.9 and the difference against the reference solution in fig. 2.10. The 2nd order results show substantial disagreement with the reference solution that is enhanced at altitude. This result appears to be associated with an overestimation of the vertical wavelength of the mountain response that arises from the lower order discretization. At 4th order the upper atmosphere does not show substantial errors, and most differences are instead constrained to the near-surface. These near-surface errors generally show consistent improvement as the vertical order-of-accuracy is increased. The discrepancy that

appears at the highest peak of the Schär mountain ($x = 0$) is associated with slight differences in resolving the topography at coarser horizontal resolution than the reference solution.

We further compare the resulting profiles of momentum flux for all experiments in the Lorenz configuration (Fig.2.11). We observe that the flux profile for the 2^{nd} -order method has the greatest error, as expected from dispersion errors typical of low-order centered schemes (particularly in the upper atmosphere and near the surface). The higher-order methods show improvements in the structure and magnitude of the profiles (especially at the near-surface, when compared to the reference profile in black), but again appear to be influenced by the lower-order horizontal discretization. Furthermore, the results are strongly influenced by the Rayleigh layer showing a pronounced deviation in the flux profiles throughout the domain. The Rayleigh layer approximation to a free-flow boundary condition clearly introduces deficiencies that are exacerbated in the flux profiles.

2.4.3 Straka density current

The density current test case of Straka et al. (1993) considers a cold bubble that sinks and spreads across the bottom boundary, driving the development of Kelvin-Helmholtz rotors. The original experiments by Straka et al. (1993) sought a converged solution through the use of 2^{nd} order uniform diffusion applied to all prognostic variables. A value of $\nu = 75 \text{ m}^2 \text{ s}^{-1}$ was chosen so that a horizontal resolution of $\Delta x = 25 \text{ m}$ was sufficient for convergence. No-flux conditions are applied on all boundaries and Coriolis forcing set to zero.

The initial state consists of a hydrostatically balanced state with a uniform potential temperature of $\theta = 300 \text{ K}$. A standard pressure of $p_0 = 1000 \text{ hPa}$ is assumed. The cold bubble perturbation is applied to the θ field and is given by

$$\theta' = \begin{cases} 0 & \text{if } r > 1.0, \\ -\frac{\theta_c}{2} [1 + \cos(\pi r)] & \text{if } r \leq 1.0, \end{cases} \quad (2.68)$$

Chapter 2. The Staggered Nodal Finite-Element Method

where $\theta_c = -15$ K and

$$r = \sqrt{\left(\frac{x - x_c}{x_r}\right)^2 + \left(\frac{z - z_c}{z_r}\right)^2}. \quad (2.69)$$

The domain is an enclosed box $(x, z) \in [-25600, 25600] \times [0, 6400]$ m with $t \in [0, 900]$ s. The cold bubble is initially located at $(x_c, z_c) = (0, 3000)$ m with radius $(x_r, z_r) = (4000, 2000)$ m.

The 4th order horizontal hyperdiffusion coefficients for all fields are given by

$$\nu_{\text{scalar}} = 5.0 \times 10^{12} \left(\frac{\Delta x}{L_{\text{ref}}}\right)^{3.2} \text{ m}^4 \text{ s}^{-1}, \quad (2.70)$$

$$\nu_{\text{vorticity}} = 2.0 \times 10^{14} \left(\frac{\Delta x}{L_{\text{ref}}}\right)^{3.2} \text{ m}^4 \text{ s}^{-1}, \quad (2.71)$$

$$\nu_{\text{divergence}} = 2.0 \times 10^{14} \left(\frac{\Delta x}{L_{\text{ref}}}\right)^{3.2} \text{ m}^4 \text{ s}^{-1}, \quad (2.72)$$

where Δx is the element length in the x direction and $L_{\text{ref}} = 51200.0$ m is the reference length used for this test case.

For the experiments with vertical flow-dependent hyperviscosity, the viscous coefficients are given by (2.47). The uniform Laplacian diffusion requires further stabilization via the addition of 4th order scalar hyperviscosity in the horizontal and 4th order vertical flow-dependent diffusion on all variables. This added diffusivity is necessary to control a horizontal stationary mode in the scalar fields and fast moving vertical modes that are a consequence of sound waves accumulating energy at the grid scale. However, the highly scale-selective nature of the high degree operators does not significantly affect the structure of the reference solution as shown in fig. 2.12.

The grid spacing for the reference solution is $\Delta x = 25$ m and $\Delta z = 25$ m with $\Delta t = 0.01$ s. Experiments are further conducted at vertical order 2 and 10 at a resolution of $\Delta x = 200$ m and $\Delta z = 200$ m with $\Delta t = 0.01$ s.

Chapter 2. The Staggered Nodal Finite-Element Method

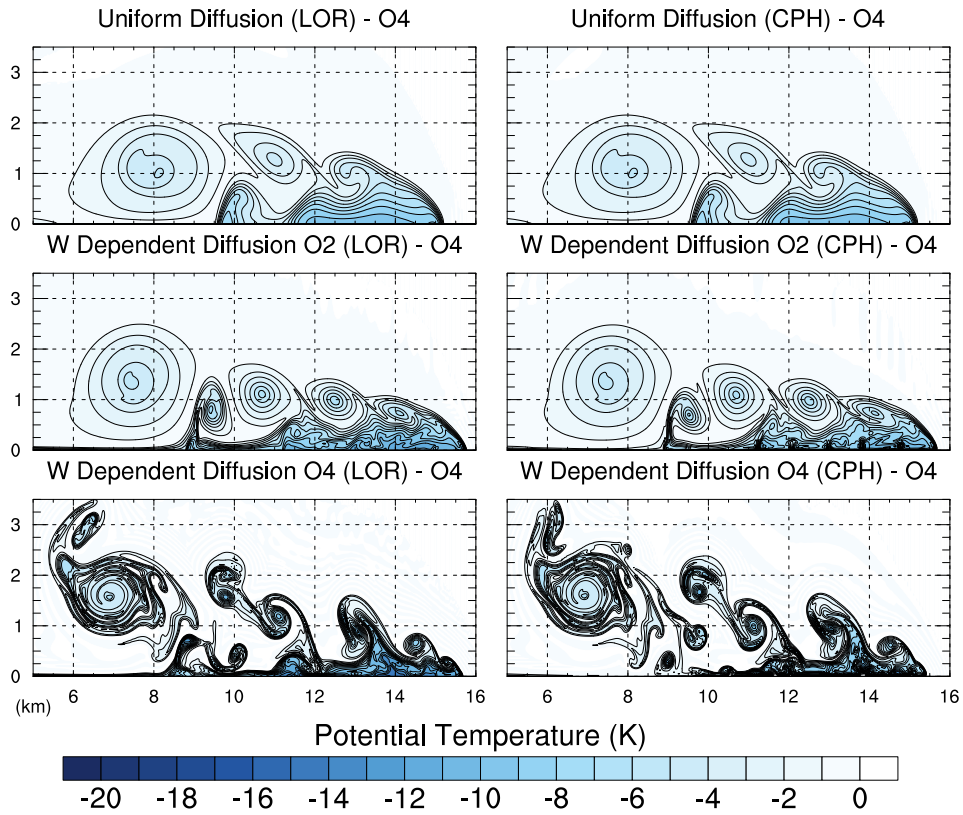


FIGURE 2.12: Straka Density Current test reference solutions at vertical order 4 in two staggering configurations LOR and CPH. Converged resolution of $\Delta x = 25$ m and $\Delta z = 25$ m shown. Vertical flow dependent diffusion in of order 2 and 4 (rows 2 and 3) is compared with the reference solution where an explicit 2^{nd} order diffusion with $\nu_0 = 75 \text{ m}^2\text{s}^{-1}$ is used (top row). Contour interval: 1.0K

Chapter 2. The Staggered Nodal Finite-Element Method

Method-Stagger	Vertical Order @ Resolution	Diffusion Method	Wave Front (km)
SNFEM-LOR	2 @ $\Delta x = 190$ m	Reference Damping	14.21
SNFEM-LOR	2 @ $\Delta x = 190$ m	Up-wind Order 2	14.59
SNFEM-LOR	2 @ $\Delta x = 190$ m	Up-wind Order 4	15.68
SNFEM-LOR	4 @ $\Delta x = 190$ m	Reference Damping	14.18
SNFEM-LOR	4 @ $\Delta x = 190$ m	Up-wind Order 2	14.58
SNFEM-LOR	4 @ $\Delta x = 190$ m	Up-wind Order 4	15.47
SNFEM-LOR	10 @ $\Delta x = 190$ m	Reference Damping	14.22
SNFEM-LOR	10 @ $\Delta x = 190$ m	Up-wind Order 2	14.61
SNFEM-LOR	10 @ $\Delta x = 190$ m	Up-wind Order 4	15.33
FD-Colocated	2 REFC @ $\Delta x = 25$ m	Explicit $\nu_0 = 75 \text{ m}^2\text{s}^{-1}$	15.53
SNFEM-LOR	4 (REF) @ $\Delta x = 25$ m	Reference Damping	15.20
SNFEM-LOR	4 (REF) @ $\Delta x = 25$ m	Up-wind Order 2	15.77
SNFEM-LOR	4 (REF) @ $\Delta x = 25$ m	Up-wind Order 4	15.68

TABLE 2.2: Cold wave front position ($\theta' = -1.0$ K) for all orders of accuracy and diffusion methods. Reference damping is uniform 2^{nd} order diffusion on all prognostic variables such that $\nu = 75 \text{ m}^2\text{s}^{-1}$ combined with horizontal hyperdiffusion on scalars and vertical 4^{th} order up-wind diffusion. The reference solution wave front position (finite difference method at 25 meter resolution) by Straka et al. (1993) is shown in bold (REFC) compared to the equivalent result from Tempest.

Chapter 2. The Staggered Nodal Finite-Element Method

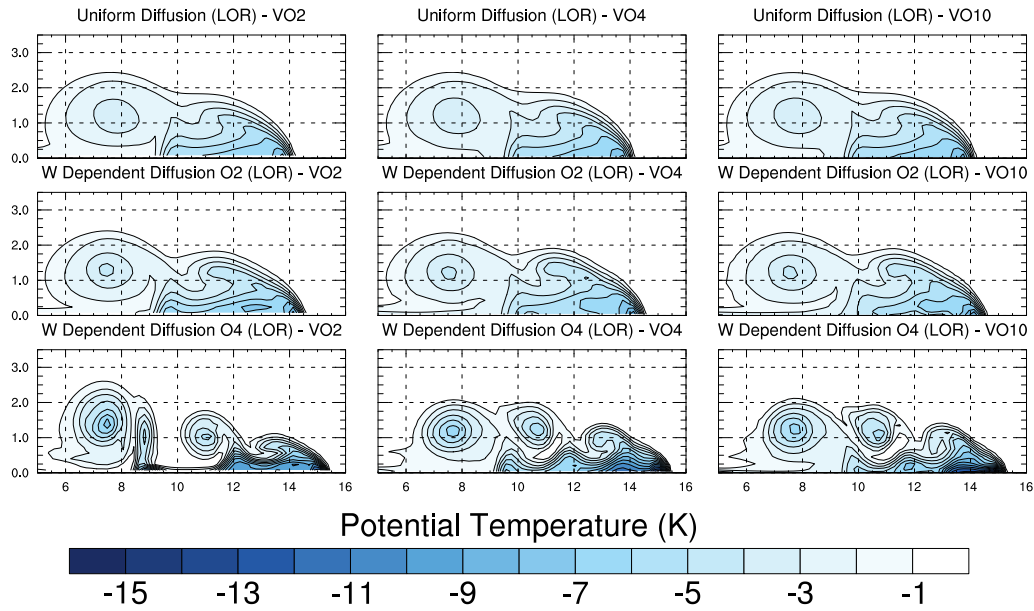


FIGURE 2.13: Straka Density Current test at vertical order 2, 4 and 10. Coarse, evaluation resolution of $\Delta x = 190$ m and $\Delta z = 160$ m shown. Vertical flow dependent diffusion of order 2 and 4 (rows 2 and 3) is compared with the reference solution where an explicit 2^{nd} order diffusion with $\nu_0 = 75 \text{ m}^2\text{s}^{-1}$ is used (top row). Results for Lorenz (LOR) staggering shown. Contour interval: 1.0K

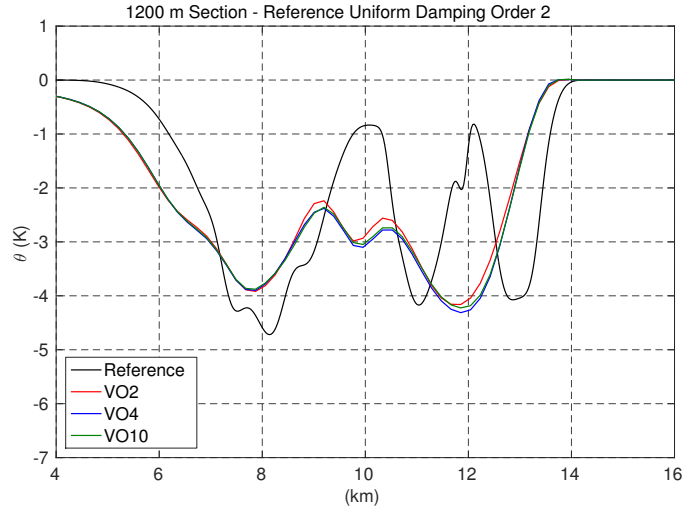


FIGURE 2.14: Straka Density Current test at vertical order 2, 4 and 10. Coarse, evaluation resolution of $\Delta x = 190$ m and $\Delta z = 160$ m with explicit 2^{nd} order diffusion with $\nu_0 = 75 \text{ m}^2\text{s}^{-1}$ compared at 1200 m with the reference solution ($\Delta x = 25$ m and $\Delta z = 25$ m). Results for Lorenz (LOR) staggering shown.

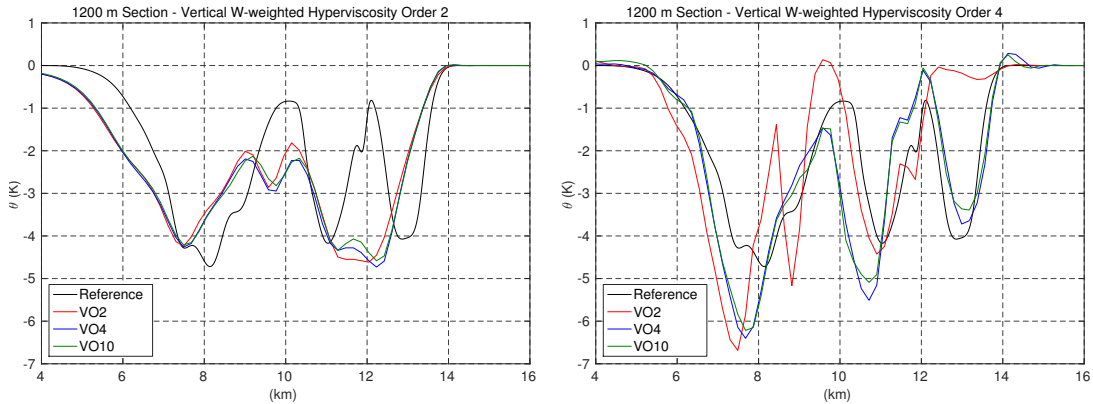


FIGURE 2.15: Straka Density Current test at vertical order 2, 4 and 10. Coarse, evaluation resolution of $\Delta x = 190$ m and $\Delta z = 160$ m shown. Vertical flow dependent diffusion of derivative order 2 and 4 compared at 1200 m with the reference solution ($\Delta x = 25$ m and $\Delta z = 25$ m). Results for Lorenz (LOR) staggering shown.

For the density current, we emphasize results from the Lorenz (LOR) staggering. Under Charney-Phillips (CPH) staggering, the vertical advection term for potential temperature (see

Table 2.1) on the bottom-most and top-most interfaces is exactly zero within our formulation. Consequently, within our formulation there is no mechanism to transport θ vertically from these interfaces leading to the development of a discontinuity in θ along the lower boundary. These gradients then enhance vertical heat fluxes above the surface, slowing the propagating cold pool as momentum is transported vertically. This inconsistency is counteracted by the application of uniform diffusion, which provides a mechanism by which θ can be exchanged with the bottom interface. However, flow-dependent vertical diffusion, which is weighted by $|u^\xi|$, does not permit exchange with the interface and so leads to inconsistency between the LOR and CPH staggerings. In fig. 2.12, the CPH staggering with flow-dependent diffusion leads to a relatively slow density current that is more convective near the boundary. Nonetheless, a better choice of flow-dependent coefficient could be made to mitigate this issue. Note that this issue with CPH can be counteracted by rewriting the vertical advection term as

$$u^\xi \frac{\partial \theta}{\partial \xi} = \frac{\partial}{\partial \xi}(u^\xi \theta) - \theta \frac{\partial u^\xi}{\partial \xi}, \quad (2.73)$$

although this form tends to be more unstable in practice

We often desire diffusion to be as weak as possible while still preserving the stability of the underlying method. However, as can be seen here, the structure of the density current is also strongly dependent on the dissipation mechanisms employed in the simulation. Here we present the reference solution equivalent to Straka et al. (1993) at the converged resolution. We also compare solutions with different diffusion mechanisms in fig. 2.12 with corresponding cross sections in fig. 2.14. The 1200 m cross sections indicate that experimental coarse resolutions are not converged in the case of reference uniform damping. In Table 2.2 it is apparent the reference solutions are sensitive to diffusion and differ significantly in structure, but the wave front positions compare with good precision to the solution given by Straka et al. (1993). This would indicate that momentum fluxes are comparable, but close inspection of the eddy structure suggests significant differences exist throughout, as noted above, and with the appearance of detached eddies when

the high-order flow-dependent viscosity is used exclusively.

From Table 2.2 it is apparent our coarse-resolution experimental solutions are slow with reference damping and 2nd order flow-dependent viscosity, but are closer to the reference solution with 4th order diffusion. Both low- and high-order simulations show wave front positions that accurately approximate the reference results. However, the structure of the Kelvin-Helmholtz rotors changes significantly with vertical order-of-accuracy and dissipation method shown in fig. 2.13. The more scale-selective 4th order flow-dependent viscosity shows greater detail in the structure of the rotors. In general, it is not recommended to use hyperdiffusion with a higher order than the dynamical discretization (bottom left) since more derivatives would be required than the polynomial space allows.

The use of flow-dependent hyperviscosity in 2nd and 4th derivative order changes the structure of coarse experiments tending toward a 3-rotor flow field shown in the reference solution as shown in fig. 2.15. Curiously, the 10th order vertical discretization with 4th order flow-dependent viscosity produces a flow that more closely approximates the reference solutions at a resolution that would otherwise be considered too poor for the dynamical features considered. However, the authors have not found a dynamical reason for correlation involving high-order vertical discretization coupled with high-order dissipation schemes and the reference solution with uniform damping.

Moreover, fig. 2.15 indicates that magnitudes are significantly different for high-order dissipation cases. Wave front position at the -1.0°C contour further given in 2.2 confirm that momentum fluxes are also captured more accurately as these are associated to the propagation speed of the wave front.

2.4.4 Rising thermal bubble

Thermal bubble experiments have become a standard in the development of non-hydrostatic mesoscale modeling systems. At very fine resolutions ($< 10\text{ m}$) we test the ability to reproduce the simplest form of convection. This is a precursor to simulations of real atmospheric phenomena such as thunderstorms and other convective systems. A positive, symmetric perturbation to the

Chapter 2. The Staggered Nodal Finite-Element Method

potential temperature (buoyancy imbalance) causes a vertical acceleration that moves the bubble upward. Subsequently, shearing and compensating subsidence leads to two primary symmetrical eddies that further break down as the simulation progresses. We are interested in the evolution of the flow in terms of structure and conservative properties on θ .

We present two flow scenarios: a) the bubble rises and is allowed to interact with the top and lateral boundaries and b) the so-called Robert smooth bubble experiment (as outlined in Giraldo and Restelli (2008)) that are a variation of the experiments of Robert (1993). In the former, the bubble will meet the boundaries and develop shear instabilities and in the Robert bubble, shear instabilities develop in the interior of the flow. For these experiments, 4th order viscosity is applied in the horizontal and vertical to the potential temperature and horizontal velocity fields. Furthermore, at finer resolutions we observe more fine-scale features of the thermal bubble, including tighter winding of the trailing edges at later times and sharper spatial gradients. Nonetheless, our comparisons for this test case are purely qualitative but remain consistent with previous results.

The background consists of a constant potential temperature field $\bar{\theta} = 300$ K, with a small perturbation of the form

$$\theta' = \begin{cases} 0 & \text{for } r > r_c, \\ \frac{\theta_c}{2} \left[1 + \cos\left(\frac{\pi r}{r_c}\right) \right] & \text{for } r \leq r_c, \end{cases} \quad (2.74)$$

where

$$r = \sqrt{(x - x_c)^2 + (z - z_c)^2}. \quad (2.75)$$

Here we choose the amplitude and radius of the perturbation to be $\theta_c = 0.5$ K and $r_c = 250$ m, respectively. The domain consists of a rectangular region $(x, z) \in [0, 1000] \times [0, 1000]$ m for the thermal bubble and $(x, z) \in [0, 1000] \times [0, 1500]$ m for the Robert bubble with $t \in [0, 1200]$ s. The center-point of the bubble is located at $x_c = 500$ m and $z_c = 350$ m for the thermal bubble and $z_c = 260$ m for the Robert bubble. The boundary conditions are no-flux over all boundaries. No Rayleigh layer is used, and Coriolis forces are set to zero.

Chapter 2. The Staggered Nodal Finite-Element Method

The reference grid spacing is $\Delta x = 5$ m and $\Delta z = 5$ m respectively with $\Delta t = 0.005$ s. This is considered the reference resolution following Giraldo and Restelli (2008). Experiments are conducted at a relatively coarser resolution of $\Delta x = 10$ m and $\Delta z = 10$ m with $\Delta t = 0.01$ s. The 4th order scalar and vector (vorticity and divergence separately) diffusion coefficients in are given by

$$\nu_{\text{scalar}} = 1.0 \times 10^6 \text{ m}^4\text{s}^{-1}, \quad \nu_{\text{vorticity}} = 1.0 \times 10^6 \text{ m}^4\text{s}^{-1}, \quad \nu_{\text{divergence}} = 1.0 \times 10^6 \text{ m}^4\text{s}^{-1}. \quad (2.76)$$

The 4th order scalar and vector (vorticity and divergence separately) diffusion coefficients in are given by

$$\nu_{\text{scalar}} = 1.0 \times 10^6 \left(\frac{\Delta x}{L_{\text{ref}}} \right)^{3.2} \text{ m}^4\text{s}^{-1}, \quad (2.77)$$

$$\nu_{\text{vorticity}} = 1.0 \times 10^6 \left(\frac{\Delta x}{L_{\text{ref}}} \right)^{3.2} \text{ m}^4\text{s}^{-1}, \quad (2.78)$$

$$\nu_{\text{divergence}} = 1.0 \times 10^6 \left(\frac{\Delta x}{L_{\text{ref}}} \right)^{3.2} \text{ m}^4\text{s}^{-1}. \quad (2.79)$$

where Δx is the element length in the x direction and $L_{\text{ref}} = 1000.0$ m is the reference length used for this test case.

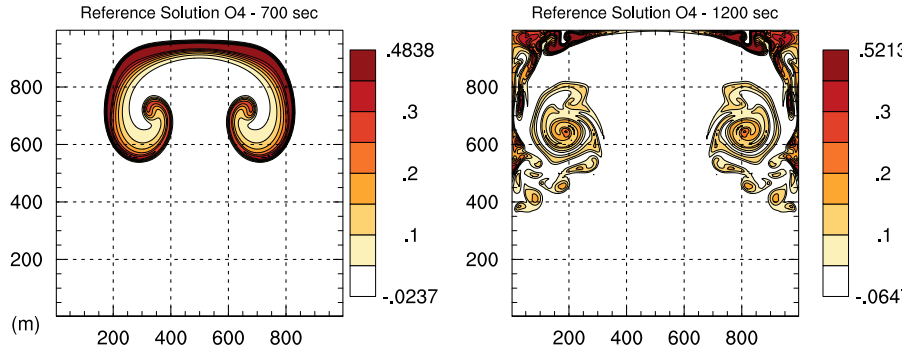


FIGURE 2.16: Rising thermal bubble potential temperature reference solution at vertical order 4. Reference resolution $\Delta x = 5$ m and $\Delta z = 5$ m. Flow at 700 and 1200 seconds. Contour interval: 0.05K

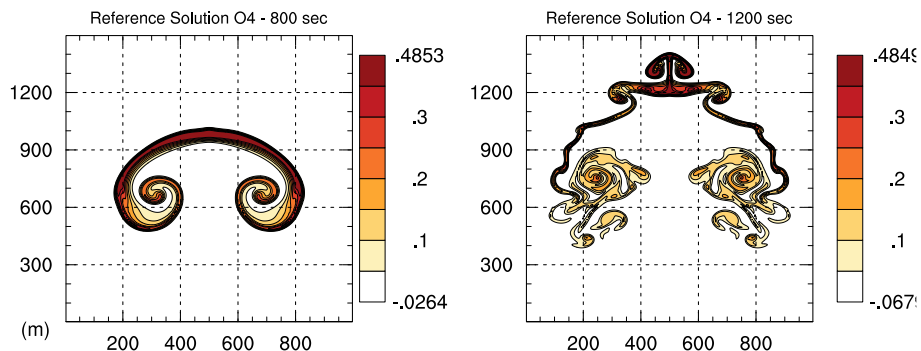


FIGURE 2.17: Rising Robert bubble potential temperature reference solution at vertical order 4. Reference resolution $\Delta x = 5$ m and $\Delta z = 5$ m. Flow at 800 and 1200 seconds. Contour interval: 0.05K

Rising bubble experiments show the non-linear dynamics of dry 2D convection. The classic thermal bubble test shown in fig. 2.16 shows potential temperature being advected conservatively throughout the domain at the reference resolution. These results use a dissipation mechanism that combines 4th order hyperdiffusion of θ for horizontal modes and scale-adaptive 4th order flow-dependent hyperviscosity of θ for vertical modes. In this case, no diffusion is needed in the velocity or density fields to obtain a stable simulation.

The rising thermal bubble experiment is typically carried out and compared at 700 seconds precisely before the convective bubble interacts with the top boundary of the domain. We present this result for comparison with previous results in fig. 2.18. However, it is also important to evaluate the conservative properties of the method and we carry out the simulation to 1200 seconds. Since (2.9) is a strict statement of constant potential temperature following fluid parcels, the results of fig. 2.18 compared to fig. 2.16 demonstrate that our method is stable and approximates conservation of θ closely when a high-order vertical discretization is used.

Chapter 2. The Staggered Nodal Finite-Element Method

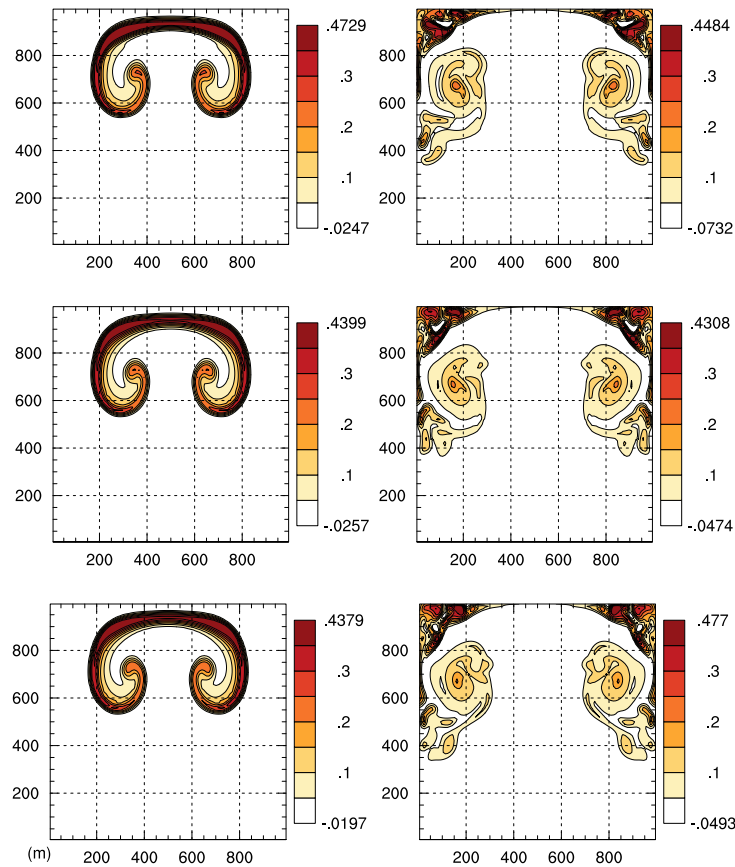


FIGURE 2.18: Rising thermal bubble potential temperature at vertical orders 2, 4 and 10. Convection bubbles at 700 and 1200 seconds. Coarse, resolution $\Delta x = 10$ m and $\Delta z = 10$ m. Extrema in θ shown. Contour interval: 0.05K

The Robert smooth bubble experiment extends the vertical domain allowing for the onset of Kelvin-Helmholtz instabilities in the flow. The solution at the reference resolution is shown in fig. 2.17. The exact time and manner in which the instabilities arise is strongly dependent on the vertical order and dissipation method used in the simulation. In the reference solution, the onset of unstable eddies begins at approximately 900 s with the flow transitioning into vigorous mixing in the region of the primary rotors.

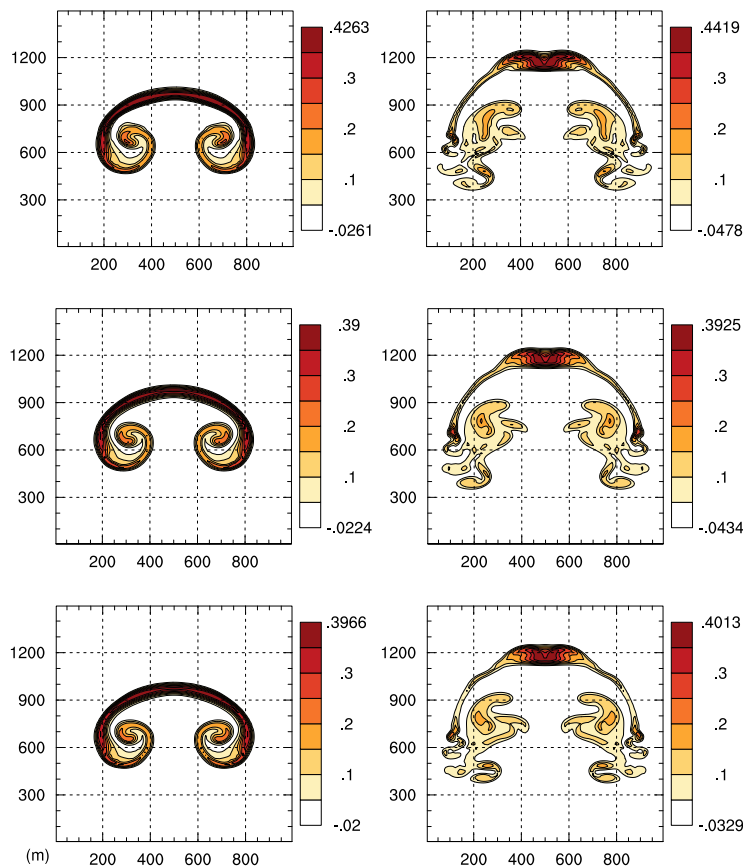


FIGURE 2.19: Rising Robert bubble potential temperature at vertical orders 2, 4 and 10. Convection bubbles at 800 at 1200 seconds. Coarse, evaluation resolution $\Delta x = 10$ m and $\Delta z = 10$ m. Extrema in θ shown. Contour interval: 0.05K

High-order vertical discretizations are typically associated with strong oscillations (Gibbs ringing) that can induce perturbations that can amplify turbulence, particularly if stabilization (such as upwinding or diffusion) is weak. The net effect is that a high-order vertical discretization, given the same horizontal discretization, changes the local mixing characteristics of the flow. This effect is seen clearly in fig. 2.19. The 10th order simulation has a structure that more closely approximates the reference result in fig. 2.17. In the context of studies that seek to represent convective processes, we would expect entrainment fluxes to be improved at a coarser resolution with the higher-order vertical discretizations.

2.4.5 Numerical Characteristics of the Method

We briefly characterize the combined discretization strategy (horizontal spectral element, vertical SNFEM, and Strang IMEX) described in section 2.3.3. We use the rising thermal bubble test (section 2.4.4) to show that, overall, our method converges at 2^{nd} order in space and time consistently across different vertical orders of accuracy as shown in fig. 2.20. Theoretically, the maximal convergence rate for this test is at most 2^{nd} order in space since the θ perturbation is only continuous in its first derivative. Nonetheless, we observe sub- 2^{nd} order convergence for the VO2 scheme applied to this test, driven by a loss of one-order of accuracy from the use of vertical flow-dependent hyperviscosity (see section 2.3.2).

A numerically computed estimate of the CFL condition (maximum Courant number) as a function of grid spacing and element aspect ratio is given in Table 2.3 using the time integration technique outlined in section 2.3.3. These results indicate a maximum Courant number of 1.95 at low order that degrades at higher aspect ratios and with higher vertical order. Moreover, all 2-D tests show a maximum Courant number of 1.95 while the 3-D Baroclinic wave test has a Courant number of 1.45. The theoretical CFL conditions for the spectral element discretization with temporal discretization (56) are 2.12 and 1.49 for 1-D and 2-D scalar advection, respectively. These results indicate that the operator split method as shown in eqs. (2.49)-(2.52) combined with Strang integration allows 90 to 95% of the maximum time step possible using a consistent 4th order space discretization. However, a more comprehensive evaluation of the theory underlying this CFL condition will be pursued in a future work due to changes observed with aspect ratio and vertical order of accuracy.

Maximum Courant Number	Aspect Ratio $\Delta x : \Delta z$		
Vertical Order	1	10	100
2	1.95	1.95	1.95
4	1.95	1.95	1.86
10	1.61	1.14	0.14

TABLE 2.3: Numerically computed estimates of the Courant-Friedrichs-Lewy condition (maximum Courant number) using Thermal Bubble tests over a wide range of horizontal : vertical aspect ratios. The maximum wave speed corresponds to the speed of sound given by $c = \sqrt{\gamma R_d T}$ where $\gamma = 1.4$, $R_d = 286.07$, and $T = 300.5K$.

Computation Time (s)	# Cores		
Vertical Order	1	2	4
2^{nd}	0.117	0.070	0.061
4^{th}	0.163	0.102	0.082
10^{th}	0.248	0.143	0.106

TABLE 2.4: Thermal bubble test ($\Delta x = 20$ m) average processor time taken per time step in seconds. Intel Core i7 4000 series under Linux with 4 computational cores on die (no interconnect hardware present). Results show relative scalability for Tempest using MPI architecture and IMEX partitioning with variable vertical order of accuracy. The implicit equations are solved using the GMRES with no preconditioner.

Furthermore, we show preliminary parallel performance scaling in Table 2.4 on a limited multicore system. These results indicate a cost associated with denser element operations as vertical order of accuracy increases. However, more controlled experiments using a distributed platform will be conducted as our parallel implementation is optimized.

Plots of the normalized change in mass and energy, along with integrated zonal and vertical momentum from the Robert smooth bubble test (section 2.4.4) are given in fig. 2.21. As expected, total mass is conserved to near-machine precision. Total energy is not explicitly conserved by this method, so we observe small oscillations of total energy about its initial value. Note that although

Chapter 2. The Staggered Nodal Finite-Element Method

total energy is not nonincreasing, it does not show exponential growth that would be characteristic of a linear instability, and remains bounded over the duration of the simulation. To ensure this result held for long-term simulations, the rising thermal bubble experiments were carried out to 1 hour, and revealed no sign of instability.

Further investigation of this issue seems to suggest roots in the way the stabilization mechanism interacts with the lateral boundaries, since the purely advective scheme with no stabilization shows nearly flat total energy. Consequently, we hypothesize this result may be associated with the inverse energy cascade from 2d turbulence theory drawing energy from the unresolved scales in a limited manner. Note that the stabilization mechanisms described by this work (horizontal and vertical hyperviscosity), which work directly on the \mathbf{u} and θ fields, do not act to explicitly diffuse energy; the strategy is intended to emphasize flow features. A more aggressive diffusion strategy could be implemented to ensure that energy does not increase at the cost of increased diffusive errors.

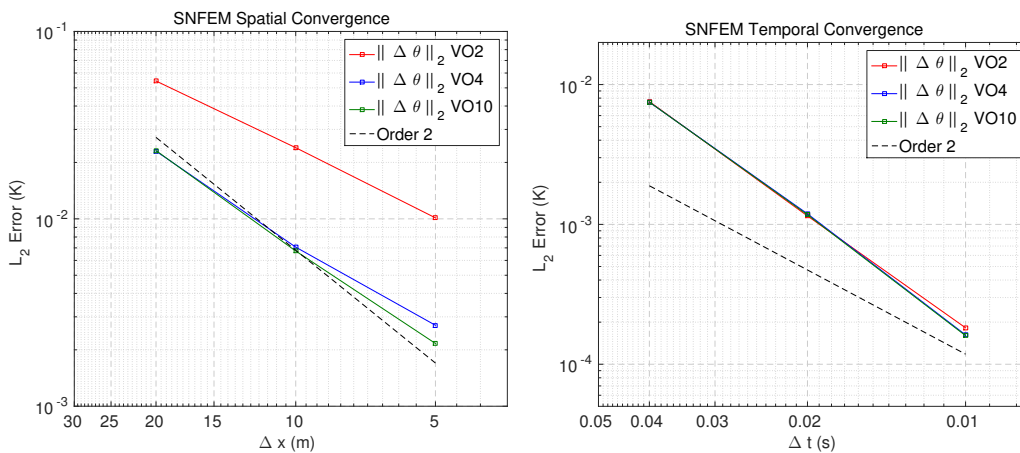


FIGURE 2.20: Spatial (left) and temporal (right) self convergence at various vertical orders of accuracy. Thermal bubble test at 200 s. Spatial resolution for temporal convergence is 10 m with reference $\Delta t = 0.001$ s. Reference spatial resolution is $\Delta x = 2$ m.

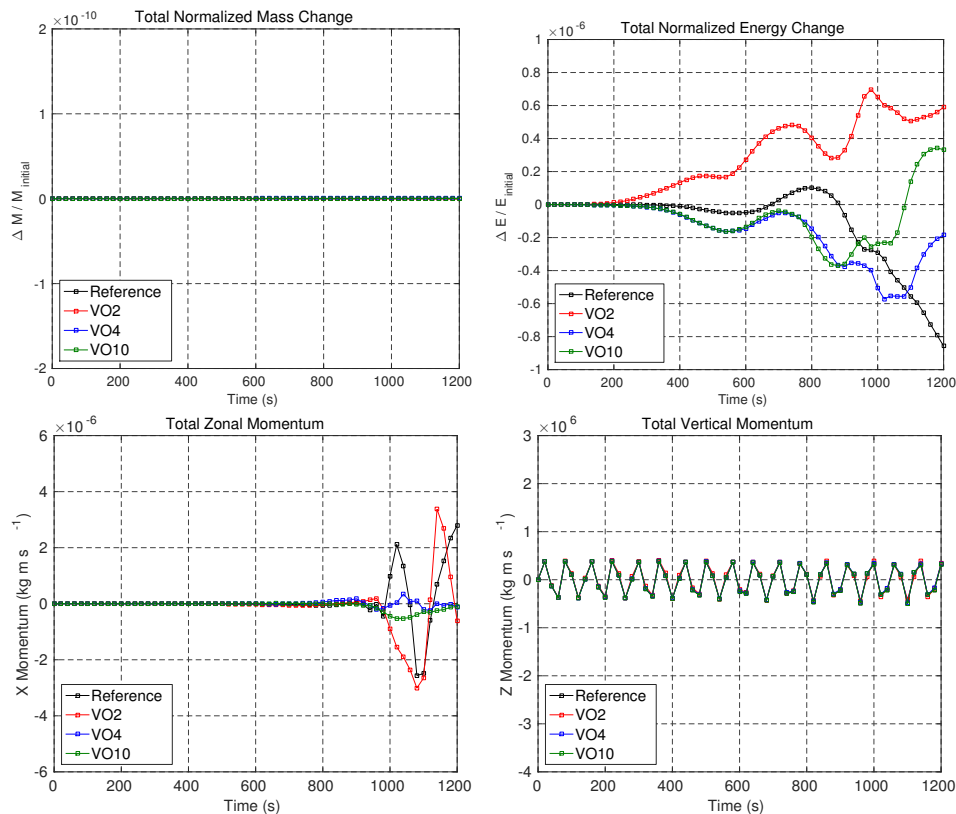


FIGURE 2.21: Observed normalized change in mass and energy (top row), along with zonal and vertical momentum (bottom row) using the Robert Bubble experiment in section 2.4.4. The reference solution corresponds to fig. 2.17 with 5 m resolution. Evaluation experiments use variable vertical order (VO) SNFEM at 10 m resolution corresponding to fig. 2.19. Total normalized mass and energy change are computed as $(Q_t - Q_{initial}) / Q_{initial}$.

For a horizontally symmetric test such as the rising thermal bubble (anti-symmetric in u), one would expect that total zonal momentum is equal to zero over the duration of the simulation. However, we clearly observe deviations from symmetry by the end of the simulation. These violations of symmetry are associated with how the spectral element method is updated in the horizontal: since horizontal derivatives are computed in an inherently asymmetric manner, namely in the direction of increasing x , small differences on the order of machine epsilon appear between the solution $x < 500$ m versus $x > 500$ m. The oscillatory signal in the vertical momentum is

attributed to strong vertically propagating sound waves that emerge from the initial perturbation being reflected by the no-flux boundary condition at the top and bottom of the model grid. Note that it is not expected that vertical momentum is conserved due to the presence of gravitational forcing.

2.5 Conclusions

The idea of separating the vertical and horizontal dynamics in atmospheric modeling systems has roots in the scale differences that characterize atmospheric flows. This principle has been fully exploited in the development of global and mesoscale models, along with the application of the hydrostatic approximation. This paper adds to the modern literature on modeling atmospheric dynamics by analyzing a novel discretization technique for achieving high-order accuracy in the vertical while maintaining the desirable properties of staggered methods. We refer to this technique as the Staggered Nodal Finite Element Method (SNFEM).

The test suite we present in this work is not exhaustive, but it is intended to evaluate the performance of the numerical schemes under conditions of near hydrostatic synoptic scale flow in section 2.4.1, linear, mesoscale, non-hydrostatic flow with topography in section 2.4.2, and fully nonlinear, non-hydrostatic, Large Eddy Simulation (LES) scale, flow in section 2.4.3 and section 2.4.4. As global models progress into the regime of non-hydrostatic flows, real flow cases will be characterized by one or more of the properties mentioned, and likely in combination when variable or adaptive meshing methods are used. More importantly, we expect that uniform or mixed grids being prepared in research will begin to span the scale range that includes the transition to non-hydrostatic dynamics and on to large-eddy flows.

In general, we postulate that a higher-order method based on finite elements will be more accurate at a given resolution with minimal computational cost relative to a low-order method. Our results demonstrate that a high-order vertical coordinate approximates well resolved, reference results at coarser resolutions that would be otherwise considered poorly represented. Our

Chapter 2. The Staggered Nodal Finite-Element Method

experiments nonetheless are constrained by the order of horizontal and temporal discretizations. Therefore, we restrict our recommendation to the use of 4th order SNFEM as optimum for the tests given here. In general the combined spatial order of accuracy should be consistent to maximize the effect of increased accuracy. The high-order approximation provides an improvement to the vertical dynamics and so reduces the need for higher vertical resolution. This benefit would prove effective when variable-grid methods are considered and nesting mesh levels can be saved by employing the SNFEM at high-order. The use of staggering in conjunction with high-order has further benefits, in particular the avoidance of stationary computational modes that are known to persist with co-located methods.

However, there are some trade offs when increasing the vertical order: 1) for a vertically implicit method, fewer high-order elements lead to a dense matrix structure that is more expensive to invert, 2) the oscillatory nature of the polynomial functions that make up the interpolants within an element have physical consequences (involving nonlinear processes) at the smallest scales, and 3) higher-order spatial discretizations often require smaller time steps or higher order temporal discretizations. Fig. 2.4 shows the times required for computations of varying vertical order and processor scaling. The results confirm that the relative cost in moving to 4th order is indeed modest relative to the use of higher orders.

The first point can be addressed in the construction of the software where parallelization and correct use of hardware resources minimizes the dense operations that high-order elements imply. We saw in fig. 2.19 that oscillations associated with high-order interpolants helped to approximate fine scale structures, but these oscillations can also be harmful depending on the flow condition. While vertical order of accuracy can be increased up to the total number of vertical levels, e.g. results from the Schär cases in fig. 2.9, increasing computational expense indicates that intermediate orders of accuracy will generally be most effective. In this study, many of the results at 4th order sufficiently improve solutions relative to low-order alternatives.

Furthermore, when physical instabilities arise, a consistent, high-order, and scale selective dissipation strategy is necessary. In this regard, finite element methods allow for the construction of

Chapter 2. The Staggered Nodal Finite-Element Method

diffusion operators for this purpose e.g. section 2.3.2. We can experiment with different combinations of diffusion operators including coefficients that are variable in space. While scale-selective 4th order operators with some grid resolution dependence are sufficient for this work, we intend to explore a wider range of strategies based on polynomial filtering, variational multiscale methods, etc. with the goal of eliminating the tuning procedure associated with user-provided coefficients.

The numerical dissipation strategy implemented here serves two primary goals: 1) stabilization of the computations and 2) as a form of closure for the Euler equations solved on a truncated grid. The methods we employ allow for the construction of derivative operators of various orders in a consistent manner. Tempest features a system that allows for diffusion to be applied in a selective manner on variables that is split according to the time integration scheme.

Further experiments are necessary to test the extent of the third point above. For this work, we used a 2nd order Strang time integration scheme (section 2.3.3) that was sufficiently robust to carry out all of the experiments up to 10th order without overly restricting time step size relative to the 2nd order simulations.

The authors conclude the following based on the experiments conducted and properties of the SNFEM:

1. Staggering has been generalized to finite element methods combining continuous and discontinuous formalisms. The result is a method that closely parallels the behavior of staggered finite differences eliminating stationary modes. This is strictly true for the lowest order finite elements and we restrict ourselves to observe that consistent behavior extends to high-order staggered elements pending a formal wave analysis.
2. Variable order of accuracy is an effective strategy that can compensate for limitations in grid scale resolution. However, the effects at very high order must be understood and controlled with appropriate stabilization methods. In general, “intermediate” orders (about 4th order) are recommended with consideration for consistency in overall spatial order given an IMEX partitioned architecture

Chapter 2. The Staggered Nodal Finite-Element Method

We emphasize that, while the equations are formulated in a coordinate-free manner, the results given all correspond to regular Cartesian coordinates as defined by the metrics in eqs. (2.22) and (2.21). Experiments corresponding to small planet and global domains are left for a subsequent work. However, any curved geometry with a terrain-following surface topography can be applied to the equations since all grid information is held in the metric terms described in section 2.2. As such, the effects of curved geometry and variable vertical order-of-accuracy are only addressed here in the Schär and Baroclinic wave cases (using the β plane approximation). From a design perspective, metric terms are precomputed and derivative operators are built in the natural, local coordinate frame when any grid is used.

Tempest is constructed to provide a unified multi-scale platform for atmospheric simulation. Experiments can be carried out readily at all scales of importance from long-term climate simulations to high-resolution weather prediction. Development is underway to include moisture transport and phase transformations as well as to further improve time integration performance. Coupled with highly accurate, efficient, and robust methods to compute dynamics, Tempest will evolve to produce reliable precipitation forecasts as well as long-term climate simulations as part of the greater effort to understand the impending challenges brought on by rapid climate change.

Chapter 3

An Orographically Forced Shear Flow Linear Model for Numerical Test Design and Validation

3.1 Introduction

The next generation of global and regional climate/weather models incorporate many advances in computational, mathematical and numerical methods that will guide our study of the Earth system in an accurate and robust manner. Atmospheric models based on approximated equations (linear, hydrostatic, shallow water, boussinesq, etc.) benefit from analytical solutions used to establish their characteristics, virtues and limitations. Here we propose a hierarchical approach based on the linear theory of mountain waves, basic fluid dynamic analysis, and properties of the numerical integration to validate the performance of a modern dynamical core in reproducing orographic waves. Our objective is to leverage and extend the linear theory in order to design numerical experiments efficiently under linear and nonlinear conditions.

Despite the usefulness of classical linear theory of mountain waves (Smith, 1979; Smith, 1980), there is a significant gap in applicability to modern high-resolution numerical simulations that incorporate fewer assumptions and simplifications, but incompatible boundary conditions. Results from linear analytical models can only be compared, quali to numerical model output under very specific conditions; uniform stratification with constant wind (Schär et al., 2002), multilayer atmospheres with piecewise linear shear and stratification (Klemp and Lily, 1975), and various studies where WKB solutions are invoked under slowly varying background fields (Teixeira, 2014). Computational studies of mountain wave interaction with large scale flows have been done successfully by Chen, Durran, and Hakim (2005) and Chen, Durran, and Hakim (2006) for example, using idealized geometries, but always in reference to the classical Boussinesq linearized theory. These specialized modeling efforts have established the value of numerical integrations in addressing transient, nonlinear phenomena that must also be captured accurately by general purpose modeling systems. Our objective is to present a robust methodology to conduct mountain wave experiments using advanced numerical models. Our method is composed of the following: 1) a reference solution suitable for direct comparison with numerical model output under general background conditions, and 2) an efficient way to design boundary conditions in truncated

Chapter 3. Linear Reference Model

domains minimizing the number of iterations.

In this work we present a novel method of computing linear solutions for 2-D mountain wave simulations using terrain-following coordinates. The method is semi analytic in that derivatives are treated as truncated global basis expansions in Hermite functions (horizontal) and Legendre polynomials (vertical). The Hermite function basis is chosen to approximate infinite lateral boundaries with grid clustering where terrain features are specified. Reference solutions are then possible for more complicated background states including finite shear and nonuniform without any restriction on the magnitude of the variations. Our reference solution is thus an extended variant of the classical theory applicable to a more general class of problems.

In order to demonstrate our methodology, we use the Schär Mountain profile (Schär et al., 2002) as prototype topography and extend the classical test case to include directional shear and a piece-wise continuous thermodynamic background. We note that general terrain profiles may be prescribed as well. We will focus on direct comparisons of vertical velocity and momentum flux between high fidelity simulations (spatial resolution of 200 m and 4th order discretization) and a semi-analytical treatment of the linearized non-hydrostatic, inviscid equations in terrain-following coordinates.

The remainder of this paper is organized as follows: We introduce the governing equations in section 3.2. Then, in section 3.3, we proceed to develop the semi-analytical reference solution method, based on truncated global polynomial expansions, for the linear equation set at steady state. Using the linear solution we develop a numerical test (section 3.4) of jet flow past a Schär profile in a non-uniformly stratified background state. We show validation results in section 3.5 for a peak mountain height of 10 m comparing the linear model with long term numerical solutions. Lastly, we present a qualitative analysis of wave breaking simulations economically designed using the linear reference model.

3.2 The 2-D linearized equations in terrain-following Cartesian coordinates

In order to find a reference solution the Cartesian non-rotating equations (prior to linearization) in terrain-following coordinates are cast as follows,

$$\begin{aligned}
 \frac{\partial u}{\partial t} + u \frac{\partial u}{\partial x} + w \frac{\partial u}{\partial z} + \frac{p}{\rho} \frac{\partial \ln p}{\partial x} &= 0 \\
 \frac{\partial w}{\partial t} + u \frac{\partial w}{\partial x} + w \frac{\partial w}{\partial z} + \frac{p}{\rho} \frac{\partial \ln p}{\partial z} &= 0 \\
 \frac{1}{\gamma} \frac{\partial \ln p}{\partial t} + \frac{u}{\gamma} \frac{\partial \ln p}{\partial x} + \frac{w}{\gamma} \frac{\partial \ln \rho}{\partial z} + \frac{\partial u}{\partial x} + \frac{\partial w}{\partial z} &= 0 \\
 \frac{\partial \ln \theta}{\partial t} + u \frac{\partial \ln \theta}{\partial x} + w \frac{\partial \ln \theta}{\partial z} &= 0
 \end{aligned} \tag{3.1}$$

$$\tag{3.2}$$

where by the Chain Rule,

$$\begin{aligned}
 \frac{\partial}{\partial z} &= \sigma \frac{\partial}{\partial \xi}, \\
 \sigma &= H \frac{\partial \xi}{\partial z}, \\
 \frac{\partial \xi}{\partial x} &= \sigma \frac{\partial z}{\partial h} \frac{\partial h}{\partial x}.
 \end{aligned} \tag{3.3}$$

and horizontal x derivative operators are expanded using the terrain-following horizontal coordinate α as,

$$\frac{\partial}{\partial x} = \frac{\partial}{\partial \alpha} - \frac{\partial \xi}{\partial x} \frac{\partial}{\partial \xi} \tag{3.4}$$

represents the projection of flow components following terrain surfaces onto the Cartesian x

Chapter 3. Linear Reference Model

direction. Here, H is the model top, u and w are the Cartesian velocity components, and ρ , p are density and pressure respectively. The metric quantity in (3.3) is known from the elevation function $h(x)$ and the decay of terrain features with height specified in the choice of vertical coordinate mapping.

The total prognostic state is decomposed into background (over bar) and perturbation (primed) components as follows:

$$\begin{aligned}u &= \bar{u}(z) + u'(x, z, t), \\w &= w'(x, z, t), \\\ln p &= \ln \bar{p}(z) + (\ln p)'(x, z, t), \\\ln \theta &= \ln \bar{\theta}(z) + (\ln \theta)'(x, z, t).\end{aligned}\tag{3.5}$$

where $\bar{u}(z)$, $\bar{\rho}(z)$, and $\bar{p}(z)$ are the height dependent, steady background jet and thermodynamic profiles. These may be continuous analytic or piecewise continuous functions where discontinuous gradients are admissible by our solution method. Also, note that the decomposition of thermodynamic quantities applies to the natural logarithm of density and pressure in order to better approximate the “small perturbation” assumption in the subsequent linearization.

We now substitute the decomposition (3.5) along with derivative expansions (3.3) and (3.4) into equations (3.1) and applying the following for all background quantities q ,

$$\frac{\partial \bar{q}}{\partial x} = 0.\tag{3.6}$$

then,

$$\begin{aligned}
 \bar{u} \frac{\partial u'}{\partial x} + \sigma \frac{\partial \bar{u}}{\partial \xi} w' + \frac{\bar{p}}{\bar{\rho}} \frac{\partial (\ln p)'}{\partial x} &= 0, \\
 \bar{u} \frac{\partial w'}{\partial x} + g_c \left(\frac{1-\gamma}{\gamma} \right) (\ln p)' - g_c (\ln \theta)' + \sigma \frac{\bar{p}}{\bar{\rho}} \frac{\partial (\ln p)'}{\partial \xi} &= 0, \\
 \gamma \frac{\partial u'}{\partial x} + \gamma \sigma \frac{\partial w'}{\partial \xi} + \sigma \frac{\partial \ln \bar{p}}{\partial \xi} w' + \bar{u} \frac{\partial (\ln p)'}{\partial x} &= 0, \\
 \sigma \frac{\partial \ln \bar{\theta}}{\partial \xi} w' + \bar{u} \frac{\partial (\ln \theta)'}{\partial x} &= 0.
 \end{aligned} \tag{3.7}$$

Therefore, it is possible to rearrange the system into a global differential operator L plus an algebraic operator B with a known forcing F depending on the thermodynamic background and the vertical coordinate. Assuming a prognostic vector $\mathbf{q} = [u' \ w' \ (\ln p)' \ (\ln \theta)']^T$, the interior system may be written as

$$(\mathbf{L} + \mathbf{B})\mathbf{q} = \mathbf{0}, \tag{3.8}$$

where

$$\mathbf{L} + \mathbf{B} = \begin{bmatrix} \bar{u} \frac{\partial}{\partial x} & 0 & \frac{\bar{p}}{\bar{\rho}} \frac{\partial}{\partial x} & 0 \\ 0 & \bar{u} \frac{\partial}{\partial x} & \sigma \frac{\bar{p}}{\bar{\rho}} \frac{\partial}{\partial \xi} & 0 \\ \frac{\partial}{\partial x} & \sigma \frac{\partial}{\partial \xi} & \bar{u} \frac{\partial}{\partial x} & 0 \\ 0 & 0 & 0 & \bar{u} \frac{\partial}{\partial x} \end{bmatrix} + \begin{bmatrix} v_1(x, z) & \sigma \frac{\partial \bar{u}}{\partial \xi} & 0 & 0 \\ 0 & v_2(x, z) & g_c \left(\frac{1-\gamma}{\gamma} \right) & (-g_c) \\ 0 & \sigma \frac{\partial \ln \bar{p}}{\partial \xi} & v_3(x, z) & 0 \\ 0 & \sigma \frac{\partial \ln \bar{\theta}}{\partial \xi} & 0 & v_4(x, z) \end{bmatrix}, \tag{3.9}$$

Chapter 3. Linear Reference Model

It is essential that we impose a set of boundary conditions identical to what is used in a general-purpose dynamical core. Reference solutions based on unbounded domains along with the application of radiative boundary conditions (Klemp and Lily, 1975; Klemp, Skamarock, and Fuhrer, 2003; Durran, 2010) present persistent discrepancies relative to simulation results that can only be reconciled by implementing identical, if imperfect, boundary conditions. The combination of top/bottom boundaries and absorption layers is needed to perform validation studies of nonlinear model output. Thus, in our linear reference solution for perturbation quantities ψ , this implementation of an absorption layer corresponds to augmenting the tendency equations as:

$$\frac{\partial \psi}{\partial t} = \dots - \nu \psi \quad (3.10)$$

This results in exponential decay of the perturbation field at a rate proportional to the absorption layer strength. This is directly analogous to implementations in numerical models where fields are relaxed to an arbitrarily chosen reference state; typically the initialization of the evolution equations. Solving the linear system in this manner will be used to more efficiently design an optimal absorption layer implementation with the purpose of minimizing boundary reflections in wave breaking simulations. Our present approach is useful in determining a suitable set of absorption layer parameters (depth, strength, and shape) and in finding a reference solution with boundary conditions exactly like those used in numerical models with capped atmospheres.

An analysis of equations (3.7) by combining the thermodynamic equation algebraically into the horizontal momentum equation reveals a constraint for the vertical variation of vertical velocity as follows:

$$\frac{\partial w}{\partial z} + \left(\frac{d \ln \bar{\theta}}{dz} + \frac{d \ln \bar{\rho}}{dz} - \frac{d \ln \bar{u}}{dz} \right) w + \left(\frac{\gamma R_d \bar{T} - \bar{u}}{\bar{u}} \right) \frac{\partial (\ln p)'}{\partial x} = 0 \quad (3.11)$$

Chapter 3. Linear Reference Model

If we neglect the contribution from horizontal pressure gradients from (3.11), then a first order ordinary differential equation in w remains:

$$\frac{\partial w}{\partial z} \approx \left(-\frac{d \ln \bar{\theta}}{dz} - \frac{d \ln \bar{\rho}}{dz} + \frac{d \ln \bar{u}}{dz} \right) w \quad (3.12)$$

If we consider only real exponential solutions to (3.12), then we see that vertical decreases in mass and potential temperature produce wave growth, while background shear may be characterized by wave growth where speed decreases and vice versa. Under stable, stratified conditions supporting gravity waves, $\bar{\theta}$ is strictly increasing while $\bar{\rho}$ decreases rapidly (nearly exponentially) and is known to dominate linear wave growth. Our linear model captures stabilizing/destabilizing interactions due to background conditions in a more general sense.

3.2.1 A new vertical coordinate transformation with uniform smooth decay

The canonical example for a vertical transform given by Gal-Chen and Somerville (1975) with linear decay of terrain features would result in

$$z(x, \xi) = \xi (H - h(x)) + h(x), \quad (3.13)$$

and terms in (3.3) become

$$\frac{\partial \xi}{\partial z} = \frac{1}{H - h} \quad (3.14)$$

$$\frac{\partial z}{\partial h} = 1 - \xi \quad (3.15)$$

However, for the purpose of this work and subsequent studies we seek a coordinate transformation that aggressively eliminates terrain features from coordinate surfaces away from the boundary corrugation profile. The purpose of such a terrain decay function is to minimize the influence of deformed coordinate surfaces in the interior of the flow. In particular, we avoid this

Chapter 3. Linear Reference Model

influence in the region roughly 2 kilometers above the mountain, and in the vicinity of the absorption layers. Therefore, we introduce a new coordinate characterized by the decay function:

$$\frac{\partial z}{\partial h} = e^{(-\frac{P}{Q}\zeta)} \left[\cos \left(\frac{\pi}{2}\zeta \right) \right]^P + A\zeta(1 - \zeta) \quad (3.16)$$

where parameters $P = 20$, $Q = 5$ and $A = 1.0 \times 10^{-3}$ are chosen.

The function (3.16) has vertical gradient controlled by P and Q at $\zeta = 0$, A at $\zeta = 1$, and is therefore monotonically decreasing, but terrain features decay more rapidly with height compared to (3.13). A comparison of the standard coordinate and that given here is shown in Figure 3.1. The derivative $\partial\zeta/\partial z$ is available by applying implicit differentiation (shown in Appendix B) on the following relation that defines a linear vertical coordinate transformation

$$z(x, \zeta) = H\zeta + \frac{\partial z}{\partial h} h(x). \quad (3.17)$$

The vertical coordinate transformation maps the physical terrain following z to a uniform, normalized (by H) computational coordinate $\zeta \in [0, 1]$ by way of an invertible, monotone relationship. If we consider the general form of the metric term σ given the derivative,

$$\frac{d\zeta}{dz} = \left\{ H + h(x) \left[\frac{d}{d\zeta} \left(\frac{dz}{dh} \right) \right] \right\}^{-1} \quad (3.18)$$

where details are defined in Appendix B. Here H is the model top, then we see that the influence of the terrain following metric behaves as H^{-1} and thus vanishes when $H \rightarrow \infty$. This is consistent with results for unbounded domains in the vertical.

We note that other coordinate surface definitions with nonlinear decay of terrain features may be used such as those introduced by Schär et al. (2002) where different exponential decay rates were applied to individual components of the terrain spectrum. We implement a simpler solution based in the physical space in order to be consistent with what is done in general purpose modeling systems. Our reference solution allows for the implementation and verification of any

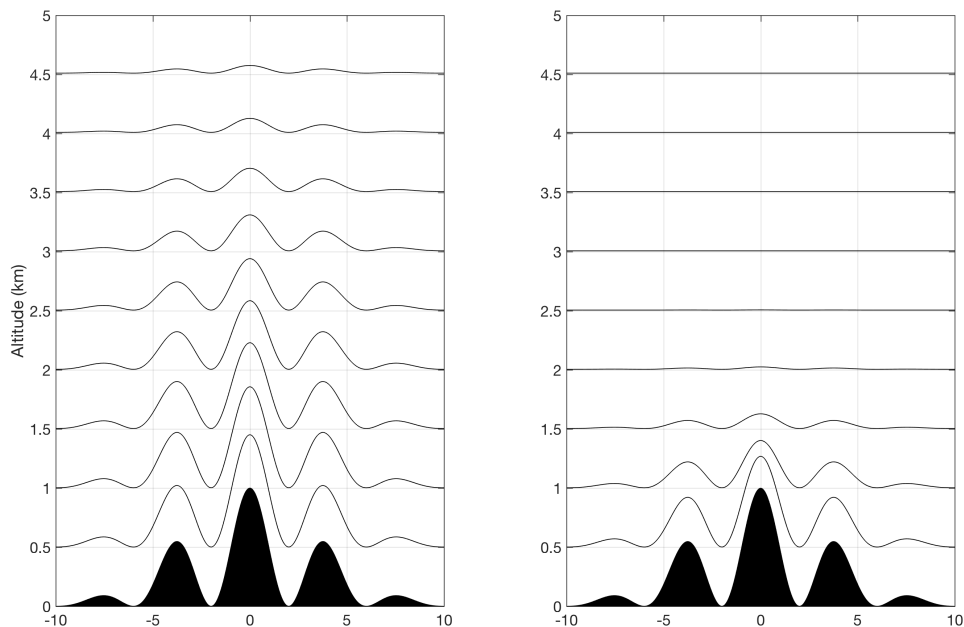


FIGURE 3.1: Comparison of terrain decay functions. The coordinate of Gal-Chen and Somerville (1975) left and (3.16) right showing decay of terrain features near boundary terrain.

choice of vertical transform (in physical space) intended for computational use.

3.3 Semi-analytic reference solution of the perturbation equations

The solution strategy for the system defined in equations (3.9) involves finding a suitable spectral transformation for x and z derivatives in \mathbf{L} and computing all the quantities in \mathbf{B} and \mathbf{F} from known data using analytical expressions where possible. In this study, the thermodynamic background will be based on a piecewise temperature profile resulting in analytical expressions for vertical gradients of pressure and density by way of the hydrostatic assumption. Our zonal jet will be prescribed as an analytical function of height with a corresponding vertical gradient profile. We note that considerable freedom exists in defining these quantities from observational data and computing gradients in any approximate manner.

Chapter 3. Linear Reference Model

Derivative operators in \mathbf{L} are converted to dense matrices using global Hermite Functions in the α direction and Legendre polynomials in ζ . In particular, the Hermite function expansion is chosen in the horizontal direction as this incorporates a good approximation to inflow-outflow lateral boundaries. The Legendre basis used in the vertical is chosen to include Dirichlet boundary conditions on the vertical velocity field i.e. terrain forcing and model top conditions.

Projection of derivatives onto orthogonal polynomials is a common discretization strategy and the foundation of spectral element methods applied on sub-domains. Here we use a global basis of Hermite Functions and Legendre polynomials in order to arrive at a global spectral derivative operator for \mathbf{L} that, combined with sampled versions of \mathbf{B} and \mathbf{F} result in a linear system of equations with a large, non symmetric, dense coefficient matrix.

Given a discrete set of nodes $x_i \in -L, L$ for $i = 1, N$ where N is a positive integer, x_i are the zeros of Hermite Functions up to order $N - 1$. Then, following Shen, Tang, and Wang (2011), the horizontal derivative matrix operator is:

$$\frac{\partial}{\partial \alpha} = \mathbf{D}_x = D_{ij} = \begin{cases} \frac{\hat{H}_N(x_i)}{\hat{H}_N(x_j)} \left(\frac{1}{x_i - x_j} \right) : i \neq j \\ 0 : i = j \end{cases} \quad (3.19)$$

where \hat{H} are the Hermite Functions up to order N computed in recursive fashion. The implementation is accomplished with the derivative matrix package of (Weideman and Reddy, 2000).

For the domain interval $-L, L$ the nodes and derivative matrix (3.19) are scaled by L as needed in the Hermite weight function $e^{-\frac{x^2}{2L}}$.

Similarly, with a set of discrete nodes $z_k \in [0, H]$ for $k = 1, N$ where N is a positive integer, z_k are the Chebyshev nodes up to order N distributed over the given interval. Again, following

Shen, Tang, and Wang (2011), the vertical derivative matrix operator is:

$$\frac{\partial}{\partial \zeta} = \mathbf{D}_z = D_{kj} = \begin{cases} \frac{\mathcal{L}'_N(x_k)}{\mathcal{L}'_N(x_j)} \left(\frac{1}{x_k - x_j} \right) : k \neq j \\ \frac{x_k}{1 - (x_k)^2} : k = j \end{cases} \quad (3.20)$$

where \mathcal{L}' are the derivatives of Lagrange basis polynomials up to order N computed in recursive fashion. Again, we implement this discrete derivative with the matrix package of (Weideman and Reddy, 2000).

The derivative matrices (3.19) and (3.20) are not suitable for computational purposes, but are known to represent the respective partial derivatives with very high accuracy well beyond that of a true numerical method. Function expansions and nodal values are collocated giving a grid-scale defined by the highest order function included over the extent of the domain. For our purposes, with a horizontal extent of 100 km and heights up to 40 km, it is sufficient to retain 120 modes in the horizontal and 100 in the vertical to produce an accurate truncation.

3.3.1 Boundary conditions and terrain forcing

The free-slip condition at the terrain surface is imposed by stating that the component of the velocity normal to the terrain must vanish. That is,

$$\vec{\mathbf{u}} \cdot \hat{\mathbf{n}} = \vec{\mathbf{u}} \cdot \frac{\vec{\nabla} \phi}{|\vec{\nabla} \phi|} = 0, \quad (3.21)$$

where $\phi = z - h(x) = 0$ is the level set representation of the terrain surface.

Chapter 3. Linear Reference Model

If the gradient of ϕ in Cartesian geometry is $\vec{\nabla}\phi = -\frac{\partial h}{\partial x}\hat{\mathbf{i}} + \hat{\mathbf{k}}$, then following (3.21) the kinematic boundary condition is stated as

$$w' - u' \frac{dh}{dx} = \bar{u} \frac{dh}{dx}. \quad (3.22)$$

Here, a further approximation may be taken where the term $u' \frac{\partial h}{\partial x}$ is regarded as a product of perturbation quantities and hence neglected. Thus the consistent linear terrain boundary condition is,

$$w' = \bar{u} \frac{dh}{dx}. \quad (3.23)$$

Applying the derivative matrix operators in (3.19) and (3.20) to the continuous system (3.9), we arrive at a matrix equation $Ax = b$ where A is non-symmetric and augmented with the boundary equations (3.23) at the bottom z surface and $w' = 0$ at the model top. The method of Lagrange Multiplier augmentation is used by appending $2N$ unknown constraint forces corresponding to the top and bottom boundary grid locations. Furthermore, evaluating (3.9) with (3.23) leads to the following set of equations at the (bottom) boundary in Cartesian horizontal x and vertical z coordinates,

$$\begin{aligned} \bar{u} \frac{\partial u'}{\partial x} + \frac{\bar{p}}{\bar{\rho}} \frac{\partial (\ln p)'}{\partial x} &= -\frac{\partial \bar{u}}{\partial z} \bar{u} \frac{\partial h}{\partial x'} \\ \gamma \frac{\partial u'}{\partial x} + \bar{u} \frac{\partial (\ln p)'}{\partial x} &= -\gamma \frac{\partial h}{\partial x} \frac{\partial \bar{u}}{\partial z} - \bar{u} \frac{\partial (\ln \bar{p})}{\partial z} \frac{\partial h}{\partial x'} \\ \bar{u} \frac{\partial}{\partial x} \left[(\ln \theta)' + \frac{\partial (\ln \bar{\theta})}{\partial z} h \right] &= 0. \end{aligned} \quad (3.24)$$

where horizontal momentum and pressure equations may be algebraically combined to give,

$$\begin{aligned} \bar{u} \frac{\partial}{\partial x} \left[\left(\bar{u} - \gamma \frac{\bar{p}}{\bar{\rho} \bar{u}} \right) (\ln p)' + h \frac{\partial (\ln \bar{p})}{\partial z} \right] &= 0, \\ \bar{u} \frac{\partial}{\partial x} \left[(\ln \theta)' + h \frac{\partial (\ln \bar{\theta})}{\partial z} \right] &= 0. \end{aligned} \quad (3.25)$$

A similar analysis for the top boundary reveals that, given a specified vertical velocity, the top and bottom boundaries must further be constrained to specified values in two of the remaining three fields in order to fully determine the linear system. Equation (3.25) states (assuming u is eliminated from (3.24)) that total internal energy and entropy do not vary in the horizontal direction at the terrain and model cap boundaries i.e. there is no horizontal transport of energy/entropy. Note that the vertical momentum equation is eliminated at the top and bottom surfaces since it would imply a static force constraint that is inconsistent at time invariant, impenetrable boundaries.

3.4 The sheared jet Schär Mountain test

The Schär Mountain test case given in Schär et al. (2002) has been used extensively in the development of dynamical cores. It is valuable for testing vertical discretizations and to show the wave dispersion properties of a particular model as in Giraldo and Restelli (2008) and Guerra and Ullrich (2016) as examples. The primary simplifications are that the background flow is uniform and constant while the reference thermodynamic profile is uniformly stratified. Depending on implementation details in a particular model, numerical results may be compared directly to analytical solutions based on the 2-D Boussinesq equations as shown by Smith (1979) or Klemp, Skamarock, and Fuhrer (2003). In this scenario the background stratification and flow fields allow the constant coefficient equations to be reduced to a single second order system and transformed to Fourier space closed solutions are attainable.

Here we present an extension to the classic Schär Mountain test case that allows for piecewise

Chapter 3. Linear Reference Model

linear continuous background temperature fields and a sheared jet with arbitrary shape. The linearized equations (3.7) applicable to such a situation are closer to more general unapproximated systems employed in modern dynamical cores with strongly varying background fields in a terrain following grid.

The topographic profile is given by

$$h_T(x) = h_c \exp \left[- \left(\frac{x}{a_c} \right)^2 \right] \cos^2 \left(\frac{\pi x}{\lambda} \right), \quad (3.26)$$

with parameters $h_c = 100$ m or a value less than $\frac{\bar{U}}{N}|_s$ corresponding to streamline separation at the surface, $\lambda = 4000$ m and $a_c = 5000$ m. The simulation domain is $(x, z) \in [-56, 56] \times [0, 30]$ km with a no-flux boundary specified along the top surface and a free-slip condition along the terrain. Free-flow boundary conditions for simulation use an absorption layer 10 km wide along the lateral boundaries and 10 km deep at the model top.

3.4.1 Background jet

The background jet profile is modified from Ullrich and Jablonowski (2012) and used in Ullrich, Reed, and Jablonowski (2015) to add a mean uniform wind:

$$\bar{u}(z) = -u_j (\ln \eta) e^{\frac{-\ln \eta}{b^2}} + u_0 \quad (3.27)$$

where u_j gives the amplitude of the jet core, b is a parameter that changes the amplitude and location of the jet, and u_0 is a constant wind. The variable $\eta = \frac{\bar{p}(H\zeta)}{p_0}$ is a normalized pressure coordinate determined from the thermodynamic background state in the terrain following coordinate ζ . The parameters in (3.27) for this study are given in Table 3.1.

The resulting background flow has a speed of 10 m s^{-1} at ground level and grows to approximately 20 m s^{-1} at 7km elevation representative of a moderate mid-tropospheric jet with a constant low level flow in conditions sufficient to launch mountain waves through the jet core.

Chapter 3. Linear Reference Model

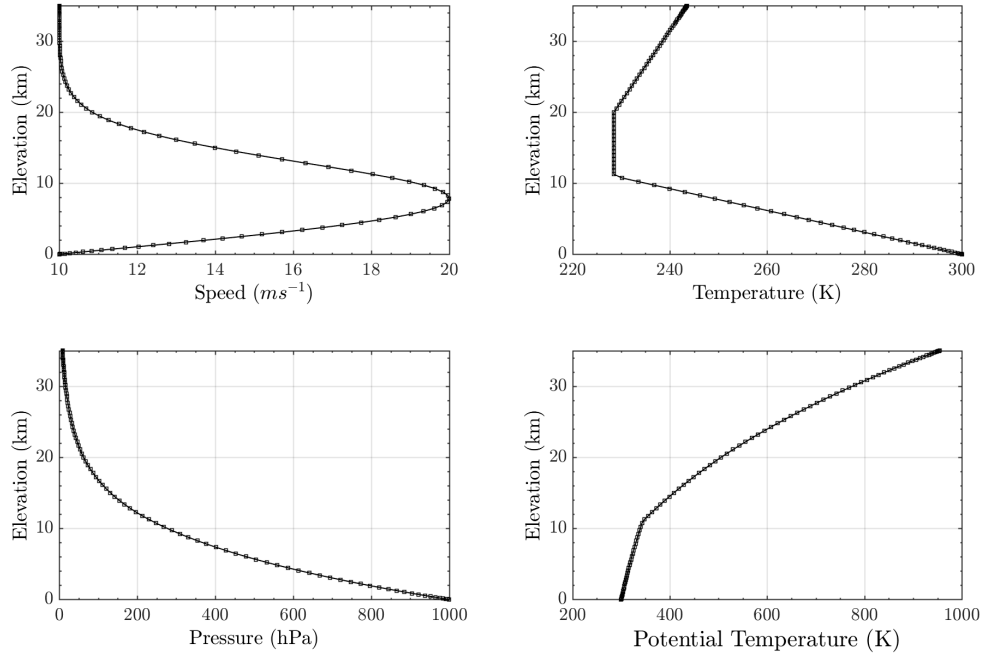


FIGURE 3.2: Background wind and thermodynamic profiles. Dry atmosphere with a prescribed sensible temperature distribution (top right).

Parameter	Value
u_j	16.822 ms^{-1}
u_0	10.0 ms^{-1}
b	1.386
p_0	$1.0E5 \text{ Pa}$

TABLE 3.1: Background jet parameters.

3.4.2 Thermodynamic and kinematic background initial state

The thermodynamic background fields are derived from a temperature profile with parameters given in Table 3.2. The initial kinematic and thermodynamic conditions are shown in Figure 3.2. Fields for pressure $\ln \bar{p}(z)$ and density $\ln \bar{\rho}(z)$ are calculated from hydrostatic balance and integrated over each isothermal or constant lapse rate layer. We note that any number of layers may be specified this way and the model also accepts discrete sounding data of any type. For a piecewise linear temperature profile in 3 layers, pressure, density, and their respective vertical gradients are computed analytically by

$$\ln \bar{p}(z) = -g_c \frac{1}{R_d \Gamma} \ln \left(\frac{T_1 - \Gamma z}{T_1 - \Gamma z_1} \right) + \ln p_1, \quad (3.28)$$

$$\frac{\partial}{\partial z} \ln \bar{p} = -g_c \frac{1}{R_d (T_1 - \Gamma z_1)} \left(\frac{T_1 - \Gamma z}{T_1 - \Gamma z_1} \right)^{-1} \quad (3.29)$$

where $R_d = 287.0$ is the gas constant for dry air, T_1 and z_1 are the temperature and elevation at the bottom of the layer. Note that $\Gamma = -\frac{\partial T}{\partial z}$ is used in direct proportion to the gradient of temperature taken to be constant in each layer.

Similarly, the background pressure field in a layer with constant temperature change is given as

$$\ln \bar{p}(z) = -g_c \frac{1}{R_d \bar{T}} \ln (z - z_1) + \ln p_1, \quad (3.30)$$

$$\frac{\partial}{\partial z} \ln \bar{p} = -g_c \frac{1}{R_d \bar{T}} \quad (3.31)$$

where \bar{T} is the layer temperature taken from the layer below. The normalized pressure coordinate η is thus readily obtained in computing the zonal jet from the pressure profile defined above.

Layer (km)	$\frac{\partial T}{\partial z}$ Km ⁻¹
$z \in [0 \ 11]$	-0.0065
$z \in [11 \ 20]$	0.0 tropopause
$z \in [20 \ H]$	+0.001

TABLE 3.2: Background thermodynamic parameters.

Relationships for background density are readily attained by use of the Ideal Gas Law,

$$\ln \rho = \ln \left(\frac{p}{R_d T} \right) = \ln p - \ln T - \ln R_d, \quad (3.32)$$

and

$$\frac{\partial}{\partial z} \ln \rho = \frac{\partial}{\partial z} \ln p - \frac{\partial}{\partial z} \ln T = \frac{\partial}{\partial z} \ln p - \frac{\Gamma}{T}. \quad (3.33)$$

3.4.3 Comparison to the classical theory

One of the primary differences in our reference solution and those derived from the classical theory is the implementation of absorption layers in lieu of unbounded domains with radiation conditions. We show a comparison of the of the two solutions in the original Schär mountain test case (Schär et al., 2002) under uniform stratification in Figure 3.3 where differences due to the change in boundary condition are readily apparent. The two solutions are quite similar up to approximately 15km, but any comparison is necessarily qualitative. Furthermore, the governing equations and boundary conditions of the classical theory are too far removed from numerical model implementations to be used in validation studies. We note that both solutions are based on a truncated polynomial expansion approach where the classical theory is facilitated by the Fast Fourier Transform algorithm and our solution is subject to a sparse matrix inversion.

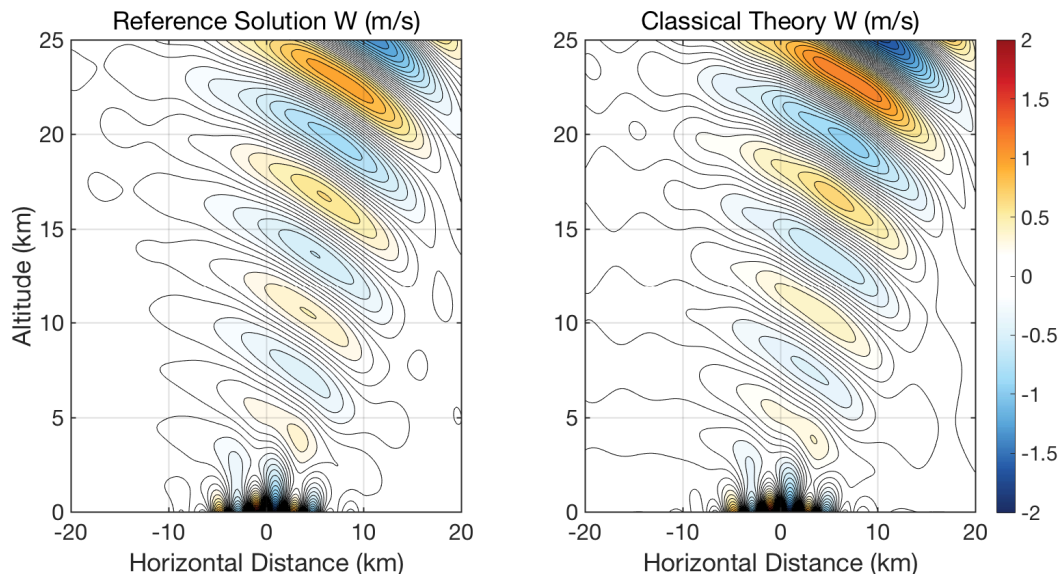


FIGURE 3.3: The original Schär mountain test case computed by our reference solution as compared to the classical theory Fourier solution.

The strength and width of the lateral/top absorption layers determine the extent of reflection noise. For the purpose of this study, our reference solution was used to tune a boundary with the thinnest and weakest layer possible and used these values in our numerical experiments. Absorption layers introduce non-trivial interactions with the interior flow that often require many iterations of a numerical model to optimize. In the case of orographic waves, two features are especially important: wavelength and amplitude of vertical modes as they meet the top layer, and strong trapped waves that may interact with the downstream lateral layer. While good estimate can be obtained from the linear theory, our model allows these interactions to be visualized and assessed quickly with the goal of minimizing the extent of the computational domain dedicated to the far field boundary condition.

Our linear model allows the process of layer optimization to be greatly reduced. However, we note that transient effects are not included and can dominate the numerical model response particularly just after initialization.

3.5 Numerical tests and results

Our goal is to demonstrate the validity of the model for conditions where purely analytical solutions are not available. Thus, we progress from constant wind and uniform background to an arbitrarily sheared wind in a background with discontinuous derivatives as a prototype for general wind and sounding profiles.

Horizontal and vertical resolutions are 1000, 500, 250, and 125 m. We compare the vertical velocity to the reference solution directly and compute the L_2 norm of the difference. Furthermore, we are interested in diagnosing momentum fluxes, and hence induced drag, using our linear solution as a reference. Here, we expected the momentum flux to be divergence-free. Lastly we evaluate the onset of shear and convective instability by computing the local Richardson number and vertical gradient of potential temperature. The purpose of these diagnostics is to efficiently design, given a set of general background conditions, numerical tests that will exhibit phenomena predicted by the linear model.

Numerical integrations are performed using the Tempest dynamical core with horizontal Spectral Element discretization and a Lorenz staggered FEM in the vertical as outlined in (Guerra and Ullrich, 2016). Steady state is assumed after a long term (15 hours) simulation with an explicit Runge-Kutta method. The tests are carried out without the use of any diffusion operators. However, some damping is required in the hyperbolic problem to remove transients borne of the impulsive initialization. Therefore, the model contains damping implicit to the time integration scheme and localized damping due to the use of absorption layers.

While we observe excellent agreement in prognostic and composite fields as shown in Figure 3.4, our numerical tests and the linear reference solution are convergent up to finite error for a given mountain height. This behavior is shown in the L_2 norm of differences in density and vertical momentum given in Figures 3.5 and 3.6. We note that the 3LAYER configuration initially appears to converge at a faster rate due to numerical errors in capturing the piece-wise background. However, this is only the case at lower resolutions where discontinuous derivatives are

Chapter 3. Linear Reference Model

most problematic. In contrast, we expect that smoothly varying (relative to the grid length) background fields would present uniform errors over the domain and result in a smaller error floor.

The reference solution based on the linearized equations (3.9) may be interpreted as the first iteration of Newton's Method applied to the full Euler equations where the initial Jacobian operator is evaluated at the background state. As such, the solution to the linear problem implies a residual with respect to the full non-linear equations. For the purpose analyzing the nonlinear residuals we employ an equivalent linearization of the equations in conservation form outlined in Appendix A. Therefore, if we assume that a nonlinear equilibrium solution exists and may be found by a Newton iteration we have, in the first two iterations,

$$\begin{aligned} \mathbf{q}' - \mathbf{q}_{\text{NL}} &= \bar{\mathbf{J}}^{-1}f(\bar{\mathbf{q}}) - \left[\bar{\mathbf{J}}^{-1}f(\bar{\mathbf{q}}) + \mathbf{J}(\bar{\mathbf{q}} + \mathbf{q}')^{-1}f(\bar{\mathbf{q}} + \mathbf{q}') + \dots \right] \quad (3.34) \\ \|\mathbf{q}' - \mathbf{q}_{\text{NL}}\| &\approx \|\mathbf{J}(\bar{\mathbf{q}} + \mathbf{q}')^{-1}f(\bar{\mathbf{q}} + \mathbf{q}')\| = \|\mathbf{U}\mathbf{S}\mathbf{V}^T f(\bar{\mathbf{q}} + \mathbf{q}')\| \Rightarrow \\ \|\mathbf{q}' - \mathbf{q}_{\text{NL}}\| &\approx \|\mathbf{S}f(\bar{\mathbf{q}} + \mathbf{q}')\| = \left[\sum_i \left(\frac{\mathbf{f}_i}{\lambda_i} \right)^2 \right]^{\frac{1}{2}} \geq \frac{1}{\lambda_{\max}} \|f(\bar{\mathbf{q}} + \mathbf{q}')\| \end{aligned}$$

where f represents the full Euler set evaluated at the current state $\bar{\mathbf{q}} + \mathbf{q}'$ and \mathbf{J} is the Jacobian operator initially evaluated at the background state. Also, λ_{\max} is the largest singular value of the Jacobian matrix evaluated after the first iteration and the last result follows from orthogonality of the right and left singular vector matrices \mathbf{U} and \mathbf{V} . The statement above indicates that there is a lower bound on the error attained by the linear solution and this is proportional to the norm of the residual in the full non-linear equations after one Newton iteration.

We now compute the nonlinear residual based on our linear solution to estimate the result of (3.34) in table 3.3 for the 3LAYER configuration. We observe a linear convergence rate in the reference solution model with respect to the fully nonlinear equations and furthermore have estimates for lower error bounds. The largest singular value of $\bar{\mathbf{J}}$ is approximately 80 and does not vary with peak terrain height. Thus, we see that minimum errors at the converged resolution of

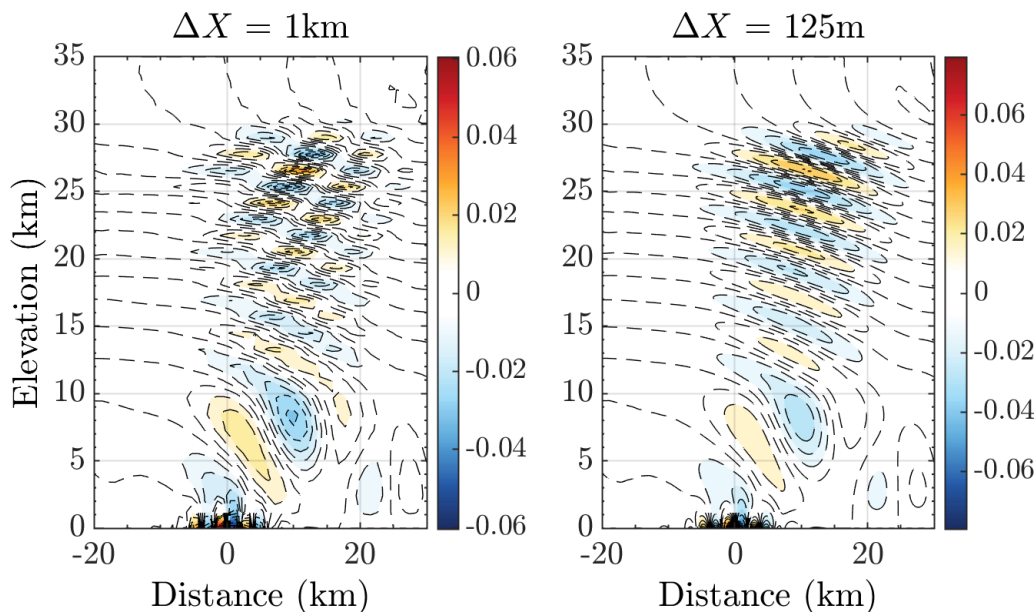


FIGURE 3.4: Overlay of numerical results and linear reference solution. Dashed contours represent the reference solution and filled contours correspond to numerical results at various resolutions. Vertical Velocity (m s^{-1}).

125m are proportional to the residual for vertical momentum. Density errors are, however, much greater than the lower bound and this is directly attributed to the rate at which the underlying discretization resolves discontinuities in the background fields. The pattern of oscillation in density is evident at 11km of elevation in figure 3.7.

While vertical momentum errors are on the order of a fraction of a millimeter per second, the relatively greater density errors cause a distinct pattern of reflected waves in the momentum field as shown in figure 3.8. This pattern is smooth and concentrated near the lateral and top boundaries. The latter case is potentially problematic for a nonlinear solution where wave breaking is to be expected as such wave reflections may precipitate instabilities and lead to incorrect structure in turbulent fields. We also notice significant errors within the lateral absorption layers coming from the numerical model indicating a strong resolution dependence for these layers. The linear reference solution serves a tool to minimize such errors by adjusting the domain size and depth/strength of the absorption layers. However, in the context of a higher order discretization,

Height (m)	Residual ρ	Residual ρw
10.0	5.9473×10^{-7}	8.5940×10^{-4}
1.0	5.9663×10^{-8}	8.5185×10^{-5}
0.1	5.9684×10^{-9}	8.5569×10^{-6}

TABLE 3.3: Nonlinear residuals in density ρ (kg m^{-3}) and vertical momentum ρw ($\text{kg m}^{-2} \text{s}^{-1}$) in the 3LAYER configuration.

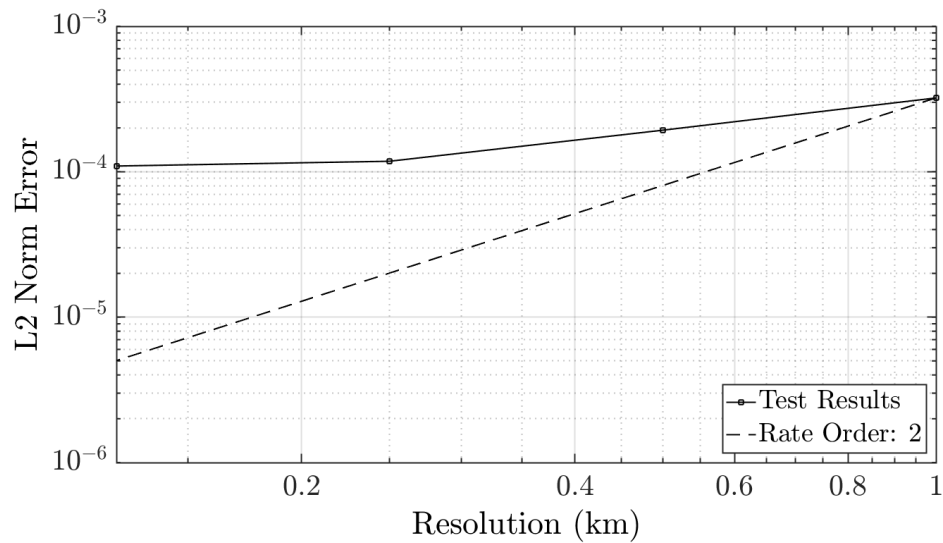


FIGURE 3.5: L_2 error convergence of numerical integration with respect to the semi-analytical reference solution. 10 m terrain height. Density (kg m^{-3}).

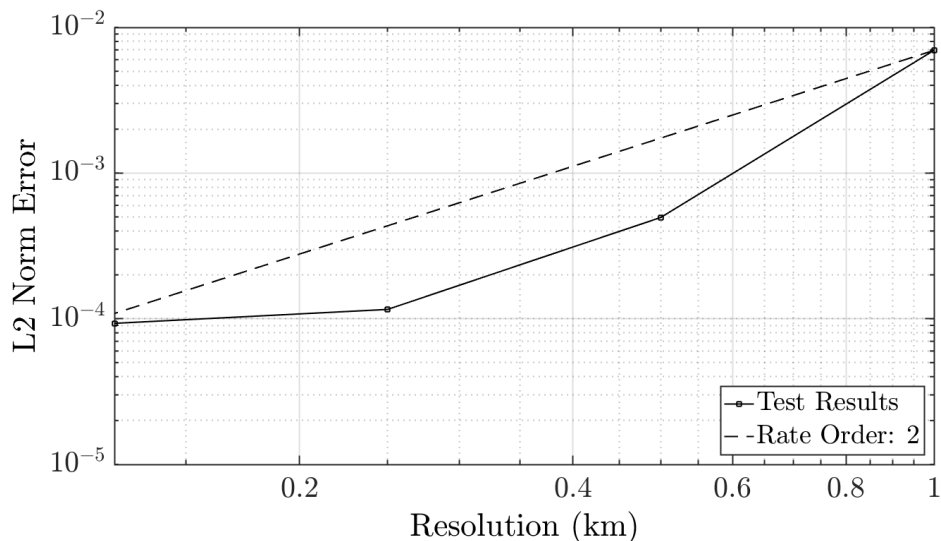


FIGURE 3.6: L_2 error convergence of numerical integration with respect to the semi-analytical reference solution. 10 m terrain height. Vertical Momentum ($\text{kg m}^{-2} \text{s}^{-1}$).

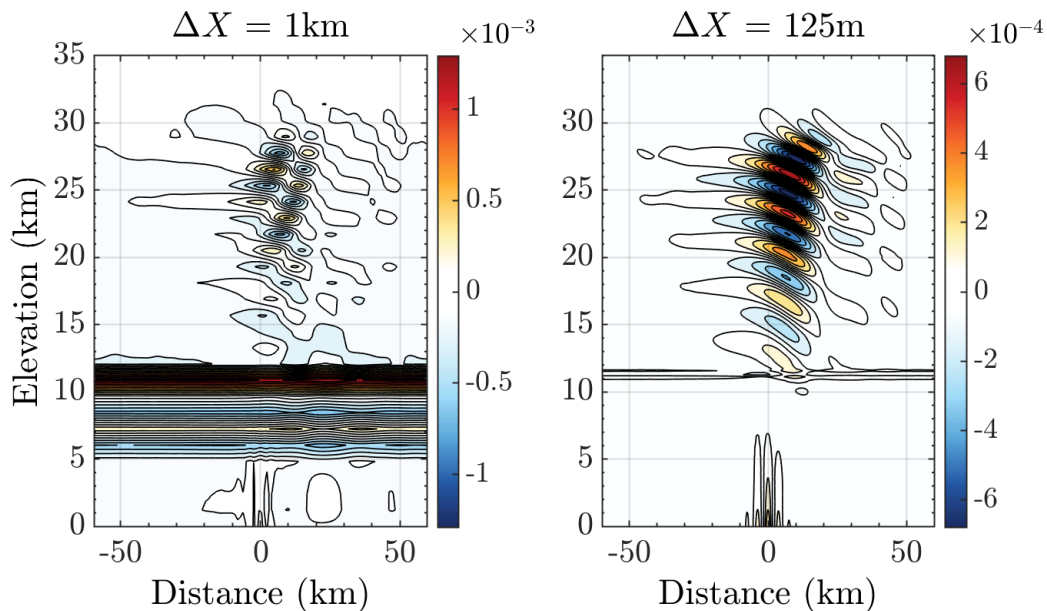


FIGURE 3.7: Difference in density for 3LAYER configuration with respect to simulation. Scaling set to show structure in the error fields. Density (kg m^{-3}).

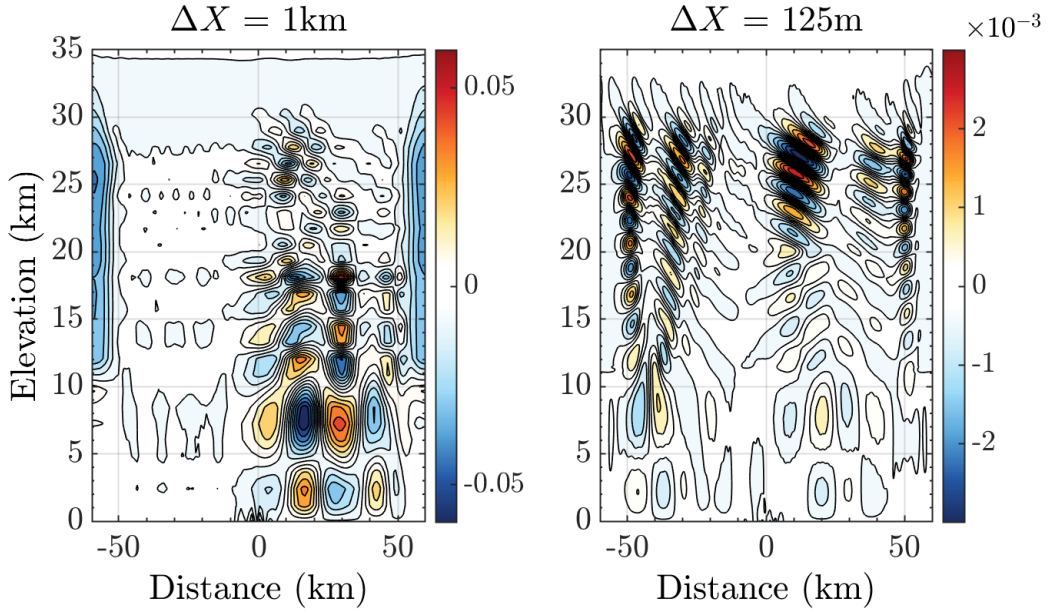


FIGURE 3.8: Numerical to reference solution difference. Scaling set to show structure in the error fields. Vertical Velocity difference (m s^{-1}).

the root cause of spurious reflection can only be remedied by increasing resolution, artificially smoothing the background fields, and/or reverting to a lower order discretization.

3.5.1 Diagnostic instability parameters

We seek to understand the onset of shear and convective instabilities in our tests in order to predict when and where our simulations will exhibit wave breaking. We use our reference solution to make a prediction of wave instability with varying mountain height as the primary parameter and consider all other initialization parameters to determine a particular test case. The first stability metric we consider is the local Richardson number computed as,

$$Ri = \mathcal{N}^2 \left(\sigma \frac{\partial u}{\partial \xi} \right)^{-2} = g_c \left(\sigma \frac{\partial \ln \rho}{\partial \xi} \right) \left(\sigma \frac{\partial u}{\partial \xi} \right)^{-2} = \frac{g_c}{\sigma} \left(\frac{\partial \ln \rho}{\partial \xi} \right) \left(\frac{\partial u}{\partial \xi} \right)^{-2} \quad (3.35)$$

The linear theory of instability for stratified shear flows as outlined by Nappo (2012) originally given by Miles (1961) and Howard (1961) states that a necessary (but not sufficient) condition for

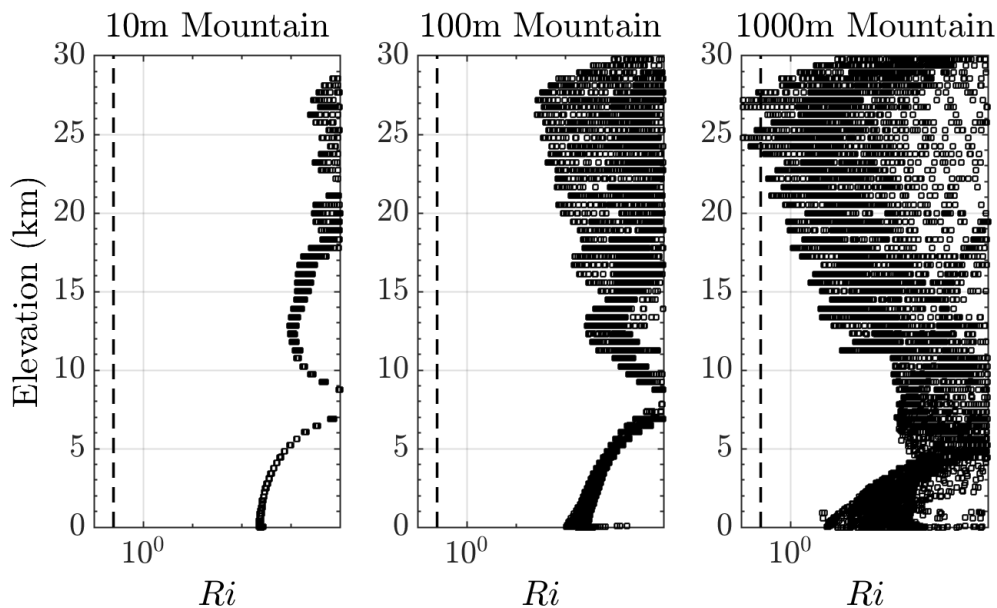


FIGURE 3.9: Local Richardson number and convective stability parameter for 3LAYER configuration. Reference solution with 10, 100 and 1000 m mountains from top to bottom. Fields plotted in the vertical axis only to show vertical structure. Dashed line indicates $Ri = 0.25$.

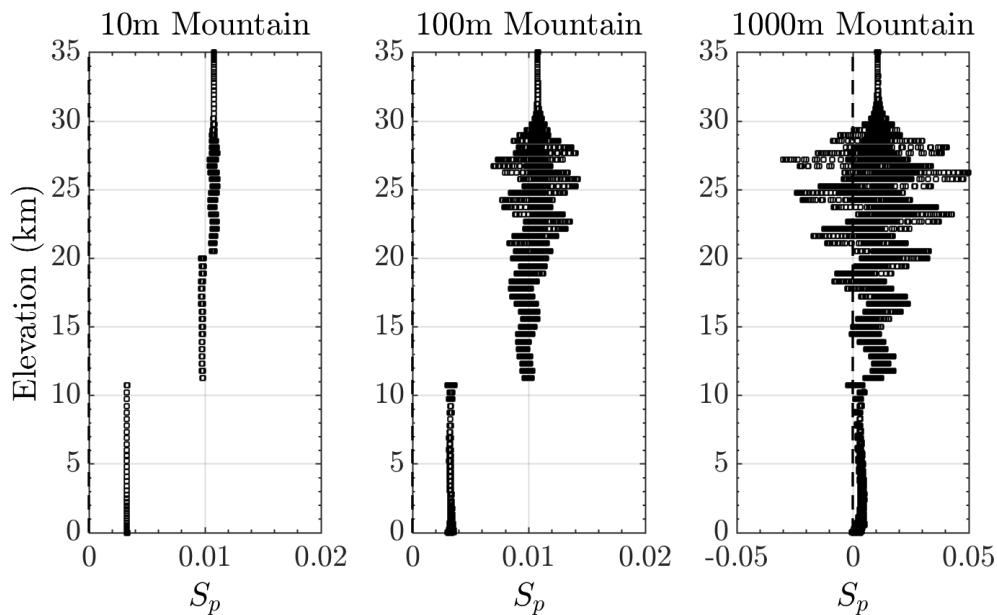


FIGURE 3.10: Convective stability parameter for 3LAYER configuration. Reference solution with 10, 100 and 1000 m mountains from top to bottom. Fields plotted in the vertical axis only to show vertical structure.

instability is $Ri < 0.25$. We note that Ri may be sensitive to accuracy in the estimate of local shear in a numerical model i.e. the discrete vertical derivative, since that factor is squared in (3.35). As waves propagate vertically throughout the flow, the minimum value of the local Ri number decreases with increasing terrain elevation as shown in figure (3.9) where the mean condition is shown in red. For mountain heights near the instability limit, the Ri number decreases exponentially with elevation particularly throughout the tropopause and lower stratosphere.

A second mode of instability corresponds to convective overturning. The condition for convective instability is stated as follows:

$$\frac{T}{\theta} \frac{\partial \theta}{\partial z} = T\sigma \frac{\partial \ln \theta}{\partial \xi} < 0.0 \quad (3.36)$$

The linear model predicts that instabilities may develop in layers above the jet maximum. Figure 3.9 shows that shear and convective stability under stratification is strongly dependent on terrain height and consequently initial wave amplitude. We note that convective instability tends to precede shear instability as a function of mountain height as shown in figure 3.10. We observe that convective instability is confined to discrete unstable layers bounded from above and below by very stable air. Therefore, we conclude that unstable convection is the primary mode of wave breaking followed (in elevation) by localized regions where shear instabilities will occur. Our linear model predicts the onset of convection at 11 km, in the 3LAYER test, with subsequent unstable layers at 18, 21, 24, and 27 km.

3.6 Nonlinear wave breaking simulations

The results from previous sections are now leveraged to set up numerical experiments to study dynamics of wave breaking. We simply raise the terrain height to 1 km sufficient to induce breaking at a level adequately below the absorption layer. It is important to note that an explicit dissipation closure is needed in order to carry out this simulation. Without rigorous justification, but in agreement with validation experiments done by Guerra and Ullrich (2016) at similar resolutions,

Chapter 3. Linear Reference Model

we choose 4th order hyperdiffusion operators both vertical and horizontal. The coefficients are constant in the horizontal and velocity weighted in the vertical. This closure model is stable and “scale selective” in the sense that structures are preserved near the grid scale.

Simulation results, shown in figure and (3.11), suggest several important flow features:

1. Breaking is displaced downstream of the primary obstacle. We made no assumption about waves being predominantly hydrostatic, therefore we expect this displacement as a consequence of non-hydrostatic effects in the initial wave train.
2. The largest eddies resolved are approximately of the same size as a vertical wavelength. This observation has implications on whether the wave structure of a flow is maintained and under what conditions it is reasonable to assume so.
3. Wave breaking generates a turbulent wake that extends far downstream of the obstacle. In fact, our simulations suggest that these regions may be as long as the several times the size of the domain (100 to 200 km). This implies that regions of wave dissipation, and thus momentum exchange, are much broader than regions immediately above a mountain.
4. Figure 3.11 (right panel) shows that the linear prediction for the lowest unstable layer in the 3LAYER configuration is quite good at approximately 12 km elevation.

3.7 Conclusions

We present a semi-analytical, high fidelity solution to the linearized non-rotating Euler equations in the vertical plane. Our solution is closely related to classical transform methods with a specific choice of expansion by Hermite functions in the horizontal and Lagrange polynomials in the vertical. While the resulting dense derivative operator matrices are impractical in a true computational setting, we exploit sufficient sparsity in the final operator to compute a solution efficiently. The result is highly accurate and ideally suited to cross mountain flows over Cartesian domains of 100

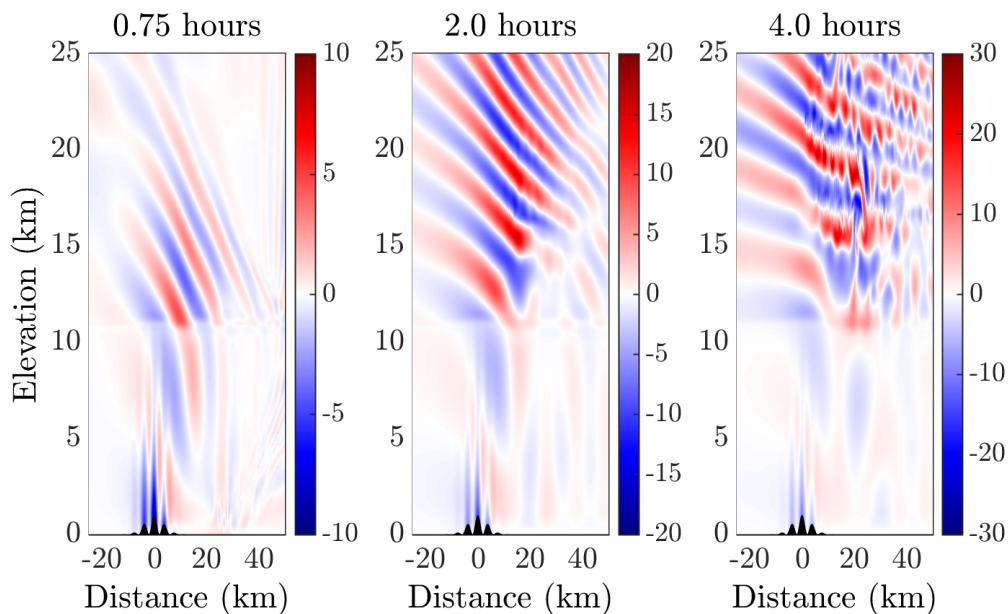


FIGURE 3.11: Wave breaking in the 3LAYER configuration. Potential temperature deviation (K) field shown.

to 200 km in total length. An important limitation to the use of the Hermite function expansion is that all partial derivatives in x become dense matrix operators. For larger domains, a more traditional Fourier expansion of said derivatives may be employed making the solution process much more efficient. However, the Fourier solution excludes the use of lateral absorption layers and often requires a larger domain than necessary in order to account for the natural periodic boundary condition especially in the presence of trapped waves that persist far downstream of the mountain.

The objective is to use the linear reference solution to design numerical experiments in the context of steady 2D mountain waves. This reference may then be used to validate fully non-linear solutions run on general purpose dynamical cores. The classical theory of linear mountain waves provides a variety of solutions under very specific conditions which are only qualitatively useful when assessing the performance of a numerical model. Our linear model, how is able to incorporate more general background conditions without hydrostatic or incompressible/Boussinesq

Chapter 3. Linear Reference Model

approximations. Furthermore, we include the use of Rayleigh absorption layers used to approximate radiation (top) and inflow/outflow (lateral) boundary conditions.

The dynamical core Tempest achieves a steady equilibrium via a long term (15 hours) integration. When comparing the simulations to our reference solution we find there is an error floor in spatial convergence for a given forcing amplitude. We attribute this finite error to a fundamental difference between the linear and non-linear equilibrium solutions and quantify it by evaluating the residual of the inviscid Euler equations using the linear solution interpreted as the first iteration in Newton's Method. Our linear reference solution allows for direct validation of numerical results from nonlinear models including error estimates for any mountain height. We do not attempt to carry out the full Newton iteration, but instead use the linear solution as an economical reference solution in the validation of numerical tests at quasi-steady state.

With the relationship between the linear model and non-linear simulations established, we design wave breaking simulations by performing parameter search iterations in the linear model only. Thus, we can establish background flow, boundary, and forcing conditions efficiently prior to running expensive batch simulations. This benefit increases greatly when the model/simulations are extended to 3D, especially for quasi-steady solutions requiring long integration times. The result is a series of simulations where the transitions from wave-like to turbulent flow can be studied in a systematic manner at reduced expense.

Chapter 4

An Assessment of the Lindzen/McFarlane Orographic Gravity Wave Drag Parameterization at Non-hydrostatic Scale

4.1 Introduction

The linear theory of orographically forced mountain waves (Smith (1979), Eliassen and Palm (1960), Klemp and Lilly (1975), Bretherton (1969a), Lindzen (1981), McFarlane (1987), and many others) introduced important results that allowed for robust sub-grid simulation of non-linear momentum drag imposed by breaking waves in the atmosphere. If we consider atmospheric flow over rough terrain with obstacles at every scale from synoptic (100 km) to cloud resolving (100 m), then momentum transfer to the ground may be characterized by a single aggregate drag coefficient, of which, breaking waves in the free stratified atmosphere is only one component (Garratt, 1977). This orographic gravity wave drag (OGWD) is known to be an important small to large scale phenomenon necessary for all studies of the general circulation including climate prediction.

The parameterization of orographic wave drag begins with linear constant-coefficient, plane wave solutions to the Boussinesq, hydrostatic, Euler equations in a vertical slice. These solutions provide estimates for the surface drag force due to terrain obstacles, amplitude change with elevation for waves predicted to propagate vertically, and for criteria giving the necessary conditions leading to unstable breakdown of waves. In the linear model, wave stress or correlated momentum flux is constant with elevation, but it is the divergence of wave stress with elevation that imparts a change in momentum as consequence of non-linear dissipative processes. Therefore, the parameterization of McFarlane (1987) imposes two conditions: unstable breakdown is due to convective motion i.e. vertical gradient of potential temperature is negative, and wave amplitude is limited to the value where instability begins. As the wave is maintained at “saturation” through a dissipation layer, stress is proportionately reduced. Each column of the parent numerical model grid is then forced where divergence of stress is non-zero. Operational models have employed such parameterized drag successfully over several decades. However, as modeling systems approach grid scales (locally or uniformly) where the hydrostatic approximation is no longer valid, it is necessary to closely evaluate the performance of physics parameterizations originally formulated in the hydrostatic context. In this work we perform such a re-evaluation of the OGWD

Chapter 4. OGWD Parameterization Assessment

parameterization currently operational in the Community Atmosphere Model (Neale et al., 2010) using high fidelity limited area experiments over scales down to 100 m.

High resolution studies, relative to what is typically used in general circulation models, have been performed under idealized conditions and for comparison against observational campaigns. For example, Broad (1996) made numerical integrations with grid lengths of 1 km resulting in good agreement with observations from the PYREX experiment cited in that work. Similarly, Bacmeister and Schoeberl (1989) shows several numerical experiments in constant background flow over a range of ridge heights demonstrating some of the characteristics of wave breaking that diverge from assumptions typically made based on the linear theory and wave amplitude saturation during breaking events. In particular Bacmeister and Schoeberl (1989) points out the presence of waves generated from turbulent regions that propagate downward contributing to transient episodes similar to what is observed in this work. However, as we will show, this resolution is insufficient to truly resolve the fine structure of turbulence generated by mountain breaking. Also, while some effort has gone into incorporating 3D aspects of cross mountain flow, we restrict ourselves to a 2D vertical slice so as to maintain reasonable run times as we perform our simulations at 100 and 200 m uniform resolutions.

In this paper, we study the parameterization using input flow fields generated using a high resolution numerical model Tempest. Tempest is designed to solve the dry non-hydrostatic equations in terrain-following height coordinates (Guerra and Ullrich, 2016) and stands as a limited-area proxy for a next generation non-hydrostatic extension of the finite element dynamical core in the Community Atmosphere Model. We explore the effect of varying levels of terrain filtering on flow response at high (200 m) resolution where we find little to no influence of higher frequency forcing components on predicted drag. Our results show that broad scale terrain features of sufficient height induce very similar turbulent flow fields if the virtual atmosphere is fine enough to support such a flow. Consequently, a smoothed-out terrain profile will produce nearly identical drag forcing in the free atmosphere as will a full terrain spectrum.

We further explore coarser resolutions, in both forcing and grid, of 1, 5, and 25 km. This is

precisely the resolution range recognized as the transition from hydrostatic to non-hydrostatic flow and which will come into operational use in the coming years. Our results show that, for an atmosphere with finite shearing and realistic stratification, model resolution at these scales does not support wave breakdown and produces a quasi-steady flow field without dissipation or internal drag forcing. Furthermore, the parameterization does not produce vertically propagating wave modes for forcing components in this same resolution range giving a null contribution. The result is that no drag is predicted under these conditions.

We conclude that model resolution is needed in regions of steep terrain variation, not only to capture the complete forcing spectrum, but primarily to set up a virtual atmosphere capable of reproducing the necessary turbulent cascade of energy needed to capture non-linear drag forcing. Advanced parameterization schemes for low level (close to terrain where Surface Layer theory is applicable) already exist and are being developed, (Lott and Miller, 1997; Beljaars, Brown, and Wood, 2004) but a comprehensive gravity wave breaking parameterization in the free atmosphere has not been attained as pointed out by (Teixeira, 2014) where many transient and nonlinear effects have yet to be accounted for in a concise manner.

The remainder of this paper is organized as follows: In section 4.2 we summarize the drag parameterization of McFarlane (1987) and how we implement it in this study. In section 4.3 we outline the methodology for processing high resolution terrain data to generate input profiles for both tests and parameterization. In section 4.4 we design our numerical experiments and make preliminary predictions based on a linear steady model. Then in section 4.5 we present our results. Discussion and conclusions follow in section 4.6.

4.2 Lindzen/McFarlane wave drag parameterization

4.2.1 Formulation

We follow the formulation of the sub-grid orographic drag parameterization given by McFarlane (1987) and currently implemented in the Community Atmosphere Model physics package

(Neale et al., 2010). We summarize the formulation by considering the steady Euler equations in a vertical slice under anelastic and hydrostatic approximations given as,

$$\begin{aligned} -\bar{U} \frac{\partial}{\partial x} \left[\frac{1}{\bar{\rho}} \frac{\partial}{\partial z} (\bar{\rho} \bar{U} \psi) \right] + \bar{U} \frac{\partial \bar{U}}{\partial z} \frac{\partial \psi}{\partial x} + \frac{\partial \Pi}{\partial x} &= 0 \\ \frac{\partial \Pi}{\partial z} + g_c \psi \frac{\partial \ln \bar{\theta}}{\partial z} &= 0 \end{aligned}$$

where ψ is the streamline displacement function (which has been used to eliminate the continuity and thermodynamic equations), Π is the Exner function, and all overbar quantities are zonally symmetric and in hydrostatic balance. Assuming a purely sinusoidal, monochromatic ridge profile, the following 2^{nd} order equation results,

$$\frac{\partial}{\partial z} \left[\frac{\bar{U}^2}{\bar{\rho}} \frac{\partial}{\partial z} (\bar{\rho} \psi) \right] + \mathcal{N}^2 \psi = 0 \quad (4.1)$$

where \mathcal{N} is the mean Brunt-Väisälä frequency defined as,

$$\mathcal{N}^2 = g_c \frac{\partial \ln \bar{\theta}}{\partial z} \quad (4.2)$$

The formulation then proceeds to find approximate solutions to (4.1). Background quantities are assumed to vary “slowly” relative to wave field variations. The assumed solution for the streamline displacement is,

$$\psi(z, x) = A(z) \cos \left[\mu x + \int_0^z \phi(z') dz' \right] \quad (4.3)$$

where A is an amplitude, and ϕ is a phase function both only dependent on elevation.

A consequence is that the primary growing mode in the solution (4.3) is assumed to vary at the characteristic length for background fields. Most importantly, wave amplitude grows as the inverse of mean density. Thus, further neglecting any 2^{nd} order terms when (4.3) is substituted

into (4.1) we may define a source level stress and amplitude function,

$$\tau_0 \approx -\frac{\mu h^2}{2} \bar{\rho}_0 \mathcal{N}_0 \bar{U}_0 \quad A(z) = h \frac{\bar{\rho}_0 \mathcal{N}_0 \bar{U}_0}{\bar{\rho} \mathcal{N} \bar{U}} \quad (4.4)$$

where the 0 subscript indicates a quantity evaluated at the ground $z = 0$ for an inviscid model with free-slip lower boundary, and μ is the spatial frequency related to terrain feature length by,

$$\lambda = \frac{2\pi}{\mu} \ll \frac{\mathcal{N}}{U} \quad (4.5)$$

for representative values of the BV frequency and mean wind typically chosen near the ground.

The quantities given by (4.4) provide a source stress as a function of low level wind and a vertical amplification factor that scales with the inverse of background density. We note that we use boundary values for all quantities with 0 subscript due to the free-slip condition. This will differ from models where a boundary layer is possible in which case source quantities are taken as integrated averages over some arbitrary height from the surface; typically on the order of terrain height (Neale et al., 2010). The condition given by (4.5) then states the range of wavelengths that will excite propagating modes in the hydrostatic model used here. Therefore, the value(s) of λ are restricted and must be chosen as the union of the set defined by the condition (4.5) and wavelengths that are excluded after filtering the input spectrum as we discuss in section 4.3.2. We will see that this becomes a second mechanism through which the parameterization shuts off and places a significant restriction on its use.

If propagating waves amplify with height, then at some finite elevation convective overturning will occur as a result of deformation in the potential temperature field. To capture this phenomenon, McFarlane (1987) makes use of what is known as the “saturation hypothesis” (Lindzen, 1981; Holton, 1982) by which waves are assumed to be amplitude-limited by diffusive transfers of heat and momentum upon wave breaking. In the linear regime, stress is constant in the column resulting in amplification, but upon breaking, amplification becomes constant and a decrease in stress

is necessary to account for energy dissipated in the process of turbulent breakdown.

In the saturation region, where diffusive transport is taking place, the amplitude function takes the form,

$$A(z) = \frac{\bar{U}}{\mathcal{N}}. \quad (4.6)$$

where it becomes clear that waves are always assumed to propagate in stable stratified layers with nonzero positive \mathcal{N} even in regions where dissipation is taking place. Critical layers are captured by imposing that wave amplitude vanish when background flow vanishes.

And the decrease in stress throughout the dissipation layer takes the form,

$$\tau(z) = \tau_0 \left(\frac{A(z)}{A_0} \right)^2 \frac{\bar{\rho} \mathcal{N} \bar{U}}{\bar{\rho}_0 \mathcal{N}_0 \bar{U}_0}. \quad (4.7)$$

A dissipation layer ends when wave amplitude falls below the value in (4.6) where the given stress in (4.7) is then carried conservatively with growing amplitude (4.5) until breaking occurs again at some higher elevation.

4.2.2 Implementation

Ultimately, the goal of the OGWD parameterization is to impose a vertical stress to the resolved momentum equations in the following form,

$$\frac{\partial u}{\partial t} = -\frac{1}{\bar{\rho}} \frac{\partial \tau(z)}{\partial z} \quad (4.8)$$

where u is the component of the resolved component of velocity that is aligned to the cross-mountain direction. The profile $\tau(z)$ is the vertical profile found by evaluating (4.7) in a given column.

In the linear formulation above, this wind is the mean/background wind while in a 3D simulation, this is the total wind magnitude at the base of the given grid column assumed to be fully

Chapter 4. OGWD Parameterization Assessment

directed onto the sub-grid orography. Therefore, a standing wave train develops in a medium made up of the numerically resolved wind/thermodynamic field. Given our objective is to investigate how the parameterization performs as we approach input wavelengths that no longer support propagation, include a transition into the non-hydrostatic regime, and may give rise to features of fully resolved wave breaking we restrict its implementation to time-averaged input fields under the assumption and requirement that our simulations approximate quasi-steady turbulent states such that time averaging is reasonably well justified.

Thus, we do not apply the parameterization output in feedback with the dynamical model. In general, a full implementation requires careful tuning of time step between the dynamics and physics update and this lies beyond the scope of our present work and we focus on the right hand side of (4.8) where the vertical gradient of stress is defined. This simplification will be sufficient for our assessment and reflects an emphasis on structure of the simulated flow field as it relates to assumptions inherent in the parameterization formulation. This study will then inform the requirements for a next-generation OGWD parameterization and associated high-resolution modeling efforts, as global models are pushed towards non-hydrostatic scales.

4.3 Methodology

In order to assess the performance of the Lindzen/McFarlane wave drag parameterization we begin with a method of processing available terrain data to construct two inputs: 2D filtered height profiles as the lower boundary for limited area high-resolution experiments, and corresponding standard deviation values from the filtered mean profile as per-column input to the parameterization code. Filtering is performed using a simple moving average applied to the raw data which differs from what is available to users of the Community Earth System Model as outlined by Lauritzen et al. (2015) where propagating/non-propagating scale separation is assumed and a spectral filter is used. In the global context, spectral filtering is much more accurate, however in our tests

the moving average filter combined with appropriate processing is sufficient to investigate the effects of such coarsening on atmospheric response at resolutions below 1 km. Due to the relatively high resolution of our data, the moving average filter is also preferable since it is monotonic and does not cause spurious oscillations typical of spectral filters.

4.3.1 Elevation of the Tropical Andes

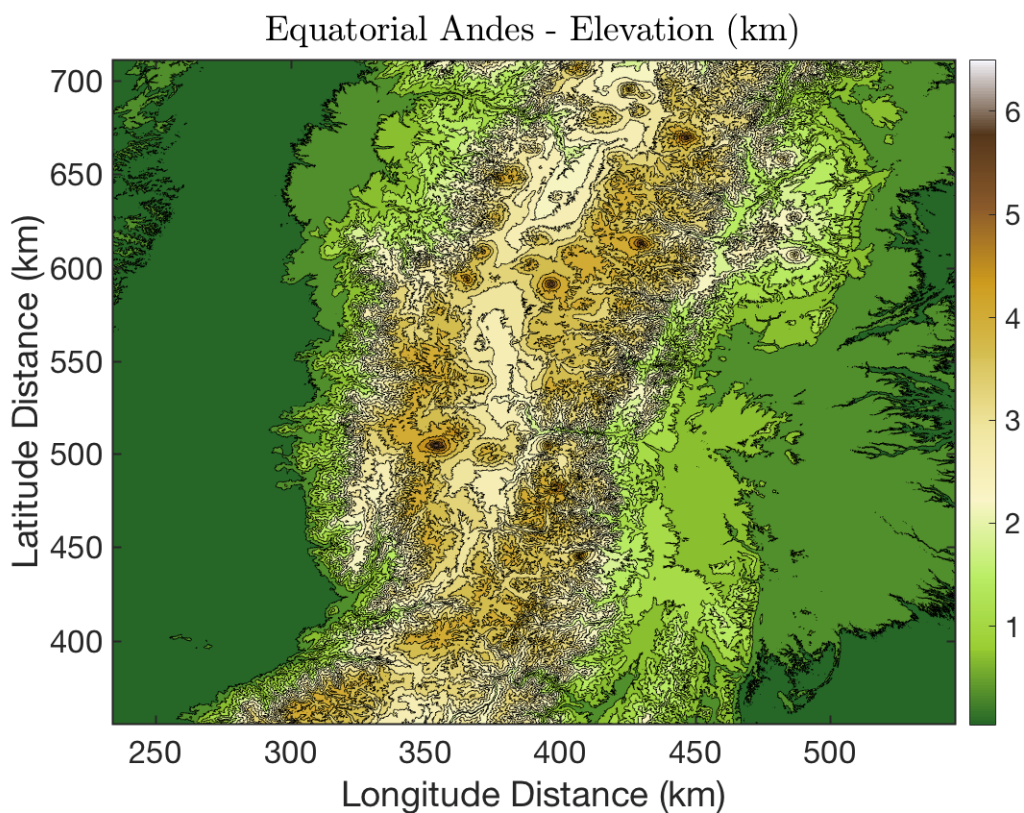


FIGURE 4.1: Digital elevation map of the equatorial Andes. Height in km. Domain distances are specified relative to the South West corner of the data map at 82° West and 6° South.

The bottom boundary is taken as an East-West section of the tropical Andes of Ecuador at a normalized peak elevation of 1 km. A smooth and complete digital elevation map (800×800 km area), at 30 m resolution, of the country of Ecuador was provided to the author by the “Instituto

Geográfico Militar del Ecuador” (IGM) as a matter of public record with the express permission to apply these data to atmospheric modeling studies (Jimenez, 2017). Selected profiles are analyzed with standard signal processing techniques and applied directly to our terrain following model.

A sample contour of the terrain data is shown in fig. 4.1. The data is meticulously constructed at a resolution of 30 m, is relatively compact (on the order of several hundred megabytes) and is therefore well suited to spectral analysis and as a source of orographic forcing profiles in simulations.

4.3.2 Terrain filtering and analysis

The current work is limited to a 2D vertical slice model and a single representative terrain profile for all simulations. We make these choices to constrain computational overhead (from 3D simulations), and to simplify our subsequent analysis of results with respect to the drag parameterization. We find that it is sufficient to examine longitude-height fields as the parameterization is originally formulated in 2D and implemented in models by projecting wind components into the cross mountain direction. We expect the vertical structure of wave trains and turbulent layers well above the terrain to be consistently reproduced in 2D simulations for the purpose of the present work.

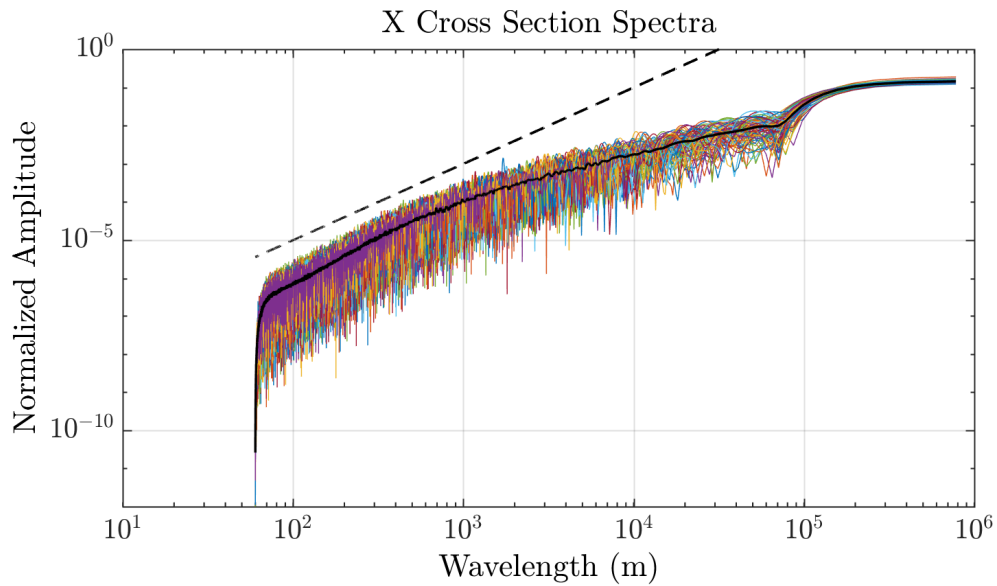


FIGURE 4.2: The normalized amplitude spectra for all horizontal cross sections as a function of wavelength (in m). The dark black line denotes the average spectrum for longitudinal cross sections. Dotted black line corresponds to the k^{-2} decay law.

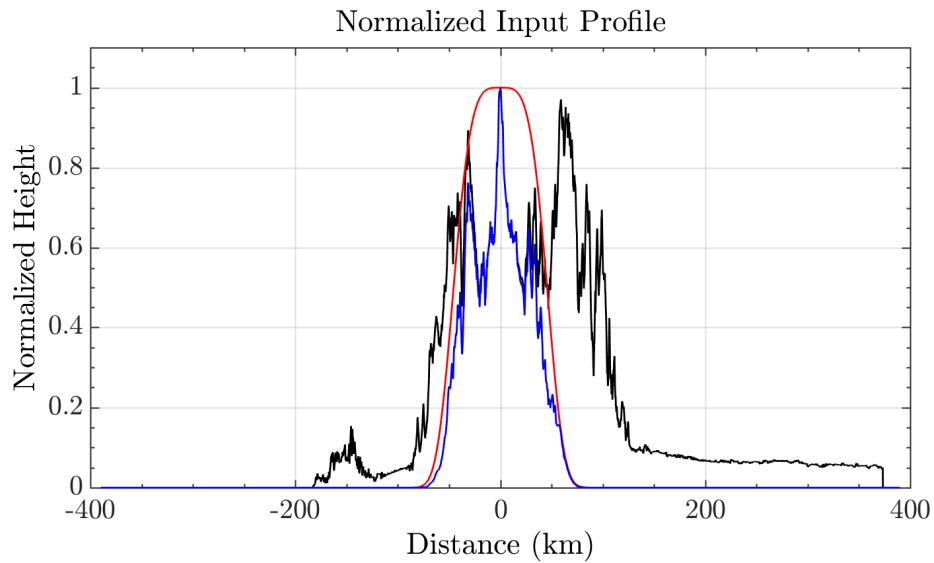


FIGURE 4.3: Input terrain profile processing. Black curve denotes the circularly shifted data, red curve is the 4th order Gaussian windowing function, and in blue is the resulting input profile. Height is normalized to unity.

We consider the amplitude spectra of all possible cross sections from the original data as shown in fig. 4.2. We observe a tight clustering with respect to the solid black ensemble mean spectrum. Departures, in any one cross section, from the mean in fig. 4.2 are at most 1%. With this result we proceed to conduct our numerical experiments by choosing a single representative profile shown in fig. 4.3 with a pre-processing detailed in Appendix B. While we note a significant difference in the spatial domain, spectral characteristics are maintained. Careful consideration has been taken to construct simulations that have sufficient overall length while supporting a representative sample of the topography without leading to prohibitive computational costs.

Given the input profile in fig. 4.3, its spectral characteristics after the application of progressively wider filters is shown in fig. 4.4 and for variance from filtered output in fig. 4.5. We observe close correspondence with findings from other data sets presented in Lauritzen et al. (2015) and Gagnon, Lovejoy, and Schertzer (2006) where spectral decay power law of -2 to short wavelength was found. fig. 4.4 we see attenuation at small wavelengths of approximately an order of magnitude for each filter width. Figure 4.5 shows variance from the moving-average filtered data. Each spectrum has a cut-off wavelength manifested as a global maximum to the left of which are terrain components excluded from the resulting profile. We observe significant decay in the amplitude spectra in fig. 4.5 with decreasing filter width showing that longwave components have much greater amplitude than shortwave terrain features as expected. Lastly, based on the variance, we compute the standard deviation as source input to the parameterization at a point (column base) along the profile as,

$$\sigma_h = \sqrt{\frac{1}{2N} \sum_{i=-N}^{i+N} (h_i - \bar{h})^2}$$

where N , h , and \bar{h} are as defined in (B.10).

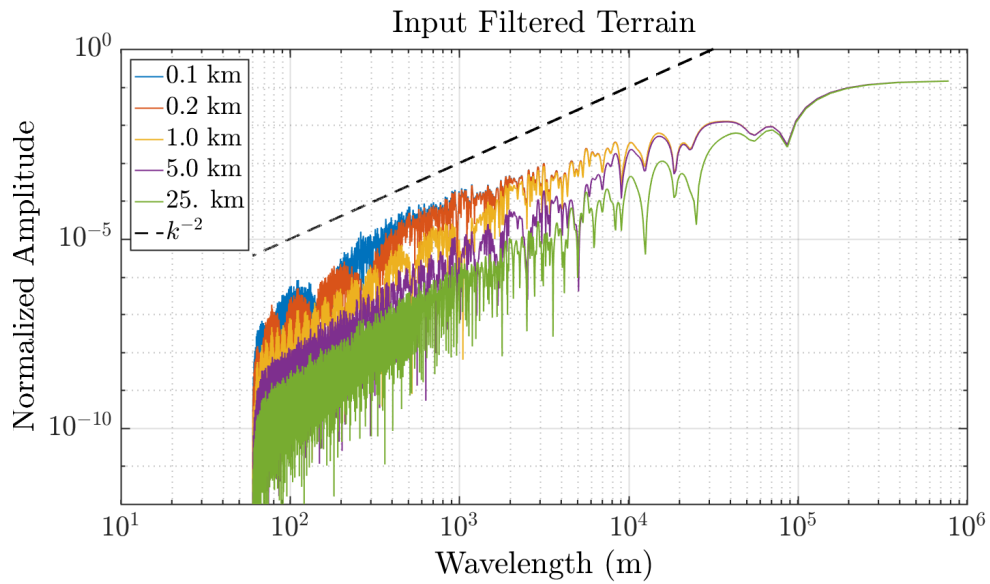


FIGURE 4.4: The input terrain normalized amplitude spectra. Filter widths are 0.1 km (blue), 0.2 km (orange), 1.0 km (yellow), 5.0 km (purple), 25.0 km (green).

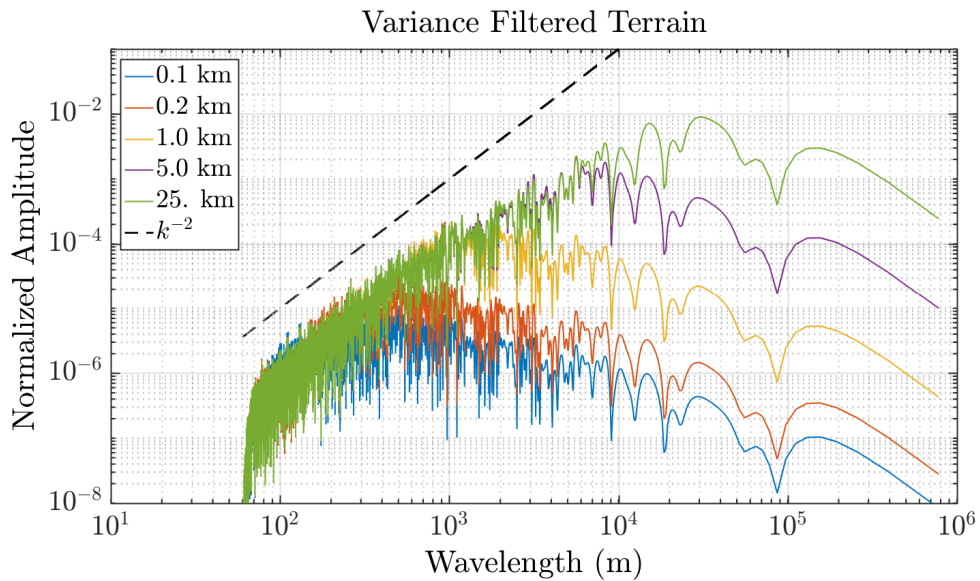


FIGURE 4.5: The input terrain normalized amplitude spectra. Filter widths are 0.1 km (blue), 0.2 km (orange), 1.0 km (yellow), 5.0 km (purple), 25.0 km (green).

4.4 Numerical test design - 2D Wave breaking

We now describe the experiments designed for this study. Given the extent and height of the input terrain, our simulated domain is a Cartesian 2D vertical slice rectangle 500 km wide and 40 km deep. We pay close attention to sponge layers employed and attempt to minimize their thickness (influence) while providing an adequate approximate outflow condition. Lastly, our numerical model utilizes separate horizontal/vertical hyperviscosity operators (Guerra and Ullrich, 2016) as a means of adding the necessary stabilization while emphasizing fine scale structures.

Bacmeister and Schoeberl (1989) uses three nondimensional parameters to characterize different regimes in a limited area model. While our tests differ significantly in the use of realistic topography and variable stratification/wind profiles, the near surface conditions may be evaluated as,

$$\frac{\mathcal{N}h}{U} = 1.0, \quad \frac{\mathcal{N}L}{U} = 100.0, \quad \frac{\mathcal{N}H}{U} = 10.0, \quad (4.9)$$

where $h = 1000$ m, $L = 100$ km, $H = 10$ km, and $U = 10 \text{ ms}^{-1}$ at the terrain surface. We interpret the flow to be predominantly in the hydrostatic regime as is typical of the real atmosphere in such a situation given the overall extent of the domain and width of the tropical Andes, but we note that ridge width L and buoyancy scale height H are variable in our study according to the input spectrum of topography shown in section 4.2 and in the layered stratification profiles shown in fig. 4.6. Thus we expect that nonhydrostatic (for shorter terrain wavelengths) and density variation (for abrupt changes in stratification) effects will become important locally and will influence breaking in a realistic manner. Lastly, we drive the tendency for overturning by setting the mountain height h to a value that brings the Froude number close to unity.

4.4.1 Background atmospheric conditions

Numerical experiments are designed around a hydrostatically balanced atmosphere composed of three layers with constant lapse rate representing a troposphere, tropopause, and lower stratosphere. The background flow field is made up of a vertically sheared jet with peak amplitude at 8 km. Flow at the boundary is a constant 10 ms^{-1} wind applied along the bottom terrain surface. The initialization profiles are shown in fig. 4.6 where corresponding density and pressure profiles are given.

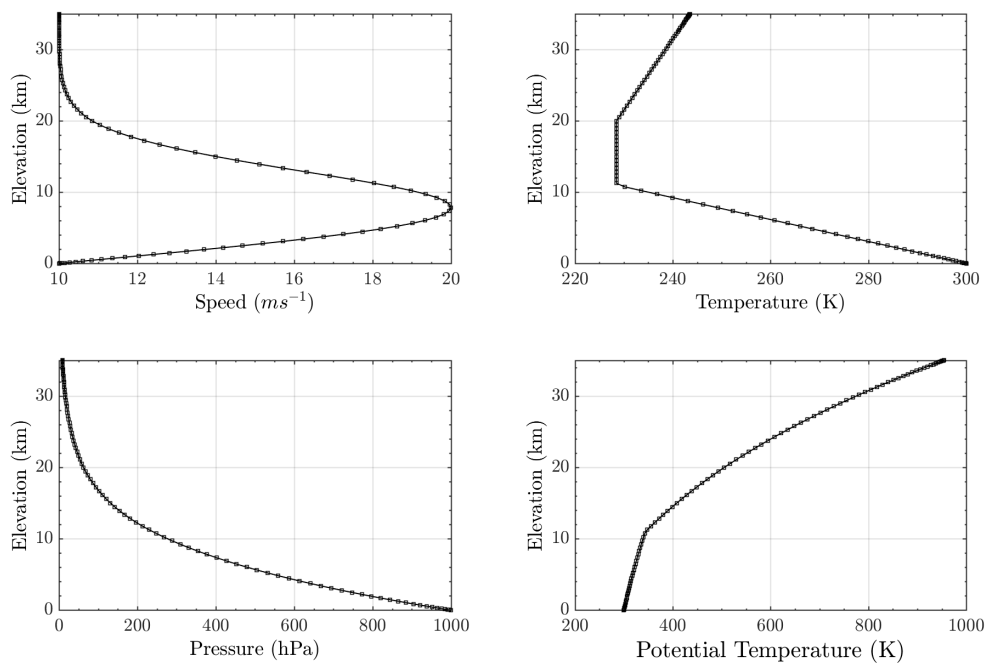


FIGURE 4.6: The background wind and thermodynamic profiles as a function of geometric height. Vertical profile and gradient details and parameters specified in Chapter 2.

The background state we have chosen is intended to represent a typical stable atmosphere with finite shear. As such, we expect evanescent and propagating waves refracted and reflected by shear and the prescribed discontinuous changes in temperature lapse rate. In particular, we expect significant trapping/ducting through the troposphere (elevations below 10 km).

4.4.2 Discrete setup and initialization

We consider a limited-area Cartesian domain in X-Z space such that $x \in [-200 \ 300]$ km and $z \in [0 \ 40]$ km with a peak height of 1000 m centered at $x = 0$. Figure 4.7 shows the initialization and control volume used to evaluate (4.13) in the region where wave breaking is expected. The equations are solved numerically using a 4th order spectral element method in the terrain following direction, the staggered (vertical velocity at boundaries) method of Guerra and Ullrich (2016) at 3rd order in the vertical, and integrated in time explicitly with a Strong Stability Preserving Runge-Kutta method of 3rd order. Horizontal (constant coefficient) and vertical (flow-weighted) hyperviscosity is employed again following Guerra and Ullrich (2016).

For nonlinear wave breaking simulations, the hyperviscosity operators, applied to all prognostic fields, serve as the subgrid closure model necessary for turbulent flows and have been used in previous numerical studies of stratified turbulence (Herring and Métais, 1989). As the operators involve fourth derivatives of the mean fields with anisotropic, time dependent coefficients, we do not define/analyze an equivalent eddy diffusivity, but limit our model be an analog for the use of a properly formulated turbulence closure scheme. However, we will see from the results, that hyperviscosity used in this manner maintains stability and preserves flow structures in a scale selective manner as desired.

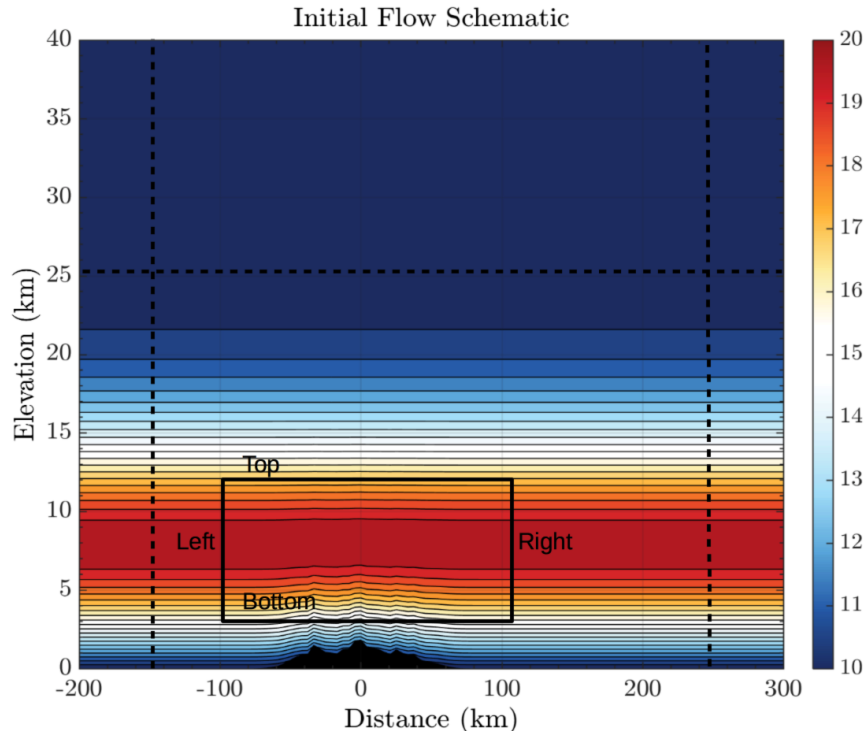


FIGURE 4.7: Schematic diagram of initial horizontal flow field and orographic forcing for numerical tests. Dashed black lines indicate the position of the sponge layers. The solid black rectangle shows a control volume boundary to evaluate net drag as given by (4.13). Terrain profile has been magnified for visualization in this figure.

Boundary conditions are such that flow at the terrain surface follows the bottom contour and vertical velocity vanishes at the model top. These conditions are augmented by top and lateral absorption layers 15 km deep, 40 km wide at the inflow (left) boundary, and 80 km wide on the outflow (right) boundary. The absorption layer parameters are found through an iterative process with the following criteria:

1. Minimize reflection artifacts from a semi-analytical linear solution to the given problem. Requires solving the steady linearized system about a background identical to the initialization prescribed to the model including absorption layers.

2. Using estimates from the linear solution, change the layer thickness and strength in order to attain stable long term (50 hours) solutions with minimal reflection transients.

All simulations fix a maximum peak height of 1000 m. This value is chosen as it is sufficiently large to allow for non-linear wave breaking, but is also sufficiently small so as to control the magnitude of impulsive transients that would require a larger domain and thicker absorption layers in order to achieve stable, smooth, long-term integrations at a reference resolution of 100 m.

4.4.3 Stratified turbulence metrics

In the interest of understanding the structure of turbulence generated by these waves, we compute the specific kinetic energy power spectra at several elevations, over the horizontal dimension. The objective is to characterize the vertical structure of confined turbulence we expect to find and determine how these layers constrain effective model resolution to values where the OGWD parameterization is completely ineffective. The horizontal and vertical components of specific kinetic energy are defined as,

$$\begin{aligned} KE_h &= \frac{1}{2}(u')^2, \\ KE_v &= \frac{1}{2}(w')^2. \end{aligned} \tag{4.10}$$

where u' and w' are the time fluctuating horizontal and vertical velocities defined as,

$$\begin{aligned} u' &= u(x, z, t) - \frac{1}{T} \int_{T_1}^{T_2} u(x, z, t) dt, \\ w' &= w(x, z, t) - \frac{1}{T} \int_{T_1}^{T_2} w(x, z, t) dt. \end{aligned} \tag{4.11}$$

and a time average from $T_1 = 10$ to $T_2 = 50$ hours has been removed from the numerical model output. Furthermore, we will consider only the vertical component of kinetic energy as defined in the second term on the right-hand-side of (4.10).

In our computations, model output is generated every 3 minutes. At each time level $t \in [T_1, T_2]$, we compute power spectral density of (4.10) as,

$$Q(k_x) = \frac{1}{N_x} |\mathcal{F}\mathcal{F}\mathcal{T}_x(q)|^2 \quad (4.12)$$

where q is the field being processed, N_x is the number of sample data points in the x direction, k_x is the spatial frequency, and $\mathcal{F}\mathcal{F}\mathcal{T}_x$ refers to the spatial Fast Fourier Transform of Cooley and Tukey (1965). Lastly, we compute the ensemble (time) average for all power spectra generated by (4.12) and present the result as a single set of spectra at various height levels.

4.4.4 Transient drag force comparison metrics

As depicted in fig. 4.7, our primary metric for comparison is the integrated net drag force in a given rectangular region of flow. We proceed by considering a static control volume spanning a rectangular region and computing the following boundary integral that emerges from conservation of linear momentum,

$$F_D(t) = \int_{-x_L}^{x_R} \rho u w|_{z_T} dx + \int_{-z_B}^{z_T} \rho u^2|_{x_R} dz - \int_{-x_L}^{x_R} \rho u w|_{z_B} dx - \int_{-z_B}^{z_T} \rho u^2|_{x_L} dz. \quad (4.13)$$

where ρ , u , and w are density, horizontal wind, and vertical wind respectively. The subscripts L , R , B , and T designate the Left, Right, Bottom, and Top of the control volume, giving the corresponding integration limits and the locations where each integrand is evaluated.

The definition of the drag force in (4.13) only takes into account changes in momentum flux and neglects any other external force contributions. This is consistent with an inherent assumption of the parameterization that forces are due to wave momentum flux divergence in the vertical

column. Furthermore, simulation output is not decomposed into mean/wave components but each field is evaluated completely into the integrands of (4.13).

4.4.5 Test configurations

With the use of a fully nonlinear unsteady numerical model we carry out the following two sets of numerical experiments:

1. Model resolution held at 200 m in the vertical and horizontal directions. Terrain forcing varies by moving average filter width at 0.2, 1.0, 5.0, and 25.0 km. Hereafter, this is referred to as the “FINE” configuration.
2. Both model resolution and terrain filtering vary at 0.2, 1.0, 5.0, and 25.0 km. Hereafter, this is referred to as the “COARSE” configuration.
3. Reference simulation with uniform resolution of 100 m in model grid and forcing filter width to study the spectral characteristics of the turbulence generated in our simulations.

For each configuration, a single flow field is generated as input to the drag parameterization code by computing a time average from 20 to 30 hours (using 3 minute outputs). Over this period, the flow is considered quasi-steady and fully developed without any initial transients. There is a significant difference in flow response at the reference 100 m resolution and the test configurations outlined above at 200 m. In section 4.5.2 we will show that, in the reference test, a broad instability develops in the background jet leading to strong vertical mixing manifested as a strong variation in net drag over regions spanning troposphere and tropopause layers. The unstable mode in the jet is transitory and persists from hour 20 to 35 in the simulations. In contrast, our test configurations do not exhibit this jet feature in the same time period as will be discussed in section 4.5.3. Thus, for the purpose of evaluating the parameterization, we will consider the time period $T \in [20, 30]$ hours to be at quasi-steady turbulent equilibrium and carry out averaging procedures for that record.

4.5 Results

In this section we present results starting with predictions of stability parameters: Richardson number, convective stability, and Froude number based on a linear steady model under the exact conditions of sections 4.4.2 and 4.4.1. We use these results to establish local length scaling for regions where unstable (nonlinear) wave breaking may be expected. We then show and discuss results from a high resolution (uniform 100 m) simulation with the goal of understanding qualitative structure and quantifying flow response in terms of mean drag forcing. Lastly we discuss numerical tests in the FINE and COARSE configurations, defined in section 4.4.5, and test the response of the Lindzen/McFarlane OGWD under these conditions.

4.5.1 Linear steady-state predictions

As part of the process for validating our numerical results, a linear steady state model for mountain waves in a 2D, Cartesian, non-rotating domain was developed. An application of the linear theory of mountain waves provides us with a first estimate for both vertical length scale as a function of wavenumber, and wave growth potentially leading to instability at a given elevation. As we are invoking a linearization of the equations, we restrict this portion of the analysis to a peak terrain height of 100 m. These estimates are important in determining the vertical resolution necessary to capture the wave train resulting in an upper bound for the grid necessary to then resolve any turbulent breakdown. This model is an extension of the classical linear theory (Nappo, 2012) (and references therein), where the linearized inviscid equations are solved using a collocated horizontally Hermite, vertically Lagrange expansion of solution fields. This approach is analogous to the use of discrete Fourier transforms to solve the constant coefficient Taylor-Goldstein equation, but allows for arbitrary variation in the coefficients i.e. no restriction on background atmospheric profiles is assumed. The goal is to produce fast solutions with terrain inputs of finite amplitude with initialization and boundary conditions equivalent to numerical tests and make predictions of wave instability regions prior to running costly, non-linear simulations. This model is described

Chapter 4. OGWD Parameterization Assessment

in Appendix B. The parameters of interest for determining instability are the Richardson number Ri and the static stability parameter S_p . These are defined by

$$Ri = \mathcal{N}^2 \left(\frac{\partial u}{\partial z} \right)^{-2} = g_c \left(\frac{\partial \ln \rho / \rho_0}{\partial z} \right) \left(\frac{\partial u}{\partial z} \right)^{-2}, \quad (4.14)$$

where u is the horizontal wind speed, ρ is density, and $g_c = 9.80616 \text{ ms}^{-2}$ is the gravitational constant, and

$$S_p = \frac{T}{\theta} \frac{\partial \theta}{\partial z} = T \frac{\partial \ln(\theta / \theta_0)}{\partial z} \text{ K m}^{-1} \quad (4.15)$$

where T , and θ are total dry sensible and potential temperature respectively. Density and potential temperature in (4.14) and (4.15) are normalized to surface reference values of $\rho_0 = 1.16 \text{ kg m}^{-3}$ and $\theta_0 = 300.0 \text{ K}$. Thus, the necessary condition for shear instability in a stratified environment is $Ri < 0.25$ while free convection occurs when $S_p < 0.0$ (Nappo, 2012). Both instability modes are known to be associated with topographically induced wave breaking. We will use the linear steady solution, under nearly identical initial and boundary conditions as the non-linear transient simulations, to estimate the vertical structure of unstable layers that may develop as the peak terrain height is increased to 1000 m. However limited to the linear regime, our solution incorporates variations in the background fields without approximation, does not neglect density perturbations, and is formulated in the terrain following system exactly matching what is done in the complete numerical model. Our objective is to bring the linear steady approximation as close as possible to the fully non-linear solution for input terrain of finite amplitude.

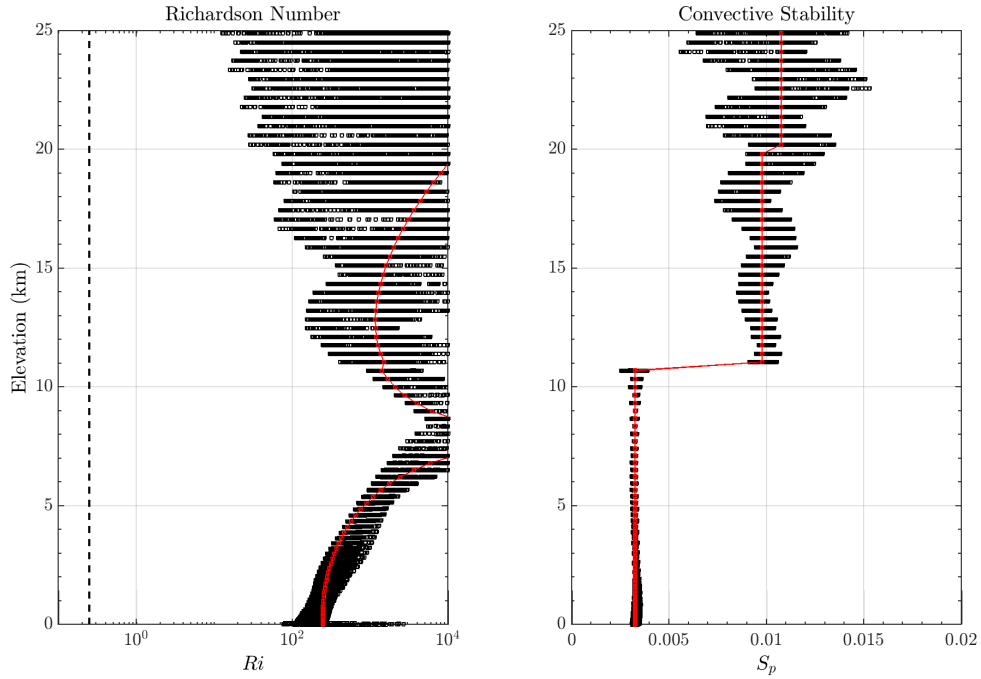


FIGURE 4.8: Vertical scatter plots of Richardson number (4.14) and convective stability (4.15) criteria computed from the linear solution with 1000 m peak terrain height. Dashed black lines indicate the stability thresholds. Markers corresponds to each grid value plotted by amplitude-Z. Red curves denote Ri and S_p evaluated with initial conditions.

We also evaluate a local estimate of the Froude number defined as,

$$Fr = \frac{2\pi|u|}{\mathcal{N}\ell_h} \quad (4.16)$$

where $|u|$ is the absolute value of the total horizontal velocity and $\ell_h = 5000\text{m}$. We employ a modified form of the definition for the Froude number (4.16) given by Riley and deBruynKops (2003). In particular, we use the total horizontal velocity from the linear solution in order to capture changes in Fr due to orographic waves. We also fix the vertical length scale to $\ell_h = 5000\text{m}$ as a representative estimate of vertical wavelength in the flow were turbulence is expected to occur. Figure 4.8 shows the two primary modes of instability as a function of elevation as predicted by a purely

linear solution. The pattern of oscillation above 10 km in figure 4.8 indicates that layers where convective overturning is likely ($S_p < 0.0$) will be trapped between increasingly stable air leading to turbulence that is vertically confined. In particular we note that convectively unstable layers are predicted by the linear solution to be 2 to 3 km deep alternating with strongly stratified layers above and below. Our estimate for the local Froude number shown in figure 4.9 is likewise consistent with instability modes in figure 4.8 in revealing alternating layers of potentially unstable air. The effect of the waves is to lower the Froude number below unity (particularly above 15 km) where we expect wave breaking turbulence to be significantly influenced by stratification.

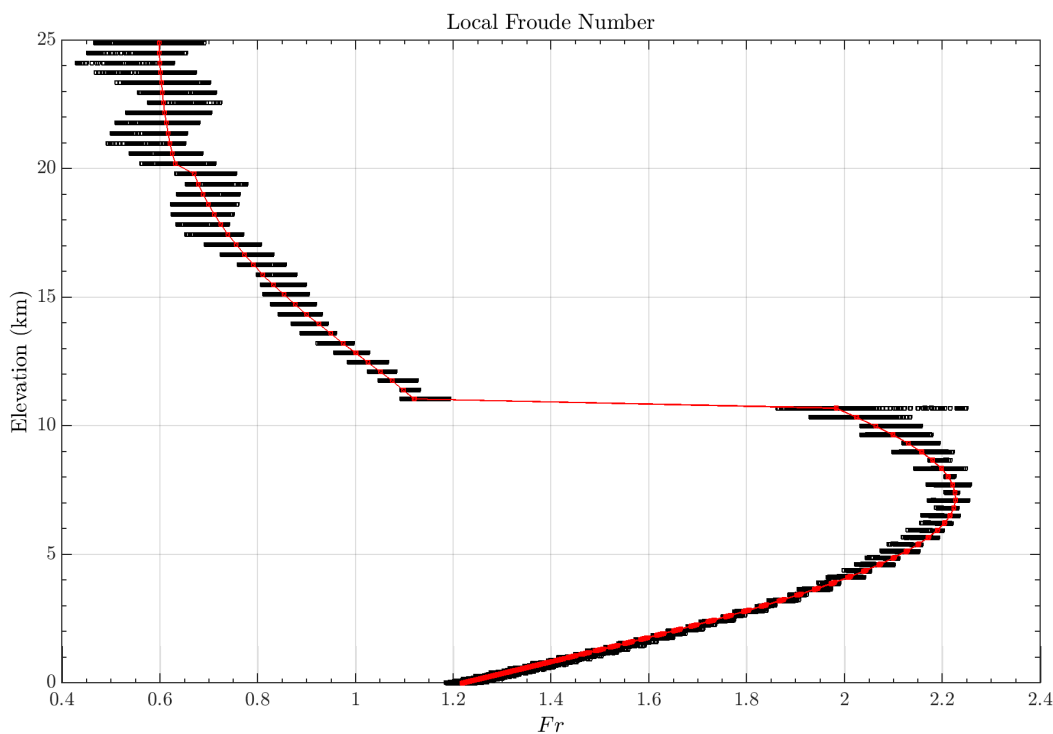


FIGURE 4.9: Vertical scatter plot of local Froude number from (4.16) computed from the linear solution with 100 m peak terrain height. The red curve indicates profile based on initial conditions. Markers corresponds to each grid value plotted by amplitude-Z.

Therefore, the linear model alone suggests a vertical model resolution much less than the depth

Chapter 4. OGWD Parameterization Assessment

of each unstable layer is required to sustain a truncated turbulent cascade within these alternating unstable layers. Given an effective model resolution assumed to be $4\Delta z$, then in order to resolve eddy features contained in the unstable layers of depth 2500m we estimate that a grid spacing of $\Delta z \leq 750\text{m}$ is necessary to model the wave breaking process explicitly.

The linear solution computed over the horizontal Fourier spectrum shows a generally variable vertical response as shown in figure 4.10. This is the analog to the dispersion relation derived from our linear solution admitting arbitrarily variable background fields. Thermodynamic and mass fields follow a similar behavior to horizontal velocity show limited response in the non-hydrostatic range of the input spectrum. Vertical velocity has a concentrated response, in terms of vertically propagating waves, for terrain features of 9 km in width indicating forcing in the non-hydrostatic regime. We observe from figure 4.10 that linear response in this atmosphere is greatly limited to input wavelengths near or greater than 10 km . This result indicates, that despite the rich continuous spectrum of inputs available (see figure 4.3) only a relatively narrow set of components project onto atmospheric response and supports the hypothesis that low level drag dynamics are decoupled from the contribution of breaking waves in the free atmosphere.

Chapter 4. OGWD Parameterization Assessment

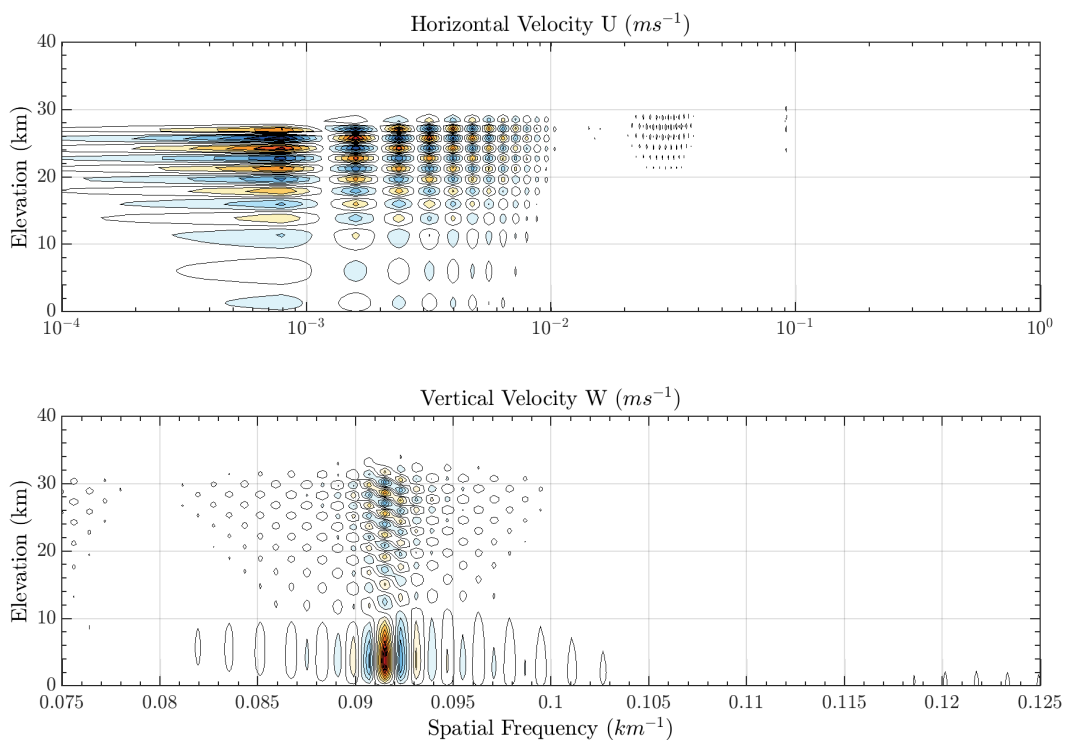


FIGURE 4.10: Linear solution frequency response map. Horizontal (top log axis) and vertical velocity (bottom linear axis) response as a function of horizontal spatial frequency k . Response amplitude is normalized to unity.

4.5.2 High-resolution reference

The reference solution is run at a uniform (vertical and horizontal) resolution of 100 m with a corresponding terrain filter window also set to 100 m. Figures 4.11 and 4.12 shows snapshots of the simulation just before and hours after the onset of turbulence in the model. We first see the initial impulsive disturbance as it propagates downstream and is consumed by lateral absorption layers as well as the height variable standing wave train that will eventually break locally. Horizontal velocity shows evidence of accelerated downslope winds at 14 hours with a subsequent low level reversal at 28 hours. There is also clear evidence of downward propagating waves in the tropospheric layer.

Chapter 4. OGWD Parameterization Assessment

A key feature of the turbulent flow is a wake that extends several hundred kilometers downstream of the terrain while maintaining a marked layered structure corresponding to the background environment. This wake is a mixture of wave-like and vortex flow where we will search for the presence of turbulent drag using (4.13) over distinct regions directly above and downstream of the mountains. This feature of our simulations is consistent with observations of highly anisotropic layered stratified turbulent flow as described by Billant and Chomaz (2001) and references therein from numerous numerical and physical experiments. As the flow develops further, we observe transient effects (upstream modes and evidence of downward waves caused by the primary breaking layer near 10 (km) elevation) that will give rise to changes in drag estimates.

If we consider that the OGWD model was designed to augment hydrostatic models, at a typical resolution of 100 km, then figure 4.11 shows that, remarkably, much of the turbulent field is indeed contained within a horizontal dimension of that size with perhaps some transient unstable regions advecting down and upstream in the flow. Therefore, it is quite reasonable to assume that a parameterization acts in a column that represents an equivalent area. However, work is now underway to assess performance of global atmospheric models (including CAM) at 0.25° and finer global resolution without significant modification to their parameterization suite (Haarsma et al., 2016) To that end, we now look toward global model resolution in this range, and into the non-hydrostatic regime.

If we consider each individual (at a given time step) spectrum as a realization of the turbulent field, we can then take an ensemble (time) average over the entire history and evaluate (4.12) for each component of the local specific kinetic energy. We present the results as a function of Brunt-Väisälä frequency at several elevations in figure 4.13. Theoretical work by Lilly (1983) followed by Métais et al. (1996) suggest that 3D stratified turbulence develops an inverse cascade of energy, but an opposing hypothesis by Lindborg (2006) suggests that, while a power law of $k^{-5/3}$ is applicable in an inertial range, the energy cascade is strictly forward into smaller scales.

Stratified turbulence caused by breaking waves in a 2D vertical slice model has been addressed by Bouruet-Aubertot, Sommeria, and Staquet (1995) indicating that the onset of turbulence is

Chapter 4. OGWD Parameterization Assessment

achieved by local overturning at a length scale corresponding to the local vertical wavenumber. Therefore, we interpret the energy spectra shown in figs. 4.13 and 4.14 as a flow forced at frequencies apparent from peaks with a forward dissipative cascade with a power law close to k^{-3} and an inverse cascade range (appropriate for the 2D slice equations solved here) with a rate close to $k^{-5/3}$, but flattened at elevations where dissipation strongly effects any larger scale (horizontal) motions driven by the inverse cascade. It remains for subsequent work to confirm and compare these findings with similar experiments in 3D.

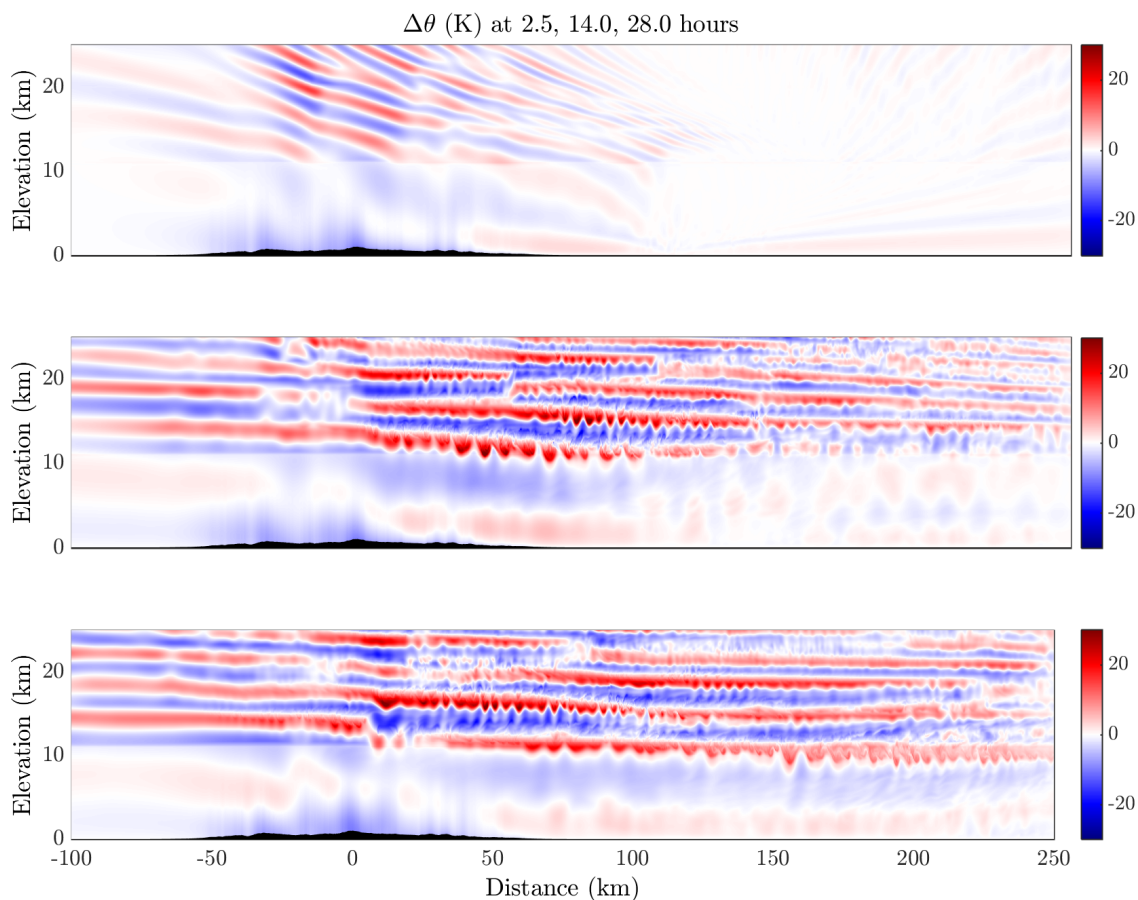


FIGURE 4.11: Potential temperature departure (K) from initial state before (2.5 hours top plot) and after (14 hours middle plot) wave breaking in the reference simulation. Bottom plot shows response at 28 hours.

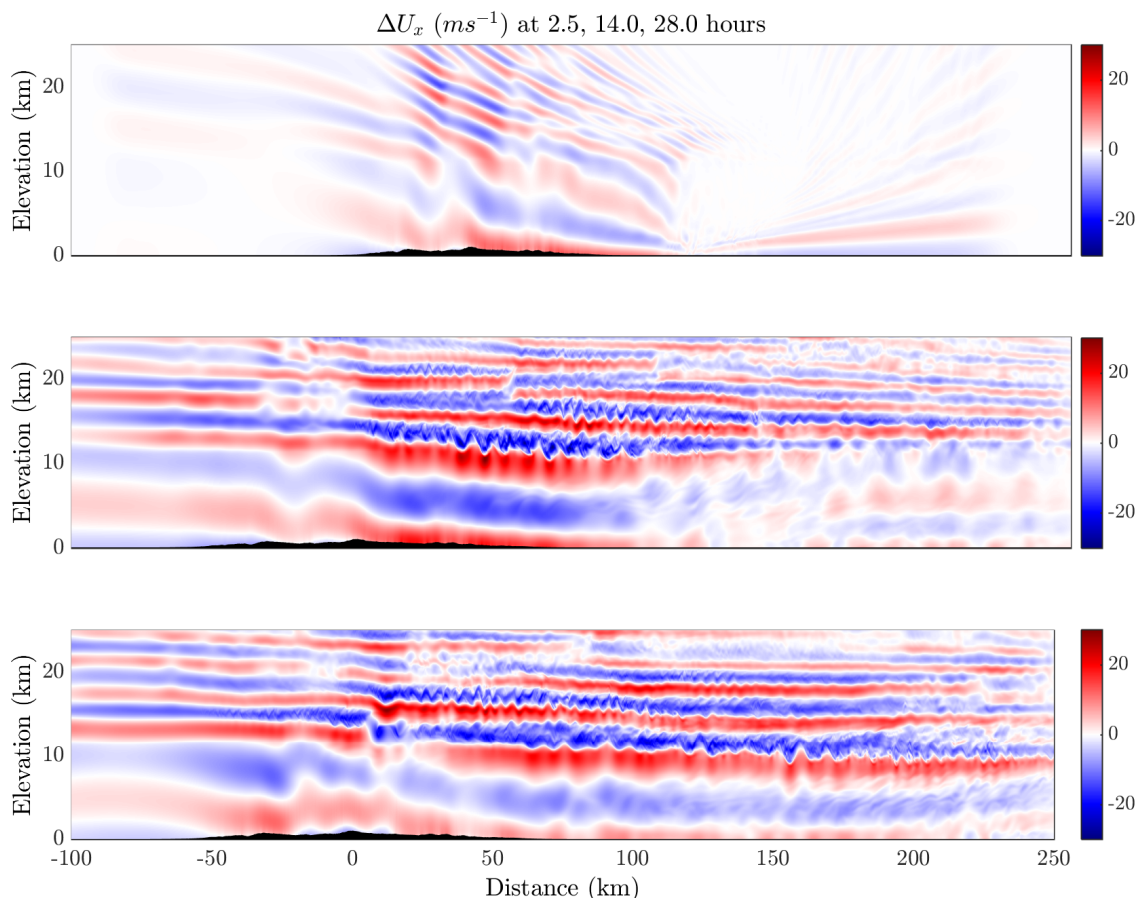


FIGURE 4.12: Horizontal velocity departure (ms^{-1}) from initial state before (2.5 hours top plot) and after (14 hours middle plot) wave breaking in the reference simulation. Bottom plot shows response at 28 hours.

The response characteristics shown in figs. 4.13 and 4.14 are significant because turbulent decay transitions from a damped inertial range into a steeper dissipative range at wavelengths from 1 to 10 km also showing strong forcing signatures in this range. Thus, a model resolution on the order of 1 km would likely underestimate the impact of gravity wave drag without the need for a parameterization. We observe this behavior in our COARSE numerical tests by inspection as simulated response tends to a quasi-steady state rather than developing any instability and an

associated turbulent breakdown.

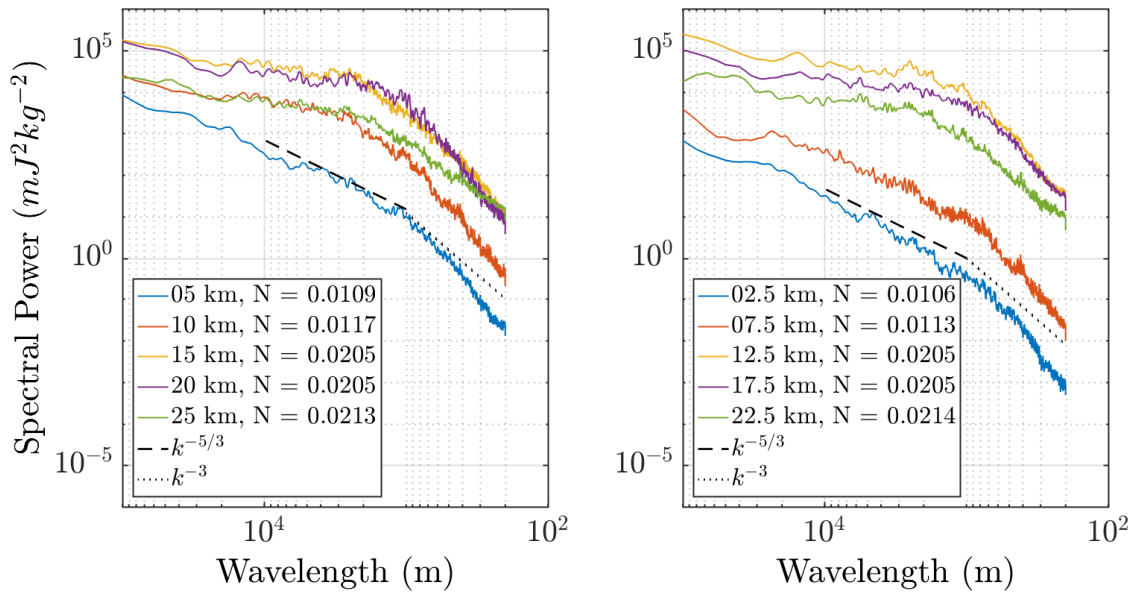


FIGURE 4.13: Horizontal component of kinetic energy power spectra as a function of elevation over wavelengths 200 to 1.0E5 m. Values of N correspond to the initial background conditions at the specified elevation.

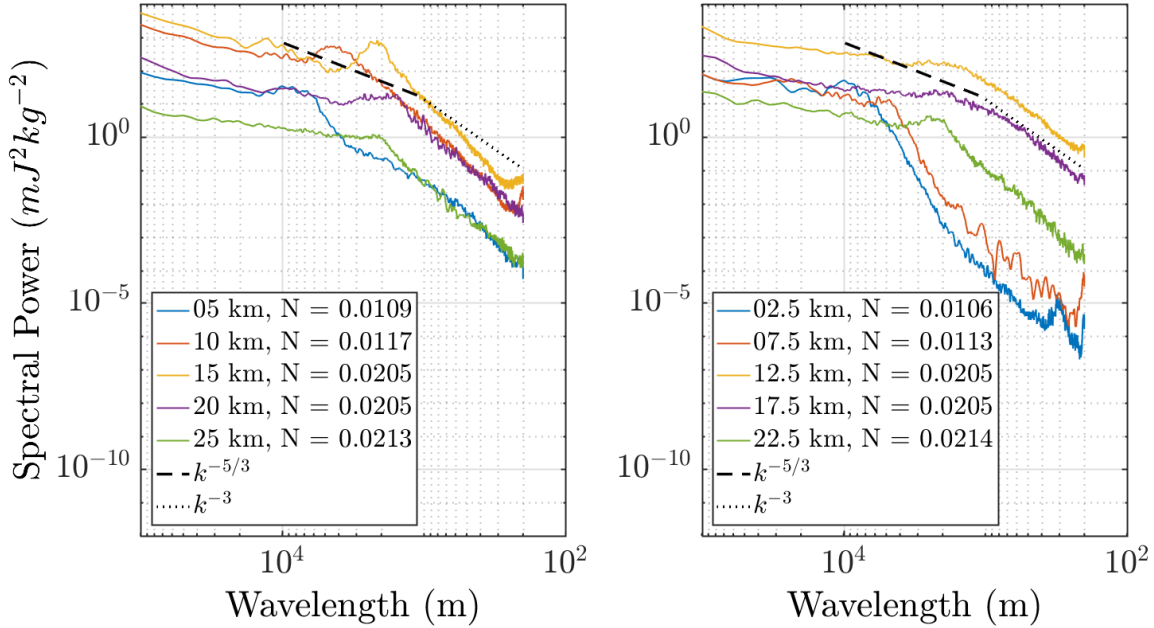


FIGURE 4.14: Vertical component of kinetic energy power spectra as a function of elevation over wavelengths 200 to 1.0E5 m. Values of \mathcal{N} correspond to the initial background conditions at the specified elevation.

If we look at the vertical component of the kinetic energy (w term in equation (4.10)) shown in figure 4.14 we can make an estimate for the cut-off wavelength/resolution where the model can support band-limited turbulence. The largest wavelengths, on the order of 5 to 10 km, occur in the troposphere layer where \mathcal{N} is small. Areas in the upper layer where stratification is strongest have a cut-off wavelength of 2 to 3 km. From these observations we hypothesize that these effects do not manifest until a model resolution less than 1km is reached. Measurements from the reference simulation are consistent with estimates from the steady linear solution in section 4.5.1. This overall structure of discrete turbulent layers superimposed on vertical wave field controlled by a strongly stratified environment validates the vortical/wave flow decomposition proposed by Lilly (1983) and used in the analysis of stratified turbulence (Riley and deBruynKops, 2003).

We now evaluate the integral in equation (4.13) over the control boundary shown in figure 4.7 to compute the net drag force in that region over the 50 hour record. The results are shown in

Chapter 4. OGWD Parameterization Assessment

Figures 4.15 and 4.16 for several control volumes with differing upper/lower boundaries. Based on qualitative inspection of figure 4.11, we also look at separate contributions of drag directly above the terrain and farther downstream (figure 4.17) in order to determine if drag is indeed distributed downstream of a terrain feature.

The initial impulsive transient is purely an artifact of the initialization. Subsequently, from 3 to 24 hours, a quasi-steady drag of approximately -150 kNm^{-1} is maintained in figure 4.15. The blue curve representing a region that includes the jet core and stratosphere shows greater drag in the first 24 hours but is punctuated by an abrupt change to positive forcing from 24 to 34 hours. We postulate that this change is due to an instability in the broader scale jet capable of inducing mixing throughout the test domain for that 10 hour period manifesting as a large (time scale) fluctuation in drag forcing. We note that the jet also exhibits an oscillation with a 3.5 hour period evident in the 1-hour mean plots. As the lower surface of the control volume is raised so as to exclude the jet feature in figure 4.15, the broader influence of the jet is lost and we see a steadier, more uniform drag forcing on the order of -75 kNm^{-1} . We then define the wave breaking region with bounds: $[-100 \text{ 250}] \text{ km}$ by $[15 \text{ 25}] \text{ km}$. Figure 4.17 the shows that the majority of the drag force does indeed occur directly over the mountain despite the presence of turbulence extending far downstream. This result suggests that column wise parameterization approaches remain useful at very high resolution.

Chapter 4. OGWD Parameterization Assessment

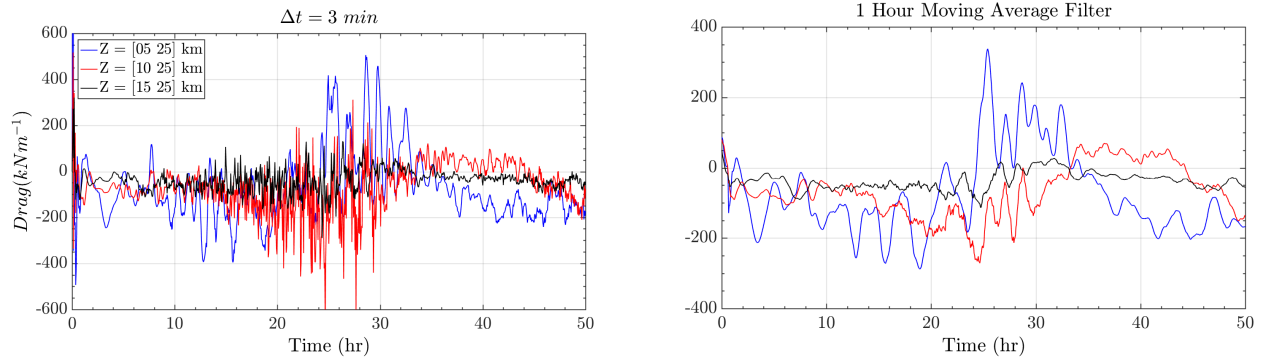


FIGURE 4.15: The net drag force with the bottom surface of the control volume changed from $Z_1 = 5$ to 15 km elevation. The control volume region is given by $[-100 \ 250]$ km by $[Z_1 \ 25]$ km in the vertical, with $Z_1 = 5$ km (blue), $Z_1 = 10$ km (red), and $Z_1 = 15$ km (black). Results from the reference resolution simulation at 100 m horizontal and vertical resolution.

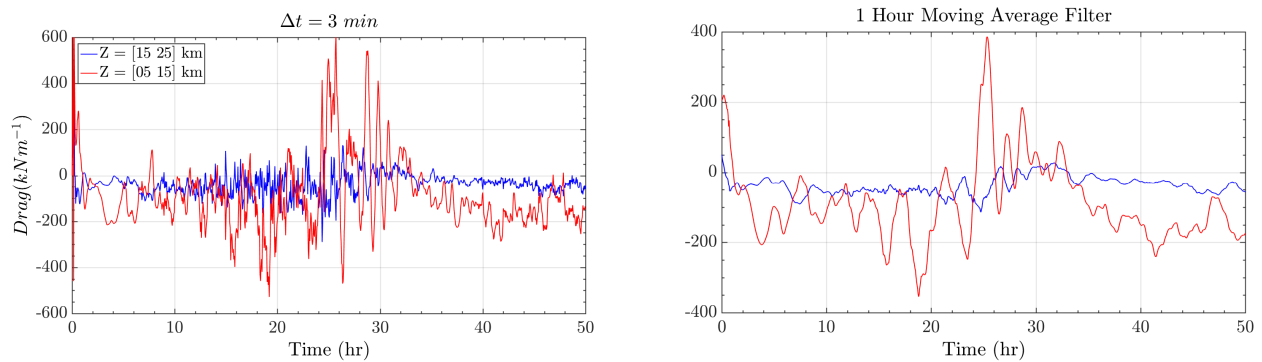


FIGURE 4.16: The net drag force comparison for wave breaking region (blue) and jet core region (red). The control volume regions are given by $[-100 \ 250]$ km by $[15 \ 25]$ km (wave breaking) and $[05 \ 15]$ km (jet core) in the vertical. Results from the reference resolution simulation at 100 m horizontal and vertical resolution.

Chapter 4. OGWD Parameterization Assessment

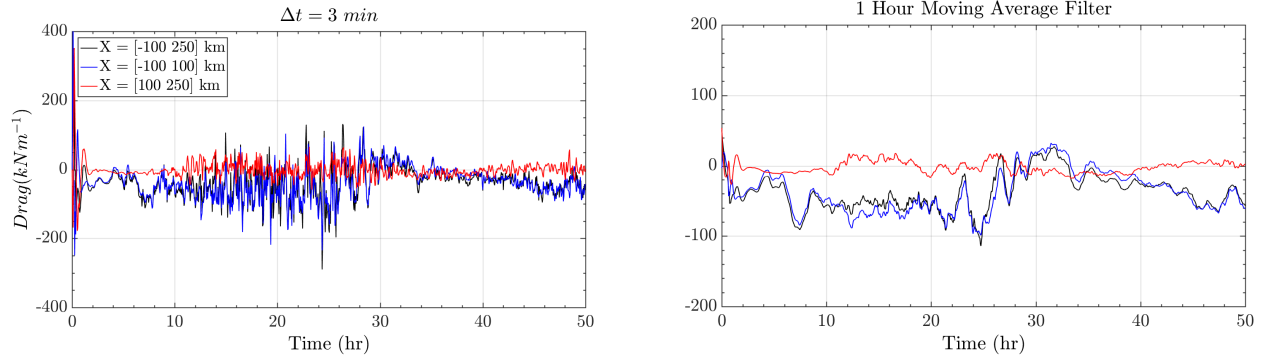


FIGURE 4.17: The net drag force comparison for wave breaking region directly above terrain (blue), in the turbulent wake (red) and the combined region (black) over the same depth. The control volume regions are given by $[-100 100]$ km by $[15 25]$ km (blue) and $[100 250]$ km by $[15 25]$ (red). Results from the reference resolution simulation at 100 m horizontal and vertical resolution.

We now compare the drag response of the wave breaking and jet core regions in figure 4.16. Flow in the jet region is characterized by stronger modes with longer periods with increased drag but capable of fluctuations with net acceleration. In contrast, the wave breaking region maintains a quasi-steady drag dominated by turbulence induced by convective wave overturning and confined to vertically narrow layers as a consequence of strong background stratification.

4.5.3 Transient drag forces - Test configurations

We compare the transient drag produced by the FINE configuration tests in order to determine the effect of terrain filtering. In all of these tests, model resolution is held constant at 200 m in both dimensions.

Chapter 4. OGWD Parameterization Assessment

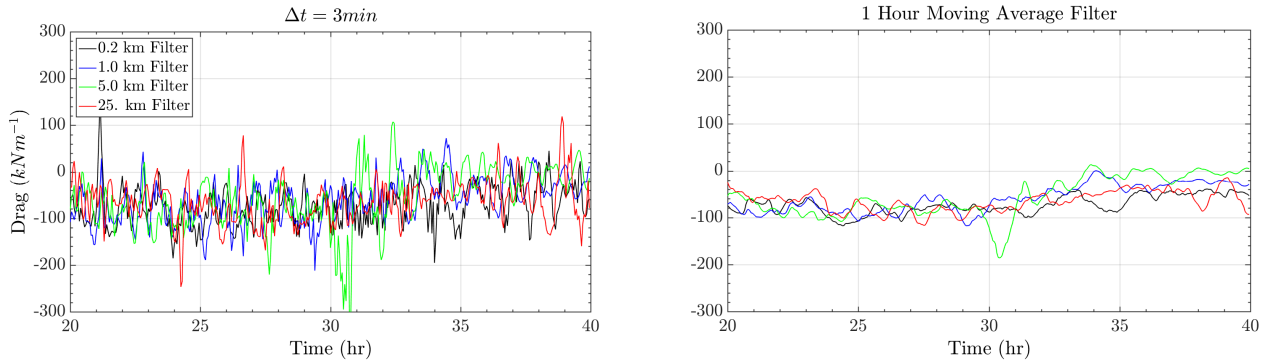


FIGURE 4.18: The net drag force comparison for wave breaking region in FINE configuration tests. The control volume region is given by [-100 250] km by [15 25] km. FINE test resolution 200 m with input filter widths of 1.0, 5.0, and 25.0 km.

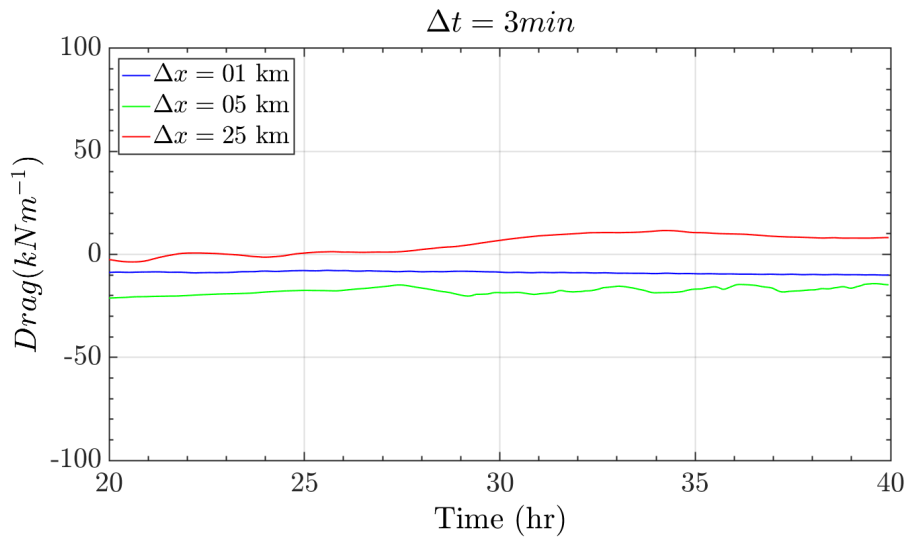


FIGURE 4.19: The net drag force comparison for wave breaking region in COARSE configuration tests. Control volume region: [-100 250] km by [15 25] km. COARSE test resolutions matching filter widths 1.0, 5.0, and 25.0 km.

There are two characteristics we note from figure 4.18: First, at a given resolution sufficient to support the necessary turbulence, all filtered inputs produce near identical mean drag and, second, the effect of the unstable jet feature is not evident in the chosen time period. The first point is explained by the fact that only the largest input modes are needed to excite the virtual

atmosphere and subsequently result in similar response. Once these primary modes break, subsequent turbulent breakdown will involve all modes within layers defined by the resonant vertical wavenumber. We conclude that, under the atmospheric conditions chosen, averaged response is practically insensitive to input wavelengths below 25 km. Second, at the FINE model resolution of 200 m, the signature of larger scale unstable jet is not visible in figure 4.18 as we have identified that its influence manifests in drag at lower levels.

We note that COARSE configurations showed a qualitatively different behavior in that no breaking was evident at 1.0, 5.0, and 25.0 km resolutions and therefore drag estimates are significantly underestimated and in some cases may suggest acceleration rather than drag as shown in figure 4.19. The computation of drag based on 4.13 relies on evaluating discrete integrals admitting greater error at coarser resolution given the same control volume. This estimate is much more reliable at the reference resolution. Also, the limited area model (particularly at 25 km) suffers from spurious reflections near the lateral absorption layers as a consequence of decreased resolution. A natural solution to these limitations is to conduct these experiments on a spherical domain, but this would greatly expand computational requirements. Nonetheless, the COARSE experiments are characterized by a flow that does not support the necessary turbulent cascade that results in an accurate direct estimate of drag and we generally observe drag on the order of 25% of what is expected from figure 4.18. Under these conditions we would expect that a parameterization scheme would make up this drag deficit even in the absence of any turbulent features.

4.5.4 Parameterization input fields

In order to explore how the parameterization physics will produce drag tendencies within a model simulation, we construct time averaged input fields for total horizontal velocity U and $\ln \theta$. The parameterization begins by checking the assumption of vertical propagation from obstacle frequencies well below the model resolution at a given column. For the background conditions

defined in our simulations we have,

$$2\pi \frac{U_0}{N_0} = 2000.0\pi \approx 6400.0\text{m} \quad (4.17)$$

where the subscripts 0 indicate surface values of background wind and bouyancy.

Following McFarlane (1987), we assume that propagation is only possible for terrain inputs broader than the value given in (4.17). We see immediately that filtered inputs, at 0.2, 1.0, and 5.0 km, for both FINE and COARSE configurations will result in null parameterization response if we follow the typical guidance that propagating modes correspond to terrain features “much greater” in length than the value computed in (4.17).

We focus on the FINE and COARSE configurations at 25 km in order to characterize the performance of the parameterization scheme. This is a pertinent choice since propagating modes are allowed according to (4.17) and because current global modeling efforts are approaching or have reached this resolution level. Figure 4.20 shows total horizontal velocity in FINE and COARSE configurations. We note the presence of reversed flow layers in the FINE test indicative of overturned flow. These features are notable in the tropospheric layer just in the lee of the mountain and at several altitudes in the stratospheric layer. The parameterization scheme will capture regions where a “critical layer” is present, i.e. where total flow velocity vanishes and impose that all parameterized stress vanishes across such a layer. This results in maximum dissipation and drag without the possibility of any wave energy to continue propagating above said critical level. Thus, we expect drag to be overestimated locally in the FINE configuration due to detection of critical layers. We emphasize that enabling drag parameterization in an operational setting at the FINE resolution would be inappropriate with respect to the assumptions in the original parameter model derivation (see section 4.2.1). We use these results to show an extreme bounding case of what can be expected from such a scheme if a model is run at finer resolution.

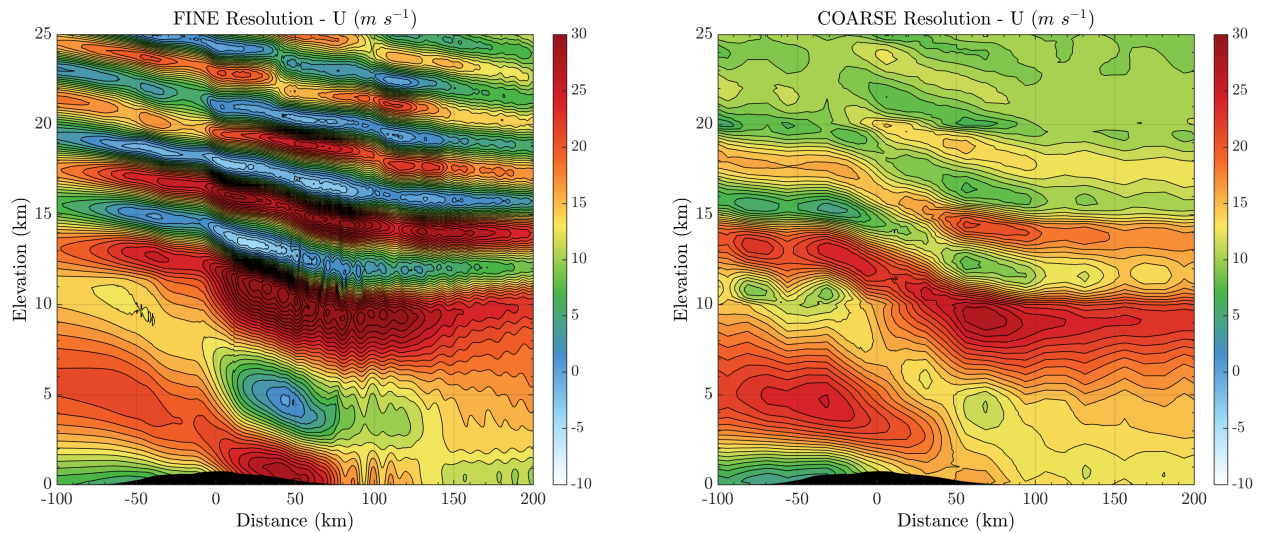


FIGURE 4.20: The ensemble (time) averaged total horizontal velocity with (left) FINE resolution and (right) COARSE resolution simulations with 25 km terrain filtering.

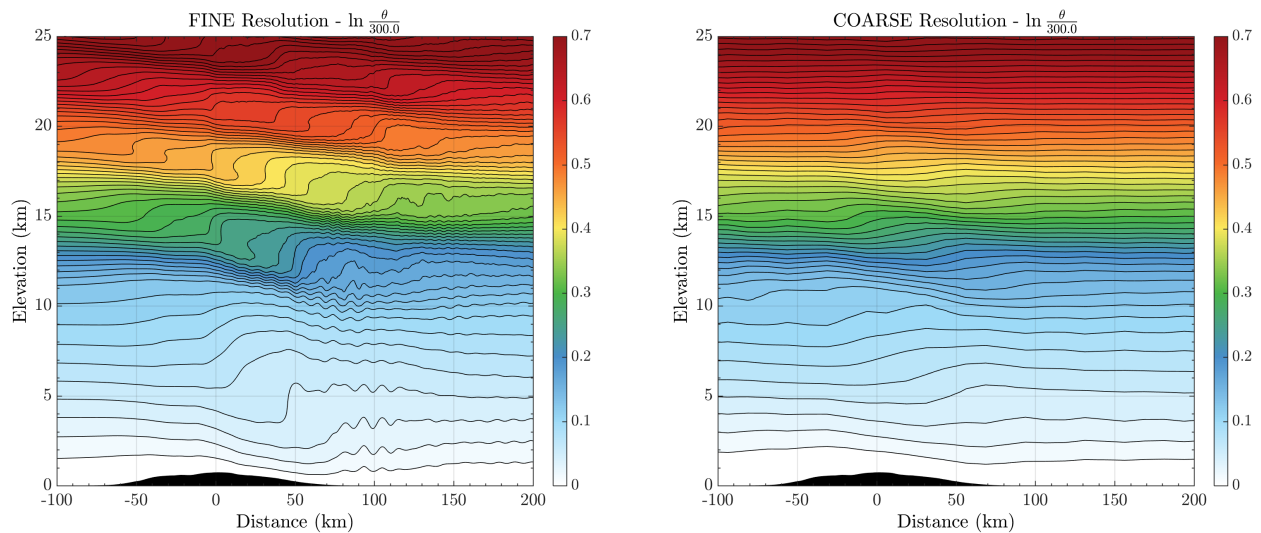


FIGURE 4.21: The ensemble (time) averaged total $\ln \theta$ with (left) FINE resolution and (right) COARSE simulations with 25 km terrain filtering.

Alternatively, in the COARSE test where flow resolution matches terrain filtering, no such critical layers are evident as seen in figure 4.20 right. In fact, truly coarse simulations under the

background conditions chosen will tend to approach a quasi-steady state rather than producing turbulent layers. This result is consistent with spectra from the reference simulation (Figs. 4.13 and 4.14) where turbulent cascades are only possible at length scales below 10 (km). With the presence of critical layers from the resolved field, we expect the parameterization to underestimate drag in the COARSE configuration.

The wave amplitude function in (4.4) also requires that the local Brunt-Väisälä frequency be evaluated. Waves are required to propagate in stable layers only since \mathcal{N} must be real and positive. Figure 4.21 shows the $\ln \theta$ input fields in the FINE and COARSE configurations. We note the presence of convective instabilities where isentropes are distorted and negative vertical gradients are possible. These layers coincide with overturned flow evident in figure 4.20 left. Again, we expect the parameterization to be biased in detecting critical layers and imposing maximum stress dissipation. In contrast, the COARSE configuration shows no evidence of overturned flow, but with the same general wave pattern as the FINE tests. In this case we expect the parameterization to proceed in amplifying waves, imposing saturation, and dissipating stress accordingly rather than overwriting with detection of critical layers.

4.5.5 Parameterized drag

Applying the static input fields given in section (4.5.3), we compute parameterized drag for the FINE and COARSE configurations. We concentrate on the tests at 25 km filtering and resolution since no drag is given in the other tests as a consequence of non-propagation at those scales. As predicted from the formulation of the parameter scheme, figure 4.23 shows stress profiles heavily influenced by the presence of reverse flow in the input field which is interpreted by the scheme as a critical layer and therefore shows a concentrated layer of drag between 10 and 15 km above the mountain. This behavior effectively negates the ability to capture any breaking layers above this level. We can expect this behavior under conditions where resolution is sufficient to produce explicit breaking, but the parameterization is left on. We also compare the total volume integrated drag based on acceleration data on the right in figs. 4.23 and 4.24 where the COARSE configuration

Chapter 4. OGWD Parameterization Assessment

gives a total of approximately 47 kNm^{-1} approximately matching values shown in figure 4.18. However, we note that the FINE configuration represents a limiting case where turbulent breaking is well resolved (200 m grid scale) and no parameterization scheme would be needed. The total parameterized drag of 81 kNm^{-1} confirms that this scheme will tend to overestimate drag based critical layer detection in a well resolved flow.

The COARSE configuration is much more representative of a computation done on a global model at a native resolution (in both terrain and grid scale) of 25 km. The behavior of the parameterization is distinctly different as seen in figure 4.24. In particular we see that wave stress divergence only takes place in layers above 15 km and the pattern in the stress profiles corresponds to saturated waves that are partially consumed but survive to grow and dissipate at higher elevations. The structure of the wave pattern is consistent with our reference simulations in the vertical, but, by construction, all wave action is confined to columns directly above the terrain. We saw in the reference results of figure 4.11 that turbulent wakes extend downstream several times the characteristic width of the mountain. In this regard, the parameterization scheme fails to capture such flow response. However, a user could compensate by increasing the source input height as in figure 4.22.

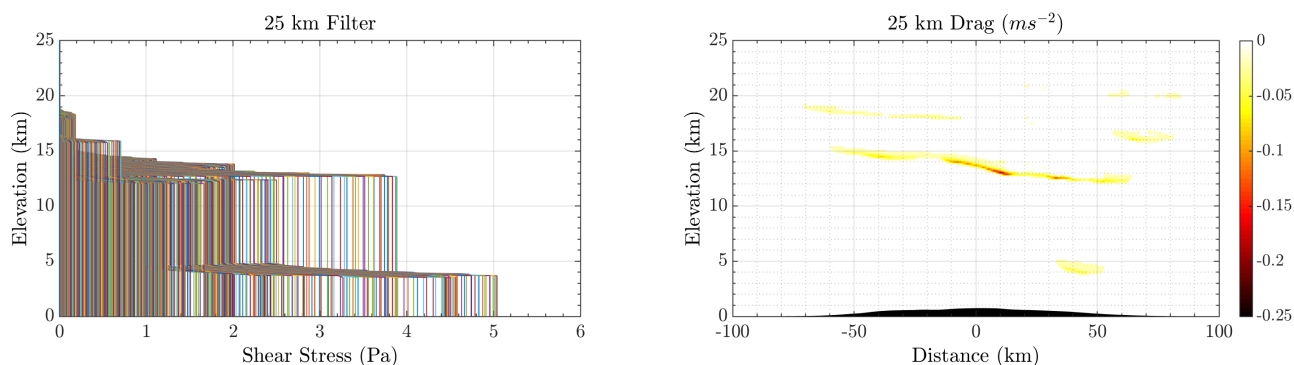


FIGURE 4.23: The parameterized stress and deceleration drag for the FINE configuration. Total drag estimate in [-100 250] km by [15 25] km region: 80.6 kNm^{-1} .

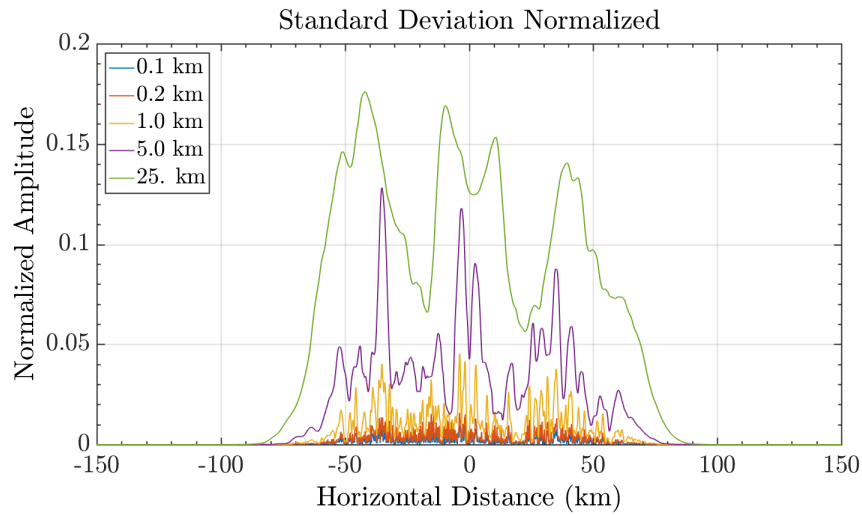


FIGURE 4.22: The spatial distribution of standard deviation for each filtering level. Filter widths are 0.1 km (blue), 0.2 km (orange), 1.0 km (yellow), 5.0 km (purple), 25.0 km (green).

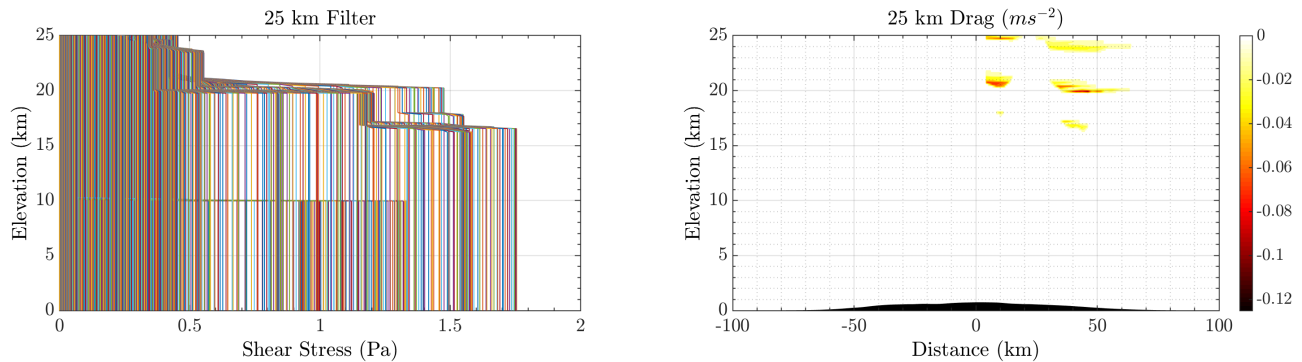


FIGURE 4.24: The parameterized stress and deceleration drag for the COARSE configuration. Total drag estimate in $[-100\ 250]$ km by $[15\ 25]$ km region: $46.9\ \text{kNm}^{-1}$.

4.6 Conclusions

Our work indicates that the classical sub-grid wave stress parameterization will either be null or provide incorrect drag tendencies at global model resolutions below 25 km. Furthermore, prediction of wave induced drag at near and non-hydrostatic scale (below 10 km) is dominated by truncated turbulent cascades that require resolution well below 1 km. The parameterization scheme

Chapter 4. OGWD Parameterization Assessment

of Lindzen (1981) and McFarlane (1987) was designed for global circulation models well in the hydrostatic regime. As model resolution approach the range (1 to 10 km) where orographically induced gravity wave trains are more fully resolved but breaking is not explicitly captured, a problem arises where neither model nor the parameter scheme predict any drag. In this situation no admissible input wavelengths (per (4.5)) are available to the parameterization from the sub-grid domain as these are now being resolved by the model. However, we confirm that a column wise parameterization scheme remains applicable at high resolution. This represents a significant simplification despite the need to represent more processes throughout a column in addition to wave amplitude saturation.

Advanced parameterization schemes have been devised to treat low-level (elevation less than 10 km as extensions of surface shear layer turbulent theory with roughness length parameters associated with the underlying terrain spectra. Recent examples include the work of Beljaars, Brown, and Wood (2004) which extended that of Wood and Mason (1993) by incorporating real terrain spectra to a low level turbulent drag scheme. Scinocca and McFarlane (2000) made several improvements to the basic parameterization studied here by incorporating a more complete source stress that takes into account blocking and near surface dynamic forcing. In essence, such schemes cover small scale dynamics in the lowest layers based on classical turbulence theory. Our study shows that a proper representation of similar turbulent layers characterized by fixed vertical extent related to background stratification is necessary to capture drag produced in the upper troposphere and stratosphere type layers. Furthermore, a scheme applicable below 10 km resolution should be formulated to correct partially resolved waves for amplitude with application of a localized turbulence model to account for purely nonlinear effects occurring at the sub-grid scale. One straightforward way of accomplishing this is to employ variable resolution over, but not necessarily downstream, of terrain although this approach may be limited by computational cost and added complication in carrying output fields over an irregular grid. The author also has reservations about static variable resolution in the presence of propagating signals from fine to coarse resolutions where significant distortions can take place.

Chapter 5

Summary, Conclusions, and Future Directions

The questions we are attempting to answer surrounding Earth's climate system are growing in scope, complexity, and urgency. While much of the 20th century saw great theoretical advances in understanding geophysical flows, a parallel effort in the use of numerical approximations sought to complement the limitations of theoretical work. With the advent of ever higher computer performance, it is tempting to develop an over-reliance on numerical modeling in studies of the atmosphere. The aim of this work has been, partly, to bridge the widening gap between "model user" and "model developer" with the assumption that, going forward, an atmospheric scientist must embrace both paradigms in order to properly analyze and scrutinize the growing torrent of model data produced. We demonstrate a process by which model development may grow into scientific inquiry with the correct knowledge of the properties and limitations of the modeling tool. Indeed, theoretical work is not abandoned but fully integrated into the design of numerical experiments and the interpretation of results.

Many questions remain in the study of cross mountain flows. The author is particularly interested in a similar study to the present dedicated to resolving clouds and precipitation forced by mountains. This would necessitate extending the simulations to 3D and including moisture

Chapter 5. Summary, Conclusions, and Future Directions

and cloud physics parameterizations and demand a rigorous evaluation of moist parameterizations in the non-hydrostatic context. This would greatly widen the test space and increase computational resources required, but provides great value to long term climate studies. The linear model presented in chapter 3.7 would be suitable to development of time integration methods (Additive Runge-Kutta, multistage, multistep, etc.) both for atmospheric models and as part of an ocean/atmosphere coupled model. Other possible projects include flight planning for small aircraft over mountainous terrain, and identification of regions known as climate refuges where local dynamics combine to create conditions stable against overall climate change.

In this work we have produced a reliable, and fast research dynamical core that is well suited to scientific questions focused on dynamical processes beyond the reach of theoretical and/or observational techniques. In the process we develop a simplified 2D linear model that retains much of the dynamical characteristics of the full equations and provides a fast reliable tool to design more comprehensive numerical experiments in mountain waves. We then investigate the nature of turbulent dissipation of mountain waves through careful design of controlled numerical experiments founded on the linear theory of gravity waves extended for the purpose of designing such tests. Our high fidelity simulations provide insight into the coming changes necessary in operational global circulation models to account for mountain wave drag in a robust manner. The result is that current parameterization schemes will need to be revised or reformulated in order to enable higher horizontal resolution grids (20 km to 1 km range) in global models. The singular challenge lies in the representation of stratified turbulence at very fine scale distributed over discrete layers throughout the depth of the atmosphere over grids that reproduce the characteristic vertical standing wave trains but are insufficient in capturing subsequent turbulent cascades. We hope that our simulations will provide a foundation for future work in developing new parameterization schemes for orographic gravity wave drag.

Appendix A

Appendix A.

A.1 Metric terms based on new terrain decay function

Starting from (??) we differentiate with respect to z on both sides such that:

$$\frac{d}{dz} \left[z = H\zeta + \frac{dz}{dh}h(x) \right] \Rightarrow \quad (\text{A.1})$$

$$1 = H \frac{d\zeta}{dz} + h(x) \frac{d}{dz} \left(\frac{dz}{dh} \right) \quad (\text{A.2})$$

Then, using (??),

$$\frac{dz}{dh} = e^{(-\frac{P}{Q}\zeta)} \left[\cos \left(\frac{\pi}{2}\zeta \right) \right]^P + A\zeta(1 - \zeta) \quad (\text{A.3})$$

and by the Chain Rule,

$$\frac{d}{dz} \left(\frac{dz}{dh} \right) = \frac{d}{d\zeta} \left(\frac{dz}{dh} \right) \frac{d\zeta}{dz}. \quad (\text{A.4})$$

Substituting back into (A.2) then:

$$\frac{d\zeta}{dz} = \left\{ H + h(x) \left[\frac{d}{d\zeta} \left(\frac{dz}{dh} \right) \right] \right\}^{-1} \quad (\text{A.5})$$

where

$$\frac{d}{d\zeta} \left(\frac{dz}{dh} \right) = -Pe^{(-\frac{P}{Q}\zeta)} \left[\cos \left(\frac{\pi}{2}\zeta \right) \right]^{(P-1)} \left[\frac{1}{Q} \cos \left(\frac{\pi}{2}\zeta \right) + \frac{\pi}{2} \sin \left(\frac{\pi}{2}\zeta \right) \right] + A(1 - 2\zeta). \quad (\text{A.6})$$

Finally, the parameters P and A control the overall rate of decay through the vertical domain and the minimum rate at top of the model. For this study we use $P = 20$, $Q = 5$ and $A = 0.001$, but we note these values may be tuned more aggressively if needed.

Appendix A.

A.2 Linearization of the Inviscid Equations - Conservation Form

Here we consider an alternative linearization of the nonrotating Euler equations in conservation form,

$$\begin{aligned}
 \frac{\partial}{\partial x} (\rho u^2) + \frac{\partial}{\partial z} (\rho u w) + \frac{\partial p}{\partial x} &= 0, \\
 \frac{\partial}{\partial x} (\rho u w) + \frac{\partial}{\partial z} (\rho w^2) + \frac{\partial p}{\partial z} &= -\rho g, \\
 \frac{\partial}{\partial x} (\rho u) + \frac{\partial}{\partial z} (\rho w) &= 0, \\
 \frac{\partial}{\partial x} (\rho u \theta) + \frac{\partial}{\partial z} (\rho w \theta) &= 0.
 \end{aligned} \tag{A.7}$$

where pressure p is related to $(\rho\theta)$ by the definition of potential temperature,

$$\begin{aligned}
 \rho\theta &= \frac{p}{R_d} \left(\frac{p_0}{p} \right)^\kappa, \\
 \kappa &= \frac{c_p}{R_d}.
 \end{aligned} \tag{A.8}$$

where $R_d = 287.06 \text{JK}^{-1}$ is the gas constant for dry air, and $c_p = 1004.5 \text{JK}^{-1}$ is the heat capacity at constant pressure for dry air. The reference pressure $p_0 = 1.0 \times 10^5 \text{Pa}$. And solving (A.8) for p ,

$$\begin{aligned}
 p &= \left(\frac{R_d}{(p_0)^\kappa} \right)^\gamma (\rho\theta)^\gamma = A (\rho\theta)^\gamma, \\
 \gamma &= \frac{1}{1 - \kappa} = 1.4.
 \end{aligned} \tag{A.9}$$

Appendix A.

Then, equation (A.7) may be written as the xz Cartesian divergence of two flux vectors,

$$\frac{\partial}{\partial x} \begin{bmatrix} \frac{(\rho u)^2}{\rho} + A (\rho \theta)^\gamma \\ \frac{(\rho u)}{\rho} (\rho w) \\ (\rho u) \\ \frac{(\rho u)}{\rho} (\rho \theta) \end{bmatrix} + \frac{\partial}{\partial z} \begin{bmatrix} \frac{(\rho w)}{\rho} (\rho u) \\ \frac{(\rho w)^2}{\rho} + A (\rho \theta)^\gamma \\ (\rho w) \\ \frac{(\rho w)}{\rho} (\rho \theta) \end{bmatrix} = \frac{\partial f_x}{\partial x} + \frac{\partial f_z}{\partial z} = 0 \quad (\text{A.10})$$

Our linearization proceeds by considering the Jacobian of the flux vectors in (A.10) such that for a vector of quantities $q = [\rho u, \rho w, \rho, \rho \theta]^T$ expanded as $q = \bar{q} + q'$,

$$\frac{\partial f_x}{\partial q} \Big|_{\bar{q}} \frac{\partial q'}{\partial x} + \frac{\partial}{\partial z} \left(\bar{f}_z + \frac{\partial f_z}{\partial q} \Big|_{\bar{q}} q' \right) = 0. \quad (\text{A.11})$$

where overbars denote background quantities that are time and x invariant. And expanding the vertical derivative terms,

$$\begin{aligned} \frac{\partial}{\partial z} \left(\frac{\partial f_z}{\partial q} \Big|_{\bar{q}} q' \right) &= \frac{\partial}{\partial z} \left(\frac{\partial f_z}{\partial q} \Big|_{\bar{q}} \right) q' + \left(\frac{\partial f_z}{\partial q} \Big|_{\bar{q}} \right) \frac{\partial q'}{\partial z} \\ \frac{\partial}{\partial z} (\bar{f}_z) q' &= -\rho g q'. \end{aligned} \quad (\text{A.12})$$

where g is the gravitational constant.

Computing the terms in (A.12), using the resulting continuity equation, and eliminating terms from horizontal momentum with the entropy equation we arrive at the following linearization,

Appendix A.

$$\bar{u} \frac{\partial}{\partial x} (\rho u)' + \left(\frac{\partial \bar{u}}{\partial z} - \bar{u} \frac{\partial \ln \bar{\theta}}{\partial z} \right) (\rho w)' + \frac{\gamma \bar{p} - \bar{\rho} \bar{u}^2}{\bar{\rho} \bar{\theta}} \frac{\partial}{\partial x} (\rho \theta)' = 0, \quad (\text{A.13})$$

$$\bar{u} \frac{\partial}{\partial x} (\rho w)' + \frac{\gamma \bar{p}}{\bar{\rho} \bar{\theta}} \frac{\partial}{\partial z} (\rho \theta)' + g \rho' - \frac{g(\gamma - 1)}{\bar{\theta}} (\rho \theta)' = 0, \quad (\text{A.14})$$

$$\frac{\partial}{\partial x} (\rho u)' + \frac{\partial}{\partial z} (\rho w)' = 0, \quad (\text{A.15})$$

$$\frac{\partial \ln \bar{\theta}}{\partial z} (\rho w)' - \bar{u} \frac{\partial \rho'}{\partial x} + \frac{\bar{u}}{\bar{\theta}} \frac{\partial}{\partial x} (\rho \theta)' = 0. \quad (\text{A.16})$$

This equation set corresponds directly to the first iteration in a nonlinear solution where the Jacobian is initialized to the background, steady, x -invariant background. An analysis of equations (3.7) by combining the thermodynamic equation algebraically into the horizontal momentum equation reveals a constraint for the vertical variation of vertical velocity as follows:

$$\frac{\partial}{\partial z} (\rho w)' + \left(\frac{d \ln \bar{\theta}}{dz} - \frac{d \ln \bar{u}}{dz} \right) (\rho u)' + \left(\frac{\gamma \bar{p} - \bar{\rho} \bar{u}^2}{\bar{\rho} \bar{\theta}} \right) \frac{\partial (\rho \theta)'}{\partial x} = 0 \quad (\text{A.17})$$

If we neglect the contribution from horizontal gradients in heat flux from (A.17), then a first order ordinary differential equation in ρw remains:

$$\frac{\partial}{\partial z} (\rho w)' \approx \left(-\frac{d \ln \bar{\theta}}{dz} + \frac{d \ln \bar{u}}{dz} \right) (\rho w)' \quad (\text{A.18})$$

Use of the conservative equations presents a distinct advantage in that vertical momentum does not change (grow or decay) in response to background density changes. We can envision practical situations where background conditions are derived from observational data with vertical gradients approximated crudely and computing on vertical momentum rather than vertical velocity is advantageous as a significant sensitivity is removed in the conservative equation set.

Appendix B

Appendix B.

B.1 Linear Steady State Model Solution

The total prognostic state is decomposed into background (over bar) and perturbation (primed) components as follows:

$$\begin{aligned}u &= \bar{u}(z) + u'(x, z, t), \\w &= w'(x, z, t), \\\ln p &= \ln \bar{p}(z) + (\ln p)'(x, z, t), \\\ln \theta &= \ln \bar{\theta}(z) + (\ln \theta)'(x, z, t).\end{aligned}\tag{B.1}$$

where $\bar{u}(z)$, $\bar{p}(z)$, and $\bar{\theta}(z)$ are the height dependent, steady background jet and thermodynamic profiles (pressure and potential temperature). These may be continuous analytic or piecewise continuous functions where discontinuous gradients are admissible by our solution method. Also, note that the decomposition of thermodynamic quantities applies to the natural logarithm of density and pressure in order to better approximate the “small perturbation” assumption in the subsequent linearization.

Assuming a prognostic vector $\mathbf{q} = [u' \ w' \ (\ln p)' \ (\ln \theta)']^T$, the interior system may be written as

$$(\mathbf{L} + \mathbf{B})\mathbf{q} = \mathbf{0},\tag{B.2}$$

Appendix B.

where

$$\mathbf{L} + \mathbf{B} = \begin{bmatrix} \bar{u} \frac{\partial}{\partial x} & 0 & \frac{\bar{p}}{\bar{\rho}} \frac{\partial}{\partial x} & 0 \\ 0 & \bar{u} \frac{\partial}{\partial x} & \sigma \frac{\bar{p}}{\bar{\rho}} \frac{\partial}{\partial \xi} & 0 \\ \frac{\partial}{\partial x} & \sigma \frac{\partial}{\partial \xi} & \bar{u} \frac{\partial}{\partial x} & 0 \\ 0 & 0 & 0 & \bar{u} \frac{\partial}{\partial x} \end{bmatrix} + \begin{bmatrix} 0 & \sigma \frac{\partial \bar{u}}{\partial \xi} & 0 & 0 \\ 0 & 0 & g_c \left(\frac{1-\gamma}{\gamma} \right) & (-g_c) \\ 0 & \sigma \frac{\partial \ln \bar{p}}{\partial \xi} & 0 & 0 \\ 0 & \sigma \frac{\partial \ln \bar{\theta}}{\partial \xi} & 0 & 0 \end{bmatrix}, \quad (\text{B.3})$$

Applying the Fourier transform over the x dimension and assuming that background quantities are invariant in x by construction then (B.3) becomes,

$$\mathbf{L} + \mathbf{B} = \begin{bmatrix} \bar{u} ik & 0 & \frac{\bar{p}}{\bar{\rho}} ik & 0 \\ 0 & \bar{u} ik & \sigma \frac{\bar{p}}{\bar{\rho}} \frac{\partial}{\partial \xi} & 0 \\ ik & \sigma \frac{\partial}{\partial \xi} & \bar{u} ik & 0 \\ 0 & 0 & 0 & \bar{u} ik \end{bmatrix} + \begin{bmatrix} 0 & \sigma \frac{\partial \bar{u}}{\partial \xi} & 0 & 0 \\ 0 & 0 & g_c \left(\frac{1-\gamma}{\gamma} \right) & (-g_c) \\ 0 & \sigma \frac{\partial (\ln \bar{p})}{\partial \xi} & 0 & 0 \\ 0 & \sigma \frac{\partial (\ln \bar{\theta})}{\partial \xi} & 0 & 0 \end{bmatrix}, \quad (\text{B.4})$$

where i is the imaginary unit, and k is the horizontal wavenumber.

We now apply a truncated Lagrange expansion for vertical ξ derivatives in (B.4) using the

Appendix B.

following dense matrix operator with a set of discrete nodes $z_k \in [0 H]$ for $k = 1, N$ where N is a positive integer, z_k are the Chebyshev nodes up to order N distributed over the given interval. Again, following Shen, Tang, and Wang (2011), the vertical derivative matrix operator is:

$$\frac{\partial}{\partial \xi} = \mathbf{D}_z = D_{kj} = \begin{cases} \frac{\mathcal{L}'_N(x_k)}{\mathcal{L}'_N(x_j)} \left(\frac{1}{x_k - x_j} \right) : k \neq j \\ \frac{x_k}{1 - (x_k)^2} : k = j \end{cases} \quad (\text{B.5})$$

where \mathcal{L}' are the derivatives of Lagrange basis polynomials up to order N computed in recursive fashion. We implement this discrete derivative with the matrix package of (Weideman and Reddy, 2000). The result transforms (B.2) into a sparse matrix inversion problem. The system is constrained by applying free-slip boundary conditions at the bottom and top boundaries are imposed by stating that the component of the velocity normal to the terrain must vanish. That is,

$$\vec{\mathbf{u}} \cdot \hat{\mathbf{n}} = \vec{\mathbf{u}} \cdot \frac{\vec{\nabla} \phi}{|\vec{\nabla} \phi|} = 0, \quad (\text{B.6})$$

where $\phi = z - h(x) = 0$ is the level set representation of the terrain surface.

If the gradient of ϕ in Cartesian geometry is $\vec{\nabla} \phi = -\frac{\partial h}{\partial x} \hat{\mathbf{i}} + \hat{\mathbf{k}}$, then following (B.6) the kinematic boundary condition is stated in physical and Fourier space as,

$$w' - u' \frac{\partial h}{\partial x} = \bar{u} \frac{\partial h}{\partial x}, \quad (\text{B.7})$$

$$\hat{w}' - \hat{u}'(ikh) = \bar{u}(ikh). \quad (\text{B.8})$$

Here, a further approximation may be taken where the term $u' \frac{\partial h}{\partial x}$ is regarded as a product of perturbation quantities and hence neglected. The top boundary condition is simply that $w' = 0$.

B.2 Terrain Input Processing

In order to generate quasi-realistic 2D terrain profiles for a limited area model, elevation data in Fig. 4.1 is parsed into East-West cross sections. Then the following pre-processing is performed to generate a terrain profile in our simulation tests:

1. Normalize height by the maximum.
2. Circular shift the data to center the peak value at the origin.
3. Multiply by the following spatial windowing function:

$$W(x) = e^{-\left(\frac{x}{a}\right)^4}. \quad (\text{B.9})$$

where $a = 50\text{km}$.

4. Apply a moving average filter of widths $2\Delta F = 0.1, 0.2, 1.0, 5.0, \text{ and } 25.0\text{km}$. The filtered value at a location is found by the following centered moving average filter,

$$\bar{h}_i = \frac{1}{2N} \sum_{i-N}^{i+N} h_i : N = \left\lceil \frac{\Delta F}{\Delta x} \right\rceil. \quad (\text{B.10})$$

where ΔF is half the filter width, $\Delta x = 30\text{m}$, the native resolution of the terrain map, and N is the resulting number of grid points spanned by the average calculation.

4. Multiply by a constant peak height of 1000m for our tests.

Bibliography

- Arakawa, A. and S. Moorthi (1988). "Baroclinic instability in vertically discrete systems". In: *Journal of Atmospheric Science* 45(11), pp. 1688–1708. DOI: [10.1175/1520-0469\(1988\)045<1688 : BIIVDS>2.0.CO;2](https://doi.org/10.1175/1520-0469(1988)045<1688:BIIVDS>2.0.CO;2).
- Ascher, U. M., S. J. Ruuth, and R. J. Spiteri (1997). "Implicit-explicit Runge-Kutta methods for time-dependent partial differential equations". In: *Appl. Numer. Math.* 25(2-3), pp. 151–167. ISSN: 0168-9274. DOI: [10.1016/S0168-9274\(97\)00056-1](https://doi.org/10.1016/S0168-9274(97)00056-1).
- Bacmeister, J. T. and M. R. Schoeberl (1989). "Breakdown of Vertically Propagating Two-Dimensional Gravity Waves Forced by Orography". In: *Journal of the Atmospheric Sciences* 46(14), pp. 2109–2134. DOI: [10.1175/1520-0469\(1989\)046<2109:BOVPTD>2.0.CO;2](https://doi.org/10.1175/1520-0469(1989)046<2109:BOVPTD>2.0.CO;2).
- Beljaars, A. C. M., A. R. Brown, and N. Wood (2004). "A new parametrization of turbulent orographic form drag". In: *Quarterly Journal of the Royal Meteorological Society* 130(599), pp. 1327–1347. ISSN: 1477-870X. DOI: [10.1256/qj.03.73](https://doi.org/10.1256/qj.03.73).
- Billant, P. and J-M. Chomaz (2001). "Self-similarity of strongly stratified inviscid flows". In: *Physics of Fluids* 13(6), pp. 1645–1651. DOI: [10.1063/1.1369125](https://doi.org/10.1063/1.1369125).
- Bouruet-Aubertot, P., J. Sommeria, and C. Staquet (1995). "Breaking of standing internal gravity waves through two-dimensional instabilities". In: *Journal of Fluid Mechanics* 285, 265–301. DOI: [10.1017/S0022112095000541](https://doi.org/10.1017/S0022112095000541).
- Bretherton, F. P. (1969a). "Momentum transport by gravity waves". In: *Quarterly Journal of the Royal Meteorological Society* 95, pp. 213–243. DOI: [10.1002/qj.49709540402](https://doi.org/10.1002/qj.49709540402).
- Bretherton, F. P. (1969b). "On the mean motion induced by internal gravity waves". In: *Journal of Fluid Mechanics* 95, pp. 785–803. DOI: [10.1017/S0022112069001984](https://doi.org/10.1017/S0022112069001984).

BIBLIOGRAPHY

- Broad, A. S. (1996). "High-resolution numerical-model integrations to validate gravity-wave-drag parametrization schemes: A case-study". In: *Quarterly Journal of the Royal Meteorological Society* 122(535), pp. 1625–1653. ISSN: 1477-870X. DOI: [10.1002/qj.49712253508](https://doi.org/10.1002/qj.49712253508).
- Charney, J. G. and N. A. Phillips (1953). "Numerical integration of the quasi-geostrophic equations for barotropic and simple baroclinic flows". In: *Journal of Atmospheric Science* 10, pp. 71–99. DOI: [10.1175/1520-0469\(1953\)010<0071:NIOTQG>2.0.CO;2](https://doi.org/10.1175/1520-0469(1953)010<0071:NIOTQG>2.0.CO;2).
- Chen, Ch-Ch., D. R. Durran, and G. J. Hakim (2005). "Mountain-Wave Momentum Flux in an Evolving Synoptic-Scale Flow". In: *Journal of Atmospheric Science* 62, pp. 3213–3231. DOI: [10.1175/JAS3543.1](https://doi.org/10.1175/JAS3543.1).
- Chen, Ch-Ch., D. R. Durran, and G. J. Hakim (2006). "Transient Mountain Waves and Their Interaction with Large Scales". In: *Journal of Atmospheric Science* 64, pp. 2378–2400. DOI: [10.1175/JAS3972.1](https://doi.org/10.1175/JAS3972.1).
- Cooley, J. W. and J. W. Tukey (1965). "An algorithm for the machine calculation of complex Fourier series". In: *Mathematics of Computation* 19, pp. 297–301. ISSN: 0025–5718.
- Cotter, C.J. and Thuburn J. (2012). "A finite element exterior calculus framework for the rotating shallow-water equations". In: *J. Comput. Phys.* 231 (21), pp. 7076–7091.
- Cotter, C.J. and Thuburn J. (2014). "Mixed finite elements for numerical weather prediction". In: *J. Comput. Phys.* 257, pp. 1506–1526.
- Dennis, J. et al. (2011). "CAM-SE: A scalable spectral element dynamical core for the Community Atmosphere Model". In: *Int. J. High Perform. Comput. Appl.* DOI: [10.1177/1094342011428142](https://doi.org/10.1177/1094342011428142).
- Dubos, T. and M. Tort (2014). "Equations of atmospheric motion in non-Eulerian vertical coordinates: vector-invariant form and quasi-Hamiltonian formulation". In: *Mon. Wea. Rev.* 142, pp. 3860–3880. DOI: [10.1175/MWR-D-14-00069.1](https://doi.org/10.1175/MWR-D-14-00069.1).
- Durran, D. R. (2010). *Numerical Methods for Fluid Dynamics*. 2nd. Springer-Verlag New York. DOI: [10.1007/978-1-4419-6412-0](https://doi.org/10.1007/978-1-4419-6412-0).

BIBLIOGRAPHY

- Eldred, C. and D. Randall (2017). "Total energy and potential enstrophy conserving schemes for the shallow water equations using Hamiltonian methods – Part 1: Derivation and properties". In: *Geoscientific Model Development* 10(2), pp. 791–810. DOI: [10.5194/gmd-10-791-2017](https://doi.org/10.5194/gmd-10-791-2017).
- Eliassen, A. and E. Palm (1960). "On the transfer of energy in stationary mountain waves". In: *Geophys. Publ.* 22(3), pp. 1–23.
- Gagnon, J.-S., S. Lovejoy, and D. Schertzer (2006). "Multifractal earth topography". In: *Nonlinear Processes in Geophysics* 13(5), pp. 541–570. DOI: [10.5194/npg-13-541-2006](https://doi.org/10.5194/npg-13-541-2006).
- Gal-Chen, T. and R. C. J. Somerville (1975). "On the use of a coordinate transformation for the solution of the Navier-Stokes equations." In: *J. Comput. Phys.* 17, pp. 209–228. DOI: [10.1016/0021-9991\(75\)90037-6](https://doi.org/10.1016/0021-9991(75)90037-6).
- Garratt, J. R. (1977). "Review of Drag Coefficients over Oceans and Continents". In: *Monthly Weather Review* 105(7), pp. 915–929. DOI: [10.1175/1520-0493\(1977\)105<0915:RODCOO>2.0.CO;2](https://doi.org/10.1175/1520-0493(1977)105<0915:RODCOO>2.0.CO;2).
- Giraldo, F. X., J. F. Kelly, and E. M. Constantinescu (2013a). "Implicit-explicit formulations of a three-dimensional nonhydrostatic unified model of the atmosphere (NUMA)". In: *SIAM J. on Sci. Comp.* 35(5), B1162–B1194. DOI: [10.1137/120876034](https://doi.org/10.1137/120876034).
- Giraldo, F. X., J. F. Kelly, and E. M. Constantinescu (2013b). "Implicit-explicit formulations of a three-dimensional nonhydrostatic unified model of the atmosphere (NUMA)". In: *SIAM J. Sci. Comput.* 35(5), B1162–B1194. DOI: [10.1137/120876034](https://doi.org/10.1137/120876034).
- Giraldo, F. X. and M. Restelli (2008). "A study of spectral element and discontinuous Galerkin methods for the Navier Stokes equations in nonhydrostatic mesoscale atmospheric modeling: Equation sets and test cases". In: *J. Comput. Phys.* 227, pp. 3849–3877. DOI: [10.1016/j.jcp.2007.12.009](https://doi.org/10.1016/j.jcp.2007.12.009).
- Giraldo, F. X. and T. E. Rosmond (2004). "A scalable Spectral Element Eulerian Atmospheric Model (SEE-AM) for NWP: Dynamical core tests". In: *Mon. Weather Rev.* 132, pp. 133–153. DOI: [10.1175/1520-0493\(2004\)132<0133:ASSEEA>2.0.CO;2](https://doi.org/10.1175/1520-0493(2004)132<0133:ASSEEA>2.0.CO;2).

BIBLIOGRAPHY

- Guerra, J. E. and P. A. Ullrich (2016). "A high-order staggered nodal-finite element vertical discretization for non-hydrostatic atmospheric models". In: *Geosci. Model Dev.* 9(5), pp. 2007–2029. DOI: [10.5194/gmd-9-2007-2016](https://doi.org/10.5194/gmd-9-2007-2016).
- Haarsma, R. J. et al. (2016). "High Resolution Model Intercomparison Project (HighResMIP v1.0) for CMIP6". In: *Geoscientific Model Development* 9(11), pp. 4185–4208. DOI: [10.5194/gmd-9-4185-2016](https://doi.org/10.5194/gmd-9-4185-2016).
- Herring, J. R. and O. Métais (1989). "Numerical experiments in forced stably stratified turbulence". In: *Journal of Fluid Mechanics* 202, 97–115. DOI: [10.1017/S0022112089001114](https://doi.org/10.1017/S0022112089001114).
- Holton, J. R. (1982). "The Role of Gravity Wave Induced Drag and Diffusion in the Momentum Budget of the Mesosphere". In: *Journal of the Atmospheric Sciences* 39(4), pp. 791–799. DOI: [10.1175/1520-0469\(1982\)039<0791:TROGWI>2.0.CO;2](https://doi.org/10.1175/1520-0469(1982)039<0791:TROGWI>2.0.CO;2).
- Holton, J. R. (1983). "The Influence of Gravity Wave Breaking on the General Circulation of the Middle Atmosphere". In: *Journal of Atmospheric Science* 40, pp. 2497–2507. DOI: [10.1175/1520-0469\(1983\)040<2497:TIOGWB>2.0.CO;2](https://doi.org/10.1175/1520-0469(1983)040<2497:TIOGWB>2.0.CO;2).
- Holton, J. R. and G. J. Hakim (2012). *An Introduction to Dynamic Meteorology*. 5th. Elsevier.
- Holton, J. R. and W. M. Wehrbein (1980). "A Numerical Model of the Zonal Mean Circulation of the Middle Atmosphere". In: *Pure and Applied Geophysics* 118, pp. 284–306. DOI: [10.1007/BF01586455](https://doi.org/10.1007/BF01586455).
- Howard, L. N. (1961). "Note on a paper by John W. Miles". In: *Journal of Fluid Mechanics*. DOI: [10:5096-5126](https://doi.org/10.5096/5126).
- Huynh, H. T. (2007). "A flux reconstruction approach to high-order schemes including discontinuous Galerkin methods". In: *AIAA paper* 4079.
- Jimenez, L. (2017). *Digital Terrain Map DTM, Ecuador*. CD-ROM. Request ID: UITEY-DECGI-2017-0009-0. URL: <http://www.igm.gob.ec/index.php/en/servicios>.
- Kinnmark, I. P. E. and W. G. Gray (1984a). "One step integration methods of third-fourth order accuracy with large hyperbolic stability limits". In: *Math. Comput. Simulat.* 26(3), pp. 181–188. DOI: [10.1016/0378-4754\(84\)90056-9](https://doi.org/10.1016/0378-4754(84)90056-9).

BIBLIOGRAPHY

- Kinnmark, I. P. E. and W. G. Gray (1984b). "One step integration methods with maximum stability regions". In: *Math. Comput. Simulat.* 26(2), pp. 87–92. DOI: [10.1016/0378-4754\(84\)90039-9](https://doi.org/10.1016/0378-4754(84)90039-9).
- Klemp, J. B. and D. R. Lilly (1975). "The Dynamics of Wave-Induced Downslope Winds". In: *Journal of Atmospheric Science* 131, pp. 1229–1239. DOI: [10.1175/1520-0493\(2003\)131<1229:NCOMTI>2.0.CO;2](https://doi.org/10.1175/1520-0493(2003)131<1229:NCOMTI>2.0.CO;2).
- Klemp, J. B., W. C. Skamarock, and O. Fuhrer (2003). "Numerical Consistency of Metric Terms in Terrain-Following Coordinates". In: *Mon. Weather Rev.* 32, pp. 320–339. DOI: [https://doi.org/10.1175/1520-0469\(1975\)032<0320:TOWID>2.0.CO;2](https://doi.org/10.1175/1520-0469(1975)032<0320:TOWID>2.0.CO;2).
- Lauritzen, P. H. et al. (2015). "NCAR Topo (v1.0): NCAR global model topography generation software for unstructured grids". In: *Geoscientific Model Development* 8(12), pp. 3975–3986. DOI: [10.5194/gmd-8-3975-2015](https://doi.org/10.5194/gmd-8-3975-2015).
- Lilly, D. K. (1983). "Stratified Turbulence and the Mesoscale Variability of the Atmosphere". In: *Journal of the Atmospheric Sciences* 40(3), pp. 749–761. DOI: [10.1175/15200469\(1983\)040<0749:STATMV>2.0.CO;2](https://doi.org/10.1175/15200469(1983)040<0749:STATMV>2.0.CO;2).
- Lin, S.-J. (2004). "A "vertically Lagrangian" finite-volume dynamical core for global models". In: *Mon. Weather Rev.* 132(10). DOI: [10.1175/1520-0493\(2004\)132<2293:AVLFDC>2.0.CO;2](https://doi.org/10.1175/1520-0493(2004)132<2293:AVLFDC>2.0.CO;2).
- Lindborg, E. (2006). "The energy cascade in a strongly stratified fluid". In: *Journal of Fluid Mechanics* 550, 207–242. DOI: [10.1017/S0022112005008128](https://doi.org/10.1017/S0022112005008128).
- Lindzen, R. S. (1981). "Turbulence and Stress Owing to Gravity Wave and Tidal Breakdown". In: *J. of Geophysical Research: Oceans* 86, pp. 9707–9714. DOI: [10.1029/JC086iC10p09707](https://doi.org/10.1029/JC086iC10p09707).
- Lott, F. and M. J. Miller (1997). "A new subgrid-scale orographic drag parametrization: Its formulation and testing". In: *Quarterly Journal of the Royal Meteorological Society* 123(537), pp. 101–127. ISSN: 1477-870X. DOI: [10.1002/qj.49712353704](https://doi.org/10.1002/qj.49712353704).
- Majda, A. J. and J. A. Biello (2004). "A multiscale model for tropical intraseasonal oscillations". In: *Proceedings of the National Academy of Sciences* 101(14), pp. 4736–4741. ISSN: 0027-8424. DOI: [10.1073/pnas.0401034101](https://doi.org/10.1073/pnas.0401034101).

BIBLIOGRAPHY

- McFarlane, N. A. (1987). "The Effect of Orographically Excited Gravity Wave Drag on the General Circulation of the Lower Stratosphere and Troposphere". In: *Journal of Atmospheric Science* 44, pp. 1775–1800. DOI: [10.1175/1520-0469\(1987\)044<1775:TE00EG>2.0.CO;2](https://doi.org/10.1175/1520-0469(1987)044<1775:TE00EG>2.0.CO;2).
- Melvin, T., A. Staniforth, and J. Thuburn (2012). "Dispersion analysis of the spectral element method". In: *Quarterly Journal of the Royal Meteorological Society* 138(668), pp. 1934–1947. ISSN: 1477-870X. DOI: [10.1002/qj.1906](https://doi.org/10.1002/qj.1906).
- Métais, O. et al. (1996). "Inverse cascade in stably stratified rotating turbulence". In: *Dynamics of Atmospheres and Oceans* 23(1). Stratified flows, pp. 193 –203. ISSN: 0377-0265. DOI: [https://doi.org/10.1016/0377-0265\(95\)00413-0](https://doi.org/10.1016/0377-0265(95)00413-0).
- Miles, J. W. (1961). "On the stability of heterogeneous shear flows". In: *Journal of Fluid Mechanics*. DOI: [10:496–508](https://doi.org/10.4966/1.508).
- Nappo, C. J. (2012). *An introduction to atmospheric gravity waves*. 2nd. Elsevier.
- Neale, Richard B et al. (2010). "Description of the NCAR community atmosphere model (CAM 5.0)". In: *NCAR Tech. Note NCAR/TN-486+ STR* 1(1), pp. 1–12.
- Palmer, T. N., Shutts G. J., and Swinbank R. (1986). "Alleviation of a systematic westerly bias in general circulation and numerical weather prediction models through an orographic gravity wave drag parametrization". In: *Quarterly Journal of the Royal Meteorological Society* 112, pp. 1001–1039. DOI: [10.1002/qj.49711247406](https://doi.org/10.1002/qj.49711247406).
- Patera, A. T. (1984). "A spectral element method for fluid dynamics: Laminar flow in a channel expansion". In: *J. Comput. Phys.* 54(3), pp. 468–488. ISSN: 0021-9991. DOI: [10.1016/0021-9991\(84\)90128-1](https://doi.org/10.1016/0021-9991(84)90128-1).
- Riley, J. J. and S. M. deBruynKops (2003). "Dynamics of turbulence strongly influenced by buoyancy". In: *Physics of Fluids* 15(7), pp. 2047–2059. DOI: [10.1063/1.1578077](https://doi.org/10.1063/1.1578077).
- Robert, C. (1993). "Bubble convection experiments with a semi-implicit formulation of the Euler equations". In: *Journal of Atmospheric Science* 50, pp. 1865–1873. DOI: [10.1175/1520-0493\(2002\)130<2459:ANTFVC>2.0.CO;2](https://doi.org/10.1175/1520-0493(2002)130<2459:ANTFVC>2.0.CO;2).

BIBLIOGRAPHY

- Schär, C. et al. (2002). "A New Terrain-Following Vertical Coordinate Formulation for Atmospheric Prediction Models". In: *Mon. Weather. Rev.* 130, pp. 2459–2480. DOI: [10.1175/1520-0493\(2002\)130<2459:ANTFVC>2.0.CO;2](https://doi.org/10.1175/1520-0493(2002)130<2459:ANTFVC>2.0.CO;2).
- Scinocca, J. F. and N. A. McFarlane (2000). "The parametrization of drag induced by stratified flow over anisotropic orography". In: *Quarterly Journal of the Royal Meteorological Society* 126(568), pp. 2353–2393. ISSN: 1477-870X. DOI: [10.1002/qj.49712656802](https://doi.org/10.1002/qj.49712656802).
- Shen, J., T. Tang, and L-L. Wang (2011). *Spectral Methods: Algorithms, Analysis, and Applications*. Springer-Verlag Berlin Heidelberg. DOI: [10.1007/978-3-540-71041-7](https://doi.org/10.1007/978-3-540-71041-7).
- Skamarock, W. C. et al. (2012). "A Multiscale Nonhydrostatic Atmospheric Model Using Centroidal Voronoi Tessellations and C-Grid Staggering". In: *Monthly Weather Review* 140(9), pp. 3090–3105. DOI: [10.1175/MWR-D-11-00215.1](https://doi.org/10.1175/MWR-D-11-00215.1).
- Smith, R. B. (1979). "The influence of mountains on the atmosphere". In: *Adv. Geophys.* 21, pp. 87–230.
- Smith, R. B. (1980). "Linear theory of stratified hydrostatic flow past an isolated mountain". In: *Tellus* 32, pp. 348–364.
- Straka, J. M. et al. (1993). "Numerical solutions of a non-linear density current: A benchmark solution and comparisons". In: *Int. J. Numer. Meth. Fl.* 17, pp. 1–22. DOI: [10.1002/flid.1650170103](https://doi.org/10.1002/flid.1650170103).
- Taylor, M. A. and A. Fournier (2010). "A compatible and conservative spectral element method on unstructured grids". In: *J. Comput. Phys.* 229(17), pp. 5879–5895. ISSN: 0021-9991. DOI: [10.1016/j.jcp.2010.04.008](https://doi.org/10.1016/j.jcp.2010.04.008).
- Teixeira, M. A. C. (2014). "The physics of orographic gravity wave drag". In: *Front. Phys.* 2(43). DOI: [10.3389/fphy.2014.00043](https://doi.org/10.3389/fphy.2014.00043).
- Thuburn, J (2006). "Vertical discretizations giving optimal representation of normal modes: Sensitivity to the form of the pressure-gradient term". In: *Quarterly Journal of the Royal Meteorological Society* 132(621), pp. 2809–2825. DOI: [10.1256/qj.06.10](https://doi.org/10.1256/qj.06.10).

BIBLIOGRAPHY

- Thuburn, J., C. J. Cotter, and T. Dubos (2014). "A mimetic, semi-implicit, forward-in-time, finite volume shallow water model: comparison of hexagonal-icosahedral and cubed-sphere grids". In: *Geoscientific Model Development* 7(3), pp. 909–929. DOI: [10.5194/gmd-7-909-2014](https://doi.org/10.5194/gmd-7-909-2014).
- Thuburn, J. and T. J. Woollings (2005). "Vertical discretizations for compressible Euler equation atmospheric models giving optimal representation of normal modes". In: *J. Comput. Phys.* 203(2), pp. 386–404. DOI: [10.1016/j.jcp.2004.08.018](https://doi.org/10.1016/j.jcp.2004.08.018).
- Tort, M. and T. Dubos (2014). "Usual Approximations to the Equations of Atmospheric Motion: A Variational Perspective". In: *Journal of the Atmospheric Sciences* 71(7), pp. 2452–2466. DOI: [10.1175/JAS-D-13-0339.1](https://doi.org/10.1175/JAS-D-13-0339.1).
- Toy, M. D. and D. A. Randall (2007). "Comment on the article "Vertical discretizations for compressible Euler equation atmospheric models giving optimal representation of normal modes" by Thuburn and Woollings". In: *J. Comput. Phys.* 223(1), pp. 82–88. DOI: [10.1016/j.jcp.2006.08.022](https://doi.org/10.1016/j.jcp.2006.08.022).
- Ullrich, P. A. (2012). "Atmospheric Modeling with High-Order Finite-Volume Methods". PhD thesis. University of Michigan.
- Ullrich, P. A. (2014a). "A global finite-element shallow-water model supporting continuous and discontinuous elements". In: *Geosci. Model Dev.* 7(6), pp. 3017–3035. DOI: [10.5194/gmd-7-3017-2014](https://doi.org/10.5194/gmd-7-3017-2014).
- Ullrich, P. A. (2014b). "Understanding the treatment of waves in atmospheric models. Part 1: The shortest resolved waves of the 1D linearized shallow-water equations". In: *Quarterly Journal of the Royal Meteorological Society* 140 (682), pp. 1426–1440. DOI: [10.1002/qj.2226](https://doi.org/10.1002/qj.2226).
- Ullrich, P. A. (2014c). "Understanding the treatment of waves in atmospheric models. Part 1: The shortest resolved waves of the 1D linearized shallow-water equations". In: *Quarterly Journal of the Royal Meteorological Society* 140 (682), pp. 1426–1440. DOI: [10.1002/qj.2226](https://doi.org/10.1002/qj.2226).
- Ullrich, P. A. and J. E. Guerra (2015). "Exploring the Effects of a High-Order Vertical Coordinate in a Non-Hydrostatic Global Model." In: Conf. on Computational Science: Numerical and Computational Developments to Advance Multiscale Earth System Models (MSESM).

BIBLIOGRAPHY

- Ullrich, P. A. and C. Jablonowski (2012). "MCore: A non-hydrostatic atmospheric dynamical core utilizing high-order finite-volume methods". In: *J. Comput. Phys.* 231(15), pp. 5078–5108. DOI: [10.1016/j.jcp.2012.04.024](https://doi.org/10.1016/j.jcp.2012.04.024).
- Ullrich, P. A., K. A. Reed, and C. Jablonowski (2015). "Analytical initial conditions and an analysis of baroclinic instability waves in f - and β -plane 3D channel models". In: *Quarterly Journal of the Royal Meteorological Society*. In press. DOI: [10.1002/qj.2583](https://doi.org/10.1002/qj.2583).
- Weideman, J. A. and S. C. Reddy (2000). "A MATLAB Differentiation Matrix Suite". In: *ACM Trans. Math. Softw.* 26(4), pp. 465–519. ISSN: 0098-3500. DOI: [10.1145/365723.365727](https://doi.org/10.1145/365723.365727).
- Wood, Nigel and Pual Mason (1993). "The Pressure force induced by neutral, turbulent flow over hills". In: *Quarterly Journal of the Royal Meteorological Society* 119(514), pp. 1233–1267. ISSN: 1477-870X. DOI: [10.1002/qj.49711951402](https://doi.org/10.1002/qj.49711951402).
- Zhu, X. and J. R. Holton (1987). "Mean Fields Induced by Local Gravity-Wave Forcing in the Middle Atmosphere". In: *Journal of Atmospheric Science* 44, pp. 620–630. DOI: [10.1175/1520-0469\(1987\)044<0620:MFIBLG>2.0.CO;2](https://doi.org/10.1175/1520-0469(1987)044<0620:MFIBLG>2.0.CO;2).
- Zienkiewicz, O. C., R. L. Taylor, and J. Z. Zhu (2005). *The finite element method: its basis and fundamentals*. 6th. Butterworth-Heinemann.